Master in Physics
Department of Physics and Technology
University of Bergen

Effect of Free Water Elimination on Diffusion Indices in Healthy Volunteers and Patients with Multiple Sclerosis

Emile Schjeldsøe Berg

Supervisor: Assoc. Prof. Eli Renate Grüner

Bergen, October 2018

Abstract

Diffusion tensor imaging (DTI) is a technique in magnetic resonance imaging (MRI) that can be used to image the brain microstructure beyond the resolution that is achievable using conventional imaging. By utilizing DTI, it is possible to study the neuronal fiber bundles non-invasively, fascilitating virtual dissection of internal brain structures. One problem this technique faces, however, is the effect of free water contamination, i.e voxels inherently or due to disease processes have higher water content (isotropic diffusion) or consist of crossing fiber bundles (mixed mode contribution).

In order to get a more accurate estimation of the diffusion indices, a new model was introduced by Prof. O. Pasternak. The free water elimination (FWE) model removes the free water contamination in DTI. By estimating a free water portion of the diffusion tensor, a free water corrected tensor can be estimated that has a more accurate anisotropy.

This master project is an application of the FWE model on a group of healthy volunteers and on a group of participants recently diagnosed with Multiple Sclerosis (MS). FWE is applied in each participant group. Diffusion indices are then estimated and compared, both before and after FWE and between the two groups. Four regions of the brain are evaluated and compared: white matter, grey matter, the whole brain, and a small region of interest (ROI) in the corpus callosum.

Using a baseline b_0 image, grey and white matter masks are able to be segmented based on a probability threshold ($> 80\%$). This allows for the estimation of the relevant indices isolated to these regions. By combining this with images of the change in the indices caused by FWE, it is possible to get an understanding of where it has the highest impact.

FWE was applied to the healthy volunteers in order to get an understanding of the effects of free water correction. Furthermore, it was of interest to repeat the analysis for a patient group to see how these effects might change. In this thesis, FWE is applied to a group of participants with MS for the first time, this is done for a technical evaluation and not for clinical purposes.

The effect of FWE within each group is significant for almost all regions and indices, approximately 20%. The change in eigenvalues and anisotropy indices is similar to the findings of established literature. It is the first time this technique has been applied to MS, and the results are promising for future follow-up studies using FWE. In the white matter and whole brain analysis there are non-significant differences between the two groups. However, the anisotropy measures in the grey matter are significantly higher in the healthy volunteers compared to the participants with MS.

FWE has a significant impact on diffusion indices, in all regions investigated in this thesis. Because FWE is a new and still developing technique, the work in this thesis has been important to achieve a better understanding of how FWE works, and shows a lot of promise for future study and development.

Acknowledgements

I would like to thank everyone who have supported and helped me in my work on this thesis, especially in the last few months. I could never have done this by myself. I would especially like to thank some people in particular:

First of all, my supervisor, Assoc. Prof. Eli Renate Grüner for always being helpful, positive, and most importantly available. Answering all questions with great detail and clarity, and being very supportive throughout the whole process. For introducing me to the field of medical physics, and making me realize it is one of the most exciting fields in physics.

I would also like to thank Postdoc. Ørjan Bergmann for helping me to get started with the programming, and for providing invaluable insight with any issues pertaining to programming. Additionally, thank you for suggesting this project in the first place.

I want to express my gratitude to the principle investigators of the clinical studies, Prof. Kjell-Morten Myhr (patient studies) and R.G(healthy volunteer studies), that have provided me with the image data used in the evaluations.

A thank you to everyone who allow us to use their data for research purposes, you are the ones who make all this possible. Lastly, friends and family for all the support, food, and encouragement along the way.

Contents

Abbreviations

ADC	Apparent diffusion coefficient
BW	Bandwidth
cl	Linear anisotropy
cp	Planar anisotropy
cs	Spherical anisotropy
CSF	Cerebrospinal fluid
DTI	Diffusion tensor imaging
DWI	Diffusion water imaging
EPI	Echo planar imaging
FA	Fractional anisotropy
FID	Free induction decay
FLAIR-DWI	Fluid-attenuated inversion recovery diffusion weighted imaging
FOV	Field of view
FWE	Free water elimination
GRE	Gradient recalled echo
MD	Mean diffusivity
MRI	Magnetic resonance imaging
MS	Multiple sclerosis
NaN	Not a number

PD Proton density

RA Relative anisotropy

RF Radio frequency

RMS Root mean square

ROI Region of interest

SE Spin echo

SNR Signal-to-noise ratio

TA Acquisition time

TE Echo time

TR Repetition time

VR Volume ratio

List of Figures

List of Tables

Chapter 1

Introduction

DTI is one of the most powerful technique in magnetic resonance imaging (MRI). It enables the measuring of anisotropic diffusion in tissues of unknown orientation. It can measure the characteristics of the fibers, orientation and diffusion, it constructs an ellipsoid consisting of three orthogonal axes with the magnitude along each axis described by its respective eigenvalues, λ_{123}. This allows the microstructures of the brain to be studied, details that are too small to be seen with conventional MRI are revealed. Reconstructing the neural pathways allows for a virtual biopsy, where damage in the fibers can be seen without needing an invasive procedure. DTI is still in its infancy, this means that there are several pitfalls to this technique, one of them is that λ_{123} can be distorted by free water contamination, areas where there is isotropic free water diffusion, caused by blood vessels, cerebrospinal fluid (CSF) or edemas. [1] To estimate and remove the free water portion that cause these problems, a new model was introduced by Pasternak, et al [2], FWE.

The free water elimination seeks to eliminate the part of the diffusion tensor that can be ascribed to this free water contamination, leading to a presumably more accurate estimation of the anisotropic properties of the brain tissue. One example of such a case is an edema, an excess accumulation of fluid in the intracellular or extracellular spaces of the brain, in this case, the edema can disguise the underlying fiber structure. By extension, diagnostically important information could be in these underlying fiber structures, and therefore, hidden by the free water contamination. The opposite case can be that the anistropic indices are erroneously underestimated because a part of the diffusion inside a voxel can be ascribed to the CSF.

The thesis explores this topic in both healthy volunteers and in a small group of patients recently diagnosed with MS. The results from the conventional DTI and FWE are compiled, compared and presented in chapter 4. The methodology on how the data were gathered and processed is described in chapter 3. Chapter 2 tackles the theoretical background for MRI

in general, diffusion weighted imaging (DWI), DTI, and the free water elimination. The significance and meaning of the results are discussed in chapter 5.

1.1 Motivation

The goal of this thesis is to explore the effects of FWE on DWI data. Removing a free water sphere from the diffusion tensor, should increase the anisotropy in all areas of the brain. In other words, the estimated anisotropy indices should change significantly in the direction of higher anisotropy and a higher degree of directionality. FWE should, in theory, reveal more accurate estimations of the indices, without the disruptive influence of free water contamination. In order to do evaluate the correctness of these assumptions, the following steps were taken:

- Understanding the free water elimination as described by Pasternak et al, and implementing it in an image analysis pipeline.
- Gather enough images to make this analysis statistically valid. This step involves collecting diffusion data on 20 healthy volunteers and 20 participants recently diagnosed with MS, following all the ethical standards when acquiring these images.
- Acquiring the required parameters for analysis, this includes masks, gradient values and b-values.
- Implementing code and perform the correction, estimating indices and creating graphical representations.
- Use a statistical analysis to determine the significance of the effect of FWE.
- Reconstruct the fibers to see if the change in the invariant indices have any effect on fiber reconstruction.
- Compare the data from the two groups.

Chapter 2

Theory

2.1 Magnetic Resonance Imaging

2.1.1 Basic Physics

Spin and Magnetization

Magnetic Resonance Imaging uses magnetic fields and electromagnetic waves to create detailed images of the internal structure of tissues without using ionizing radiation. The technique exploits the intrinsic angular momentum of all particles, called spin. Spin is quantized, meaning that it has certain discrete values, if spin is s then each particle can have 2s+1 orientations, for nucleons s=1/2, meaning it can have $2 * \frac{1}{2} + 1 = 2$ orientations, up or down.[3] In nuclei all the spins of the individual nucleons are added together, this means that only nuclei with an uneven amount of nucleons can have a net spin. The unit that interacts with the magnetic field is called the magnetic moment, this value is related to the spin quantum number via equation 2.1 where γ is the gyromagnetic ratio.

$$\mid \mu \mid = \gamma \sqrt{s(s+1)} \tag{2.1}$$

This magnetic moment is manipulated in the imaging process, when exposed to an external static magnetic field there is a splitting of the energy levels, the Zeeman Effect. This splitting is achieved by the magnetic moments aligning parallel or anti-parallel with regards to the magnetic field B_0. [4] The energies of the two alignments are given by equations 2.2 and 2.3.

$$E_{\uparrow} = -\frac{1}{2}\gamma\hbar B_0 \tag{2.2}$$

$$E_{\downarrow} = \frac{1}{2}\gamma\hbar B_0 \tag{2.3}$$

Where $\hbar$ is the reduced Planck constant, and B_0 is the magnetic field of the MRI machine, typically 1.5-3T for clinical use. Equation 2.2 is the energy level of the parallel alignment and 2.3 is the anti-parallel alignment. When imaging a volume the machine only detects the net magnetization of each volume element (voxel), this is given by summing up all the magnetic momenta within the voxel, equation 2.4.

$$\mathbf{M} = \sum_{i=1}^{N_s} \mu_i \tag{2.4}$$

Because nature prefers to be in the lowest energy state, there is always more magnetic momenta in the parallel alignment. The ratio of parallel to anti-parallel alignment is given by equation 2.5.

$$\frac{N_{\uparrow}}{N_{\downarrow}} = e^{\frac{\Delta E}{KT_s}} \tag{2.5}$$

Here, T_s is the temperature in Kelvin, K is the Boltzmann Constant, and ΔE is the energy difference between the two levels, given by equation 2.6.

$$\Delta E = E_{\downarrow} - E_{\uparrow} = \gamma\hbar B_0 \tag{2.6}$$

The net magnetization can then be expressed in terms of $N_{\uparrow}$, $N_{\downarrow}$.

$$\mathbf{M} = \frac{1}{2}(N_{\uparrow} - N_{\downarrow})\gamma\hbar\vec{k} \tag{2.7}$$

Where $\vec{k}$ is the unity vector in the direction of the magnetic field. Now, the number difference of spins in parallel / anti-parallel direction is expressed by 2.8.

$$N_{\uparrow} - N_{\downarrow} = N_s\frac{\gamma\hbar B_0}{2KT_s} \tag{2.8}$$

Here, the new variable N_s is introduced, which is the total number of spins in the given volume. Then the equations 2.7 and 2.8 are combined in order to get an expression for the magnitude of the net magnetization.

$$\mid \mathbf{M} \mid = \frac{\gamma^2\hbar^2 B_0 N_s}{4KT_s} \tag{2.9}$$

This equation shows that the net magnetization magnitude is quadratically dependent on γ, and linearly dependent on N_s. The reason MRI uses the ^{1}H Hydrogen atom when

imaging, is because it is the most abundant, 70 % of the body is H_2O, and it has the largest gyromagnetic ratio of any element. So by choosing Hydrogen, both γ and N_s are maximized. The data in the current thesis was acquired at a clinical whole body 3 Tesla MRI scanner.

Shimming

MRI is highly dependent on having a homogeneous magnetic field in order to correctly encode the spatial information. This homogeneity is commonly required to be on the order of 1 ppm in a volume of several liters. Since it is virtually impossible for the large magnet to hold this kind of homogeneity by itself, shimming is introduced. Shimming is a technique where the local magnetic field is adjusted slightly in order to achieve greater homogeneity. There are two main types of shimming, active and passive, the difference being in the way the magnetic field is adjusted.

Passive shimming relies on magnetic materials that are placed inside the machine in such a way as to cancel out the unwanted harmonics inside the bore. Determining the location, amount and shape of the material to be used for passive shimming is complex, it involves solving equation 2.10 for different configurations of shimming material. [5]

$$d\mathbf{\Phi} = -(d\mathbf{m}/4\pi) \cdot grad_Q(\frac{1}{\nu}) \tag{2.10}$$

This is the scalar magnetic potential at P caused by a magnetic dipole, $d/\mathbf{m}$ given by equation 2.11 located at a point Q, and ν^{-1} is a Green's function. In equation 2.11, the assumption is that the main magnetic field is in the z-direction, χ and dV are properties of the material, namely its magnetic susceptibility and its volume.

$$d\mathbf{m} = \chi H_z dV \mathbf{k} \tag{2.11}$$

Active shimming, like the name suggests uses shim coils with current running through them to negate the inhomogeneity. This is mainly done through two different kinds of coils, superconducting and resistive coils. Superconducting coils are common in systems of 3T or higher, these coils are in the cryostat beyond the main magnetic coils, and once the correction is set, takes a long time to change. Resistive coils are located close to the inner edge of the scanner, close to room temperature, these coils have a current that can be changed quickly, allowing the shimming to be adjusted on a per-patient basis. [6]

Signal Generation

In order to get a readable signal, the net magnetization along B_0 has to be disturbed, in order to do this, energy is added in the form of electromagnetic (EM) waves. When the magnetic

moments align with B_o they precess around the magnetic field line with a frequency called the Larmor frequency, given by the Larmor equation.

$$\omega = \gamma B_0 \tag{2.12}$$

The equation gives the resonance frequency needed in order to perturb the net magnetization, this frequency is in the RF area of the EM spectrum. Without this perturbation the magnetic moments nullify each other, leading to zero net magnetization in the x-y plane before perturbation. The data in the current thesis were acquired at a clinical whole body 3 Tesla MRI scanner, resulting in $\omega = 127.74Mhz$.

After exciting the magnetic moments using the RF frequency given by equation 2.12, there is a precessing magnetization in the x-y plane. This precession creates the Free Induction Decay (FID) signal, with a frequency equal to the Larmor frequency. The component of the total magnetization perpendicular to the magnetic field B_0 is given by:

$$M_xy = M_0 e^{t/T_2} \tag{2.13}$$

The component of the excited magnetization parallel to the magnetic field is given by:

$$M_z = M_0(1 - e^{t/T_1}) \tag{2.14}$$

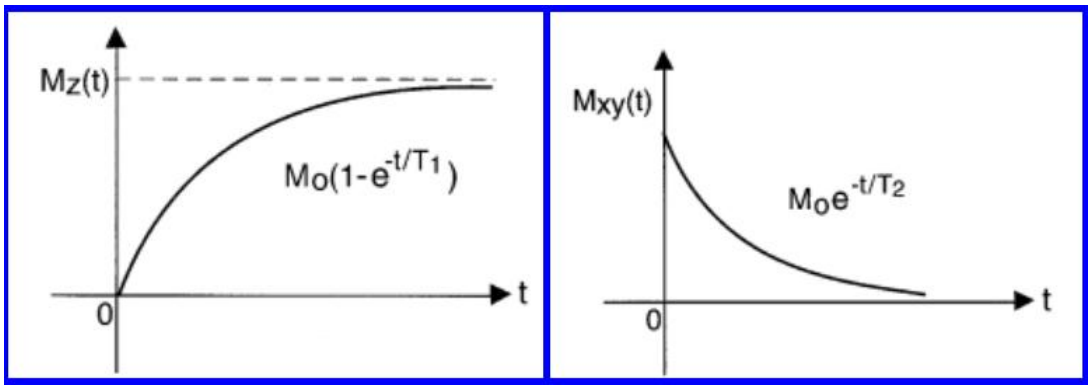

Figure 2.1: Graph representation of T_1 and T_2 relaxation times. [7]

T_1 and T_2 denotes the two relaxation times for the magnetization components in the z- and x-y-directions respectively, shown in figure 2.1. These relaxation times describe how long it takes for the magnetization to return to its original state, that means a recovery of 63% of M_z and a loss of phase coherence to 37% of M_xy for T_1 and T_2 respectively. These two relaxation times are independent of each other and dependent on tissue type, for example,

free water has a long T_1 and T_2, while fat has a short T_1 and T_2, this is used to differentiate tissues in an MRI image, in order to identify pathology or monitor therapy.

In a standard 1.5T clinical MRI, the relaxation times are on the order of several hundred milliseconds for T_1 and tens to a hundred milliseconds for T_2. When moving to higher field strengths, T_1 increases, while T_2 remains more or less constant, at very high field strengths ($B_0 > 7T$) T_2 begins to decrease. [8]

As mentioned earlier, the precession creates a FID signal, this signal is generated too quickly to be of any use, due to the machine not being able to spatially encode the signal. Therefore, the echo of the FID signal is used in order to encode the signal and that way create an image with spatial encoding. There are two main ways to create this echo, one is using several RF pulses, called spin echo (SE) sequences, and the other is using magnetic gradient reversal, called gradient recalled echo sequences (GRE). These techniques are discussed more in detail later in section 2.1.3.

Flip Angle

The angle between the precession and the magnetic field is called the flip angle, the flip angle is expressed as equation 2.15.

$$\alpha = \omega_1 t_p = -\gamma B_1 t_p \tag{2.15}$$

Where ω_1 is the angular velocity of the precession, and t_p is the amount of time the RF-field B_1 is active. This equation follows from the Larmor frequency through some steps, starting at the Larmor frequency 2.12. Faraday's law of induction gives an electromotive force (ϵ) induced on the receiver coils, expressed by the number of turns in the coils (N) and the magnetic flux (Φ_B).

$$\epsilon = -N\frac{d\Phi_B}{dt} \tag{2.16}$$

The magnetic flux is defined by the surface integral:

$$\iint\limits_{\sum(t)} \mathbf{B}(\mathbf{r}, t) \cdot d\mathbf{A} \tag{2.17}$$

Where $\mathbf{B} \cdot d\mathbf{A}$ is the vector dot product of the magnetic field through the infinitesimal area element $d\mathbf{A}$. As shown in 2.15 the angle is dependent on the strength and duration of B_1. Since the vector B_1 is linearly oscillating it can be written as the sum of two vectors rotating in the opposite directions, B_1^+ and B_1^- with angular frequencies of $-\Omega$ and $+\Omega$ respectively.

$$B_1 = B_1 + + B_1 - = B_1 \begin{bmatrix} cos(-\Omega t) \\ sin(-\Omega t) \\ 0 \end{bmatrix} + B_1 \begin{bmatrix} cos(\Omega t) \\ sin(\Omega t) \\ 0 \end{bmatrix} = 2B_1 \begin{bmatrix} cos(\Omega t) \\ 0 \\ 0 \end{bmatrix} \tag{2.18}$$

Equation 2.19 arises from a change in coordinate system from (x,y,z) to (x',y',z'), where (x',y',z') is a frame of reference that is rotating around the z-axis of the lab frame. The modified Bloch equation 2.20 gives the relation between the effective field B_{eff} and the magnetization.

$$B_{eff} = B_0 + B_1 - \frac{\Omega}{\gamma} \tag{2.19}$$

$$\frac{\partial M}{\partial t} = \gamma M \times B_{eff} \tag{2.20}$$

Applying a RF-field B_1 to this system for a time t_p will result in a precession of M around B_1^+ with the angular velocity given by

$$\omega_1 = \gamma B_1 \tag{2.21}$$

When equation (2.21) is multiplied by the precession time t_p, it becomes the equation for the flip angle (2.15). [9]

2.1.2 Image Acquisition

Contrast

In MRI, there are two intrinsic tissue contrasts, T_1 and T_2. By adjusting the repetition time (TR) and echo time (TE) parameters, the images become either T_1 weighted or T_2 weighted, displaying different characteristics of the scanned volume. By setting both TE and TR to be short, the image becomes T_1 weighted, resulting in fat giving a much stronger signal compared to water due to the rapid realignment properties of fat tissue. Long TR and TE results in a T_2 weighted image, which would give enough time for tissues with both short and long relaxation times to send out a strong signal, resulting in high intensity from both fat and water. [10] T_1 weighted images are mainly used for anatomical and fat imaging. The signal intensity for T_1 in a simple SE sequence is given by equation 2.22. The SE sequence is described later in section 2.1.3.

For pathological imaging T_2 imaging is commonly used due to its sensitivity to both fat and water. Signal intensity in a SE sequence is then given by equation 2.23. In both equation

ρ_0 represents the proton density. In order to make an image ρ_0 weighted, both equations are minimized by using a long TR and short TE.

$$S \propto \rho_0(1 - e^{\frac{-TR}{T_1}}) \tag{2.22}$$

$$S \propto \rho_O e^{\frac{-TE}{T_2}} \tag{2.23}$$

Spatial Resolution

In all imaging, the spatial resolution is very important to distinguish small differences. It generally denotes the amount of pixels in an image, and in MRI it is directly correlated to the physical volume of each voxel in the image. Generally the resolution for MRI is on the scale of mm. [11] For MRI it is important to chose the resolution so that each voxel will have a satisfactory signal-to-noise ratio (SNR), but at the same time not so big so as to lose important details of the scanned volume. Mathematically for MRI the resolution is expressed as a function of the encoding steps and the Field of View (FOV).

$$FOV_x = \Delta x N_x \tag{2.24}$$

$$FOV_y = \Delta y N_y \tag{2.25}$$

In these equations $\Delta_x \Delta_y$ denote the resolution, typically in mm, while $N_x x N_y$ is the matrix formed by the number of frequency and phase encoding steps. The most common matrix sizes used in MRI are 256x256 pixels and 128x128 pixels, increasing the resolution decreases the signal intensity from each voxel.

Choosing correct FOV is important, a common artifact relating to a too narrow FOV is back-folding, this is caused by aliasing resulting in the parts of the object outside of the FOV coming back into the image. This is avoided by choosing a wide enough FOV that it covers the object, but not so wide as to cover a lot of empty space.

Signal-to-Noise Ratio

The SNR is simply the ratio of signal to noise, a measure of how noisy the image is. It is defined as the ratio between the average signal intensity in a region of interest (RoI) in the object being imaged and the standard deviation in an RoI outside of the imaged object. [11] For a single 2D slice the SNR is given by equation 2.26.

$$SNR = A \cdot V_h \sqrt{\frac{N_y Q B_0^3}{BW}} \tag{2.26}$$

$$Q = \omega \frac{L}{R} \tag{2.27}$$

In this equation A is a constant that represents the product of all physical constants relevant to the image, such as susceptibility, temperature, geometry, and size of the object in question. Q is the quality factor of the coil given by equation 2.27, where L is the coil inductance and R is the resistance. BW denotes the bandwidth which is given by $BW = \frac{1}{T_r}$, where T_r is the time used to record the echo signal. SNR is linearly dependent on V_h, the voxel size, this is due to the simple fact that increasing the size of the voxel increases the amount of spins inside the imaged volume, this however will lead to a corresponding decrease in resolution.

To go from 2-D SNR to 3-D SNR, other parameters are added, such as the number of slices, and the effect of multiple averages, this lead to the equation for the grand total SNR 2.28. [9]

$$SNR = A \cdot \sqrt{\frac{Q B_0^3 N_{SA} \cdot N_y N_x}{BW}} V_h \cdot S(TR, TE, \alpha, T1, T2, T2^*, \rho) \tag{2.28}$$

$S(TR, TE, \alpha, T1, T2, T2*, \rho)$ is the sequence dependent signal response and needs to be determined for each pulse sequence. N_{SA} is the number of averages, N_s the number of 3D slices, and N_y is the number of phase encoding steps utilized in the scan.

As can be seen in equation 2.28, there are several ways to improve the SNR, by increasing any one of several parameters. However, increasing the parameters usually leads to either longer scan times, stricter requirements for the hardware, or a reduction in another part of the imaging process, such as resolution. Increasing the magnetic field does the same, but demands more from the gradients and shimming among others. The number of averages can also be used to increase SNR, since $SNR \alpha \sqrt{N_a}$, the same dependence can be found in readout time, phase encoding steps and number of slices. Figure 2.2 shows the effect of increasing the number of averages taken on the SNR, showing that an increase in N_a has the effect of increasing SNR. The effect of readout time is shown in 2.3, as the bandwidth is inversely proportional to the readout time, a low bandwidth value corresponds to a high readout time.

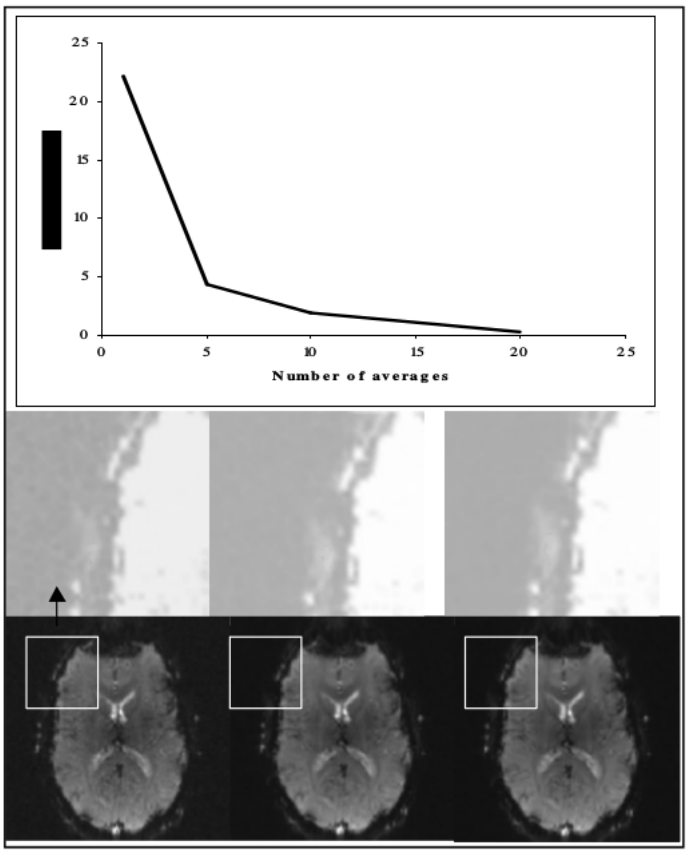

Figure 2.2: The effect of N_a, number of averages, on the SNR, from left to right N_a is 1, 5, and 10. As expected the SNR is increased. [9]

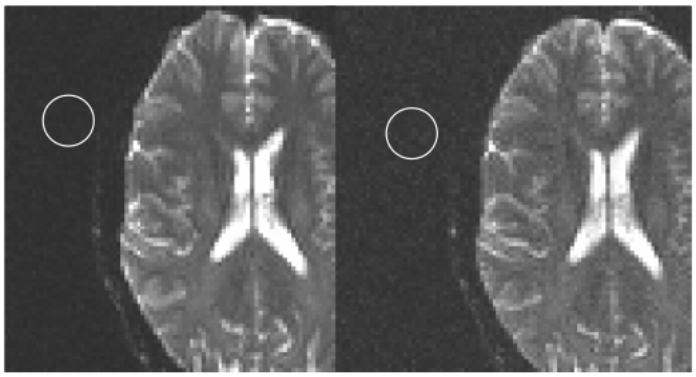

Figure 2.3: Effect of BW on SNR in single-shot SE-EPI. The values of BW are 750Hz and 2055 Hz to the left and right respectively. When all other parameters are equal, the SNR scales inversely with BW. [9]

Gradients

In the MRI machine there are gradient coils in different configurations in order to locally manipulate the magnetic field in all three spatial directions. By creating a spatially dependent magnetic field, in this way, spatial encoding is achieved, since equation 2.12 shows that the frequency and therefore the signal is dependent on the magnetic field strength. The effects of using only one gradient is shown in figure 2.4.

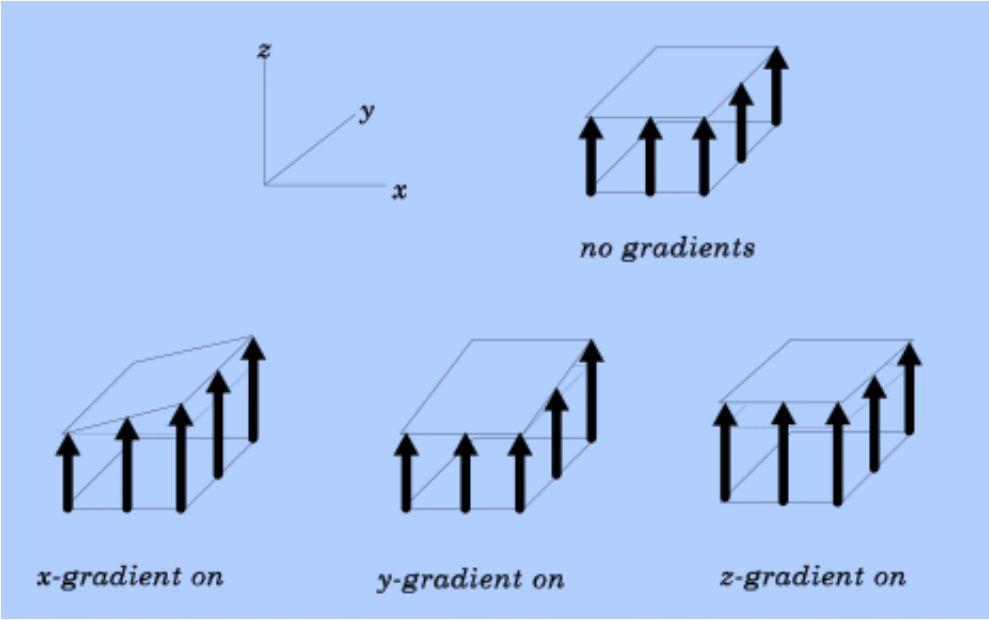

Figure 2.4: The effect of each gradient isolated. [12]

By combining the effect of all three directions, encoding in any direction is possible.

Slice Selection

A 3D image is comprised of several 2D images or "slices" of the volume. These slices are acquired by creating a linearly dependent magnetic field in one direction. This will cause all spins transverse to that axis to have the same resonance frequency as given by equation 2.12. The thickness of each slice is expressed as equation 2.29.

$$\Delta_i = \frac{\Delta\omega}{\gamma G_i} \tag{2.29}$$

In this equation i represents the direction along which slices are to be acquired. G_i then becomes the gradient amplitude along that axis, and $\Delta\omega$ is the bandwidth of the RF-pulse used to excite the sample.

Now that the slice is selected, there still remains the problem of separating each signal within the selected slice. One way of separating the signal within the sample is to apply a constant gradient during the readout of the signal, the resonant frequency will then change along one axis again, and the resultant signal will differ based on the location of the pixel along that axis. This will differentiate the signal within a slice in one dimension, in order to get two dimensional encoding, phase encoding is used.

Phase-encoding is achieved by making two measurements. First a baseline measurement, then applying a gradient before the readout of the signal. In this example, frequency encoding is done in the horizontal direction of the slice. The phase encoding is then done in the vertical direction. In the simplified case of two pixels, A and B along the same vertical axis, where the phase of B is opposite that of A, the total signal can be written as 2.30 for the baseline and as 2.31 for the phase encoded signal.

$$S_0(t) = Asin\omega t + Bsin\omega t = (A+B)sin\omega t \tag{2.30}$$

$$S_1(t) = Asin\omega t - Bsin\omega t = (A-B)sin\omega t \tag{2.31}$$

By combining these two equation, the signal from A and B can be differentiated as shown in equation 2.32 and 2.33.

$$\frac{1}{2}[S_0 + S_1] = \frac{1}{2}[(A+B) + (A-B] = A \tag{2.32}$$

$$\frac{1}{2}[S_0 - S_1] = \frac{1}{2}[(A+B) - (A-B)] = B \tag{2.33}$$

In this way the signal from within the slice in encoded along both axes and individual pixels can be differentiated. [9]

k-space

The MRI echo signals are temporarily stored in a data matrix called k-space. The k-space is a 2-D matrix typically constructed with the phase on the y-axis and the frequency on the x-axis. The imaging sequences fill out k-space in different ways, depending on how the encoding gradients are applied. The temporary matrix is put through a Fourier transformation to make the finished image. The middle of k-space contains the most data on SNR and contrast, while the outer parts contains data on resolution[9]. This way of storing data is shown in figure 2.5.

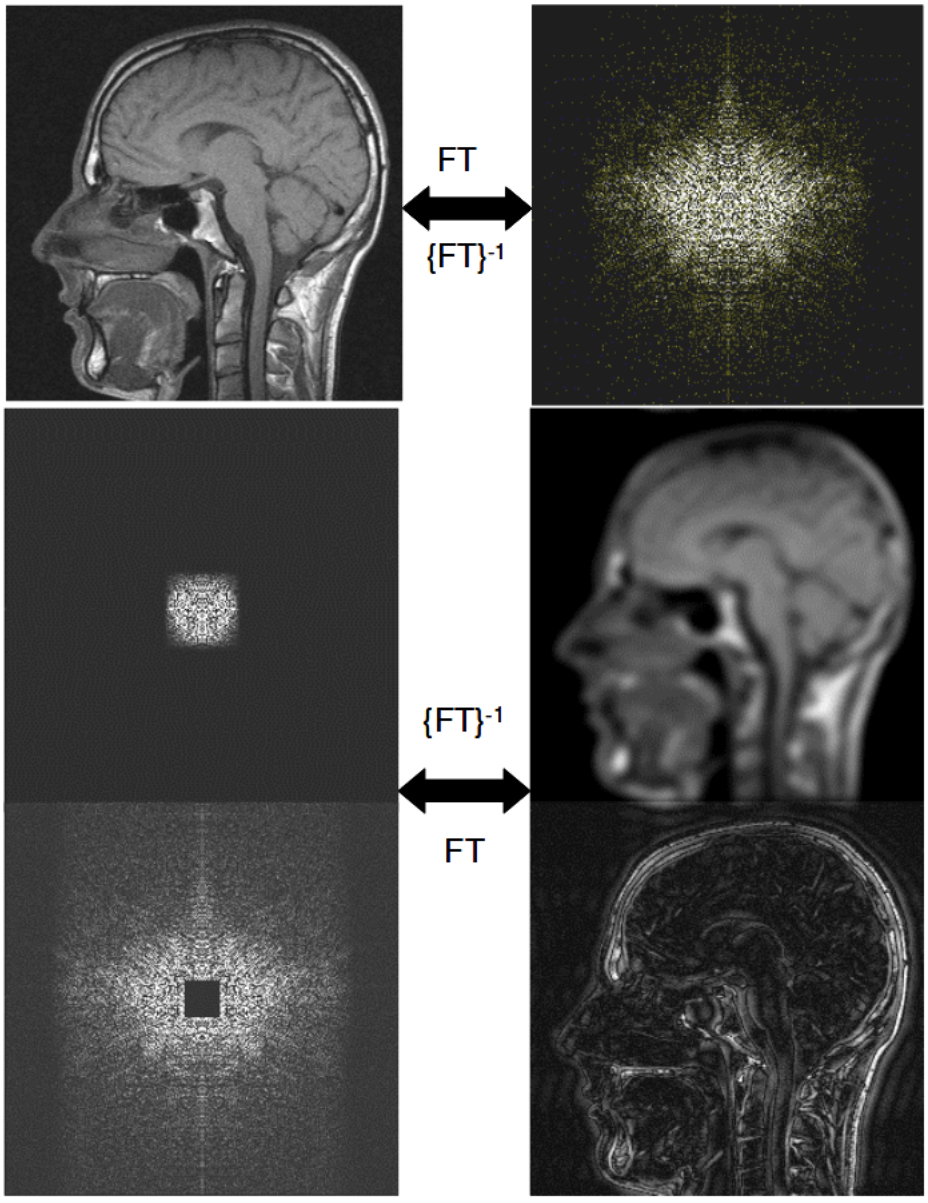

Figure 2.5: The k-space Fourier transform dependence on what part of k-space is being transformed. From right to left, the whole k-space, the middle, and the outer parts.[9]

Proper sampling of k-space is important to ensure the best quality images. Nyquist sampling theorem says that the sampling frequency has to be equal or greater than twice the highest frequency being sampled to ensure a proper signal reconstruction. This puts an effective limit on the resolution and size of the object being scanned. An incomplete reconstruction of the signal is called aliasing, this shows up when the sampling theorem is not followed and the signal is not uniquely identified.

The artifact most associated with k-space is Gibbs ringing. These typically manifest as

multiple parallel lines adjacent to high-contrast interfaces.[14] This is due to a high difference between values over a short space, leading to the Fourier transformation to oscillate after the jump in value. This effect is illustrated in figure 2.6

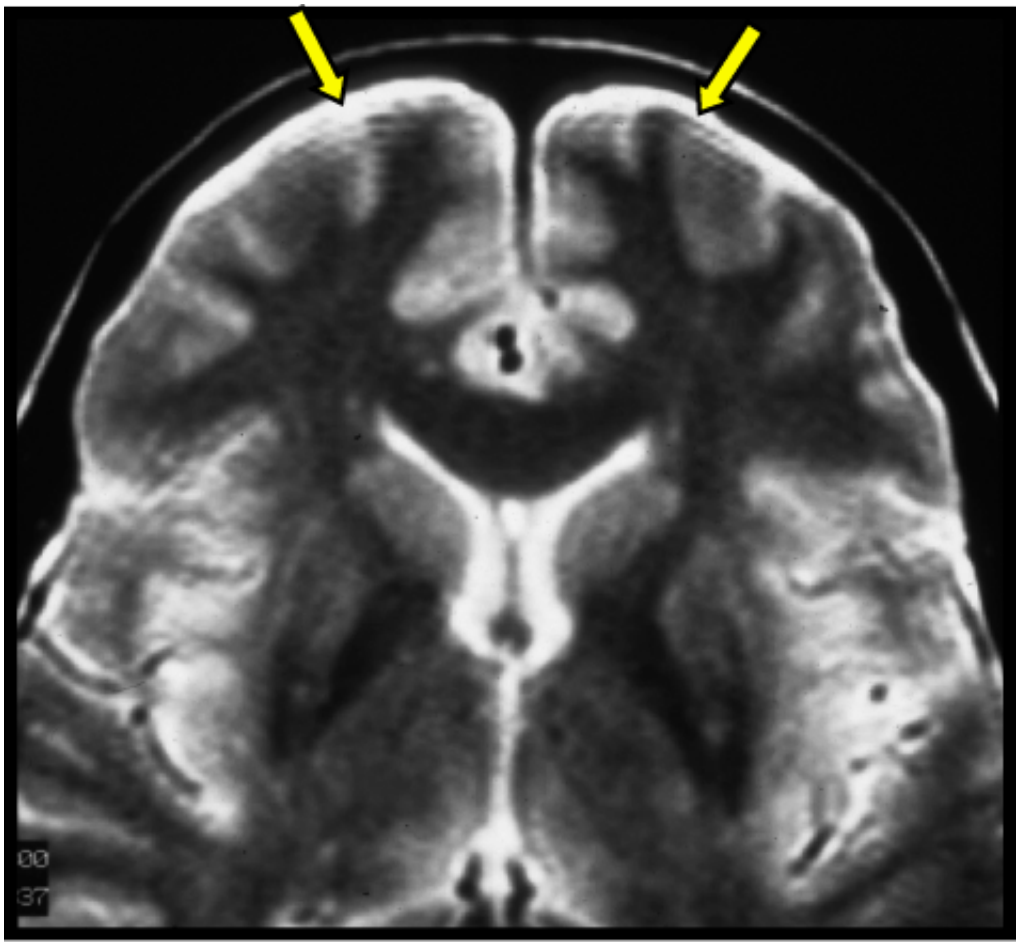

Figure 2.6: Gibbs ringing in the brain, the arrows point to parallel lines caused by the Fourier transformation struggling in high contrast regions. [15]

2.1.3 Sequences

The imaging sequences in MRI differ by the way they fill up k-space. There are two fundamental sequences called SE and GRE, where one creates the echo using radio frequency(RF) pulses, the other uses the gradients. These sequences can be sped up to decrease the scan time.

Spin Echo

SE is one of the basic sequences. It involves using two RF-pulses to create the signal to fill k-space. Figure 2.7 Shows how this signal is generated. First a 90° RF-pulse is applied, flipping the magnetization into the xy-plane. To dephase the spins, a frequency encoding gradient is then applied before the second RF-pulse is applied, the gradient is turned off before the second pulse. This second pulse is a 180° pulse, the purpose of this pulse is to flip all the spins in the xy-plane. Lastly a new frequency encoding gradient is applied and an echo is generated at t=TE.

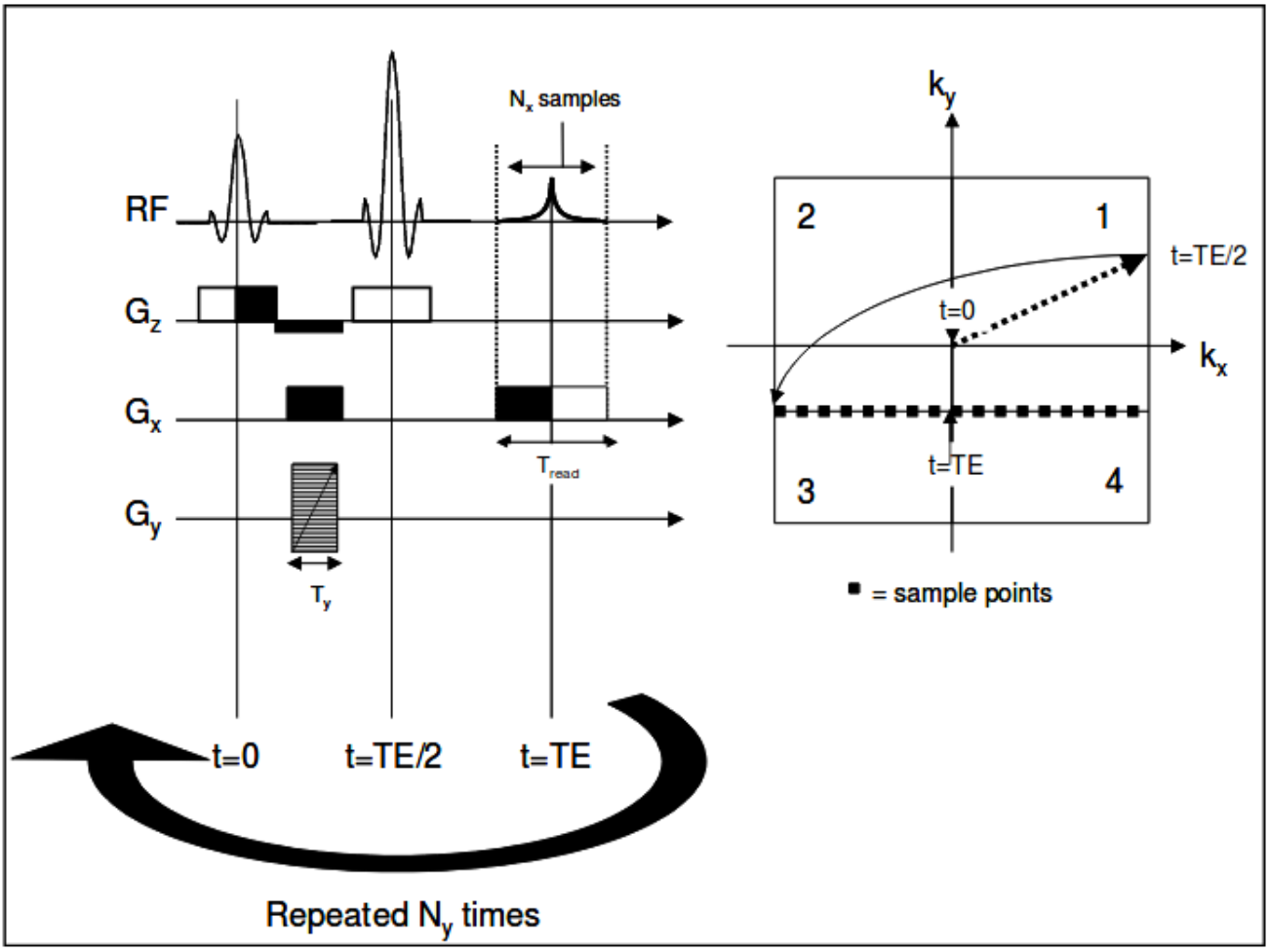

Figure 2.7: The SE sequence, where two frequency encoding gradients are used in conjunction with a 90° and a 180° RF pulse in order to generate a signal at t=TE.[9]

Gradient-Recalled Echo

In contrast to the SE sequence, the GRE sequence uses the gradients to generate the signal, rather than the RF-pulses. The GRE sequence also samples one line of k-space per pulse, just like the SE sequence. The flip angle of the RF pulse can be between 0° and 90°, in order to find the angle with the maximum signal strength, equation (2.34), is used.

$$\alpha_{Ernst} = cos^{-1}(e^{\frac{-TR}{T_1}}) \tag{2.34}$$

In the case of $\alpha > \alpha_{Ernst}$ T_1 weighing is achieved, in the opposite case, where $\alpha < \alpha_{Ernst}$ the images are proton density (PD) weighted. Figure 2.8 shows the GRE sequence.

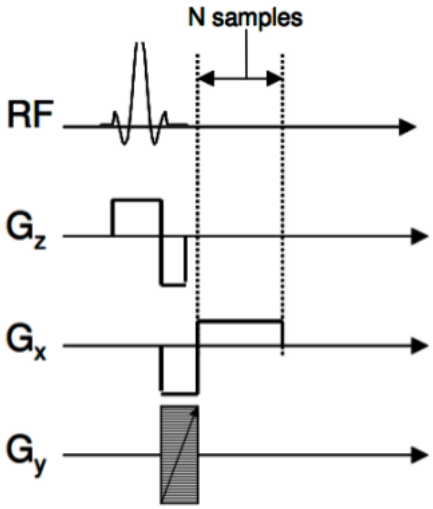

Figure 2.8: The GRE sequence, gradients are used to generate the signal and read one line of k-space after an RF-pulse. [9]

As shown in figure 2.8, k-space is filled by applying a constant negative frequency encoding gradient (G_x) at the same time as the phase encoding gradient (G_y). The line in k-space is specified by the phase encoding gradient, while the frequency encoding gradient is responsible for moving k(t) to the minimum of k_x. The phase encoding gradient is then turned off, and the polarity of G_x is changed to positive, allowing the sampling of one line in k-space. This is repeated N_y times to allow the entire k-space to be sampled. In the current thesis, a three-dimensional version of a GRE sequence is used for anatomical imaging, table 3.1.

Echo Planar Imaging

SE and GRE represent the most basic sequences, but are not time efficient. EPI is a very time efficient sequence where gradients are used for refocusing, allowing the entire k-space

to be sampled using a single SE for SE or a FID for GRE. The scans in this thesis uses an SE-EPI sequence, SE-EPI is the most used DWI sequence. Due to only needing one SE, or just one RF-pulse, an entire image can be generated in less than 100ms [9]. While this technique is relatively insensitive to movement, it is very susceptible to other artifacts, and highly sensitive to the inhomogeneties in the magnetic field. To reduce the number of artifacts, multi-shot EPI can be used, this however increases the time it takes to reconstruct the image. Figure 2.9 shows an example of a single shot EPI. A similar readout, with SE prepared echo is used for the DWI in this thesis.

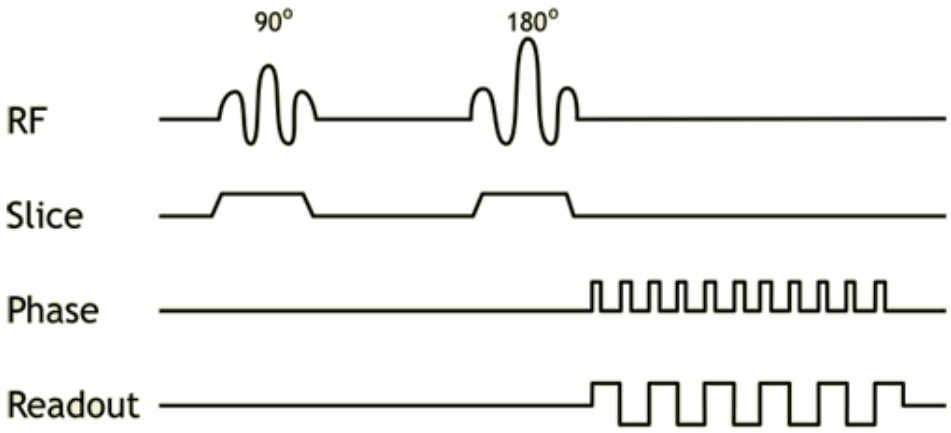

Figure 2.9: Single shot EPI sequence, using the gradients to read out the entire k-space in a single pulse.[17]

2.2 Diffusion

Diffusion is the net movement of particles, where each individual particle undergoes random Brownian motion. Although it is impossible to detect the movement of single particles in MRI, it is possible to detect the collective motion of a group of particles. MRI scans measure the apparent diffusion coefficient (ADC) since measuring the true diffusion constant is impossible, as the measured diffusion is dependent on perfusion. When doing an MR scan, the water moves around continuously while scanning, the dephasing of the water is therefore determined by the local microstructure around the water at the time of scanning, and since the signal is related to this dephasing, one can image with this in mind, thus creating a DWI. Since the scan can be very sensitive to these microstructures, any disease or damage to the local tissue can be detected through measuring the change in diffusion. In a volume where the water flows freely, the diffusion is isotropic, the same in all directions, in an environment where the water flows more easily in one direction, the diffusion anisotropic. In the tissues

inside of the body, one example is the white matter in the brain, the diffusion is not isotropic, since the flow is restricted by membranes and other barriers.

Biological Diffusion

Diffusion in biological tissues is complicated, since the tissues themselves are very complex. In tissues it is very important to have a long enough diffusion time, t_{diff}, so that the water has adequate time to diffuse. If t_{diff} is not long enough the water in the given volume does not have time to reach a barrier, and would give an isotropic diffusion read-out. It is therefore prudent to choose a t_{diff} so that the ADC will differ from the free isotropic diffusion. In a diffusion experiment the barriers are considered impossible to go through, even so, with a long enough t_{diff} water can permeate through these barriers. [19]

In DWI it is the anisotropy that is interesting, finding out in which direction the diffusion is hampered. When imaging white matter structures, the diffusion is much greater along the axons than across them, on of the factors leading to this is the myelin sheath acting as a barrier. In order to measure anisotropy in tissue, a tensor model must be estimated. The tensor must be described by six independent parameters, requiring at least six orthogonal measurements. It is common, however to measure in more than 60 directions.

Equation (2.35) gives the root mean square (RMS) displacement in one direction as a function of the measured ADC and the diffusion time. Combining the measured directions and the RMS displacement, the flow has a speed and direction.

$$< x^2 >^{\frac{1}{2}} = \sqrt{2(ADC)t_{diff}} \tag{2.35}$$

Diffusion Weighted MRI

DWI uses the previously discussed techniques in order to encode each voxel with information about water flow inside that volume. To do this, a sequence that is sensitive to motion is needed, one that differs from the traditional T1 or T2 weighting. The Stejskal-Tanner sequence is the basic one that achieves this, it combines SE with motion-sensitizing gradients to achieve the diffusion weighting.

Motion-sensitizing gradients is a technique, wherein the magnetic field gets manipulated in such a way as to make the protons precess at different rates. Since the protons continuously move around, when the second gradient pulse hits, with the same magnitude but opposite directions, there is an imperfect refocusing of spins. This leads to a signal loss proportional to the diffusion. This loss is formulated as equation (2.36)

$$\frac{S(TE)}{S_0} = exp[-\gamma^2 G^2 \delta^2 (\Delta - \frac{\delta}{3})\mathbf{D}] \tag{2.36}$$

This equation utilizes the gyromagnetic ratio(γ), the strength of the gradient pulse (G), duration of the pulse (δ), time between the pulses (Δ) and the diffusion coefficient D. The result is the ratio between the signal without diffusion weighting (S_0) and with ($S(TE)$). Figure 2.10 shows an imaging sequence with the added diffusion gradient.

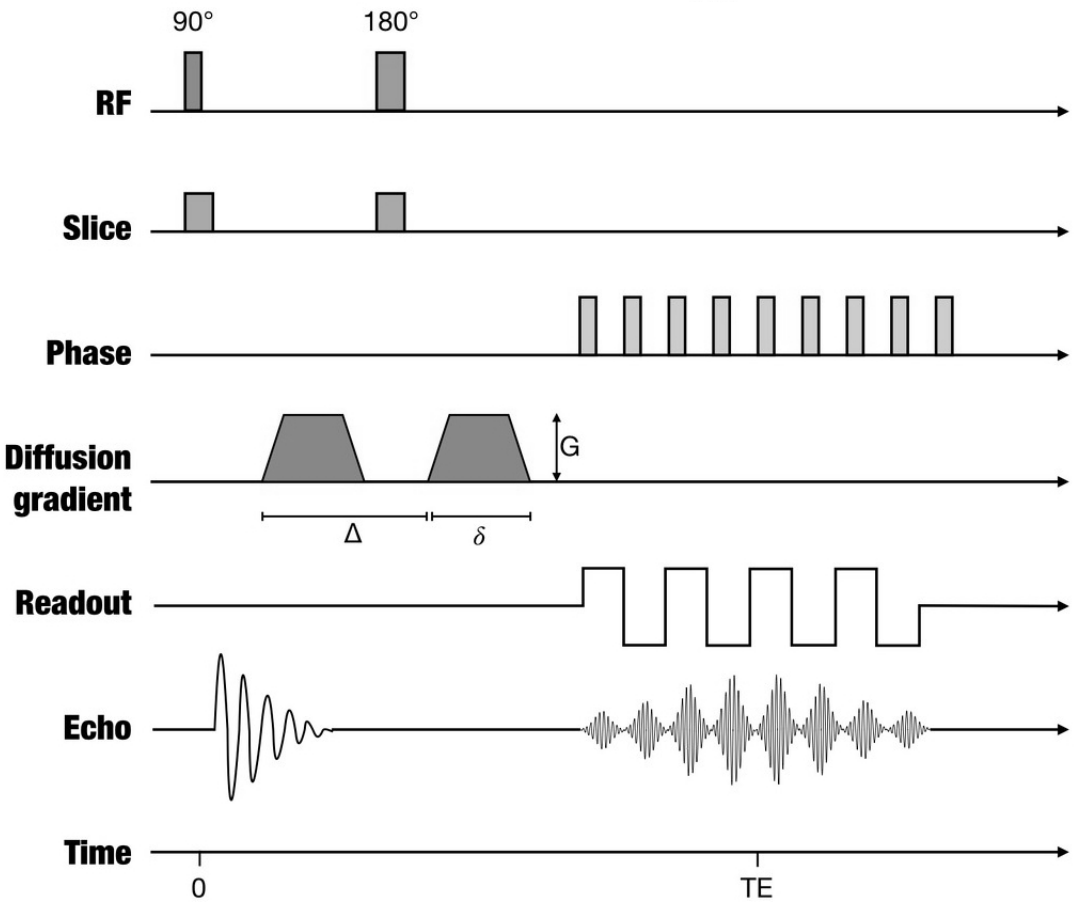

Figure 2.10: DWI sequence, showing all the relevant parameters. The b-value gathers the parameters in the added diffusion gradient. [18]

Because the sequence combines the normal localization gradients with the motion-sensitizing gradients, equation (2.36) becomes inaccurate. Cross-terms between all the pulses arise when the two different gradients are combined, in order to solve this problem, Bihan gathered all the gradient terms and created a factor that only depend on the parameters. This is called the b-value.

The b-value affects the degree of diffusion weighing, similar to how TE affects T2 weighing. Available b-values are generally in the range of $0s/mm^2$ to $4000s/mm^2$, but the most typical values are between $0s/mm^2$ and $1000s/mm^2$. The b-value can have a large impact on the imaged volume, as shown in figure 2.11, where the b-value is increasing from left to right. The image intensities have been normalized, this is done to show the effects of the changing b-value, if they were not normalized, the bottom two images (b-values of $1000s/mm^2$ and $2500s/mm^2$) would be almost completely black.

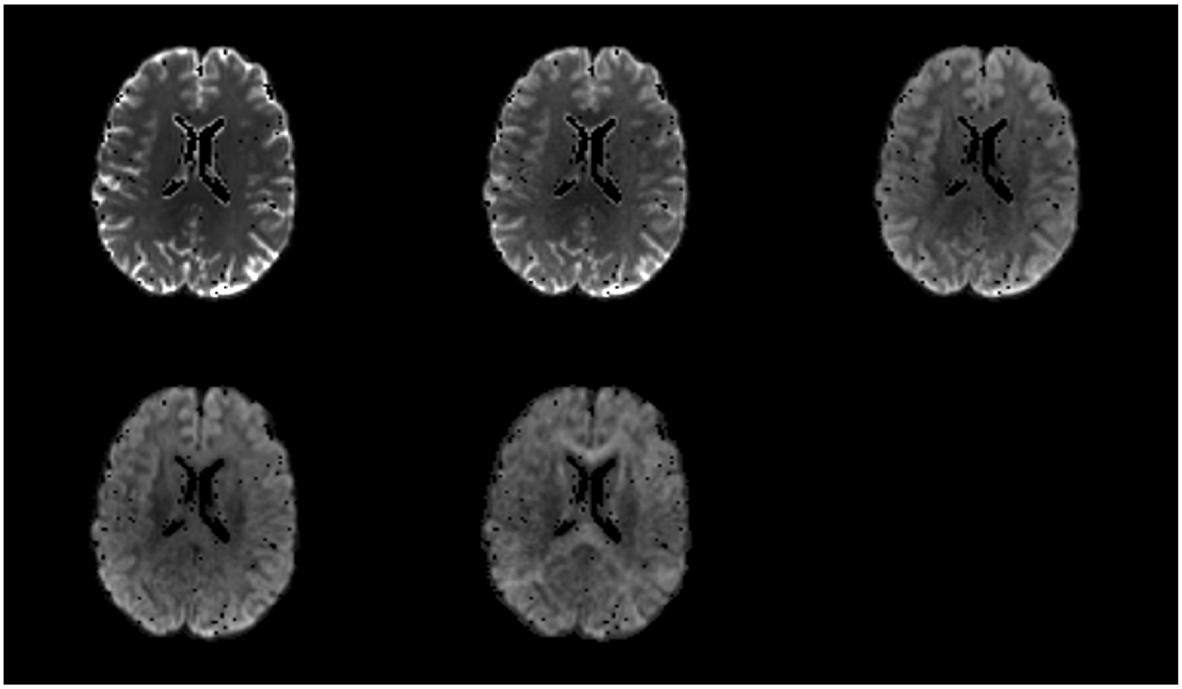

Figure 2.11: Normalized intensity image of the difference in the same brain with changing b-value. From left to right the b-values are: $0s/mm^2$, $250s/mm^2$, $500s/mm^2$, $1000s/mm^2$, $2500s/mm^2$

Diffusion is the flux of particles through an area, so the dimensions of ADC are $\frac{area^2}{time}$, therefore the b-value has to have the dimensions $\frac{time}{area^2}$ so that equation 2.38 is dimensionless. The formula for the b-value depends on the gradient pulse administered. The most common given formula for the b-value is the Stejskal-Tanner equation (2.37), but this is only valid for rectangular pulses.[21]

$$b = \gamma^2 G^2 \delta^2 (\Delta - \frac{\delta}{3}) \tag{2.37}$$

This equation depends on the magnitude (G), duration (δ) and interval (Δ). While the

b-value has a large theoretical range, larger b-values lead to more noise, it is therefore useful to restrict the b-value, a general rule of thumb is that $(b \cdot ADC) \approx 1$. By combining equations 2.37 and 2.36, equation 2.38 is created, where the b-value is used directly.

$$\frac{S(TE)}{S_0} = exp(-b \cdot ADC) \tag{2.38}$$

In clinical use, pure rectangular pulses are rarely used, for sinusoidal (2.39) and trapezoidal(2.40) the equations become.

$$b = 4\gamma^2 G^2 \delta^2 (\Delta - \delta/4)/\pi^2 \tag{2.39}$$

$$b = \gamma^2 G^2 [\delta^2 (\Delta - \delta/3) + \xi^3/30 - \delta\xi^2/6] \tag{2.40}$$

In this equation the new variable ξ denotes the rise time of the trapezoidal pulse.

Artifacts

Typically, DWI of the human brain is done using a SE prepared EPI readout. This approach allows a whole brain coverage with multiple b-values with reasonable acquisition time (5-10min). Common diffusion artifacts include susceptibility artifacts, ghosting, eddy current (shift, shear, contraction), and motion (physiology and body). Figure 2.12 shows the shift, shear, and contraction effect that eddy currents can have. Figure 2.13 shows examples of susceptibility and ghosting artifacts, the susceptibility artifact arises from the difference in magnetic susceptibility between the brain and the air surrounding.

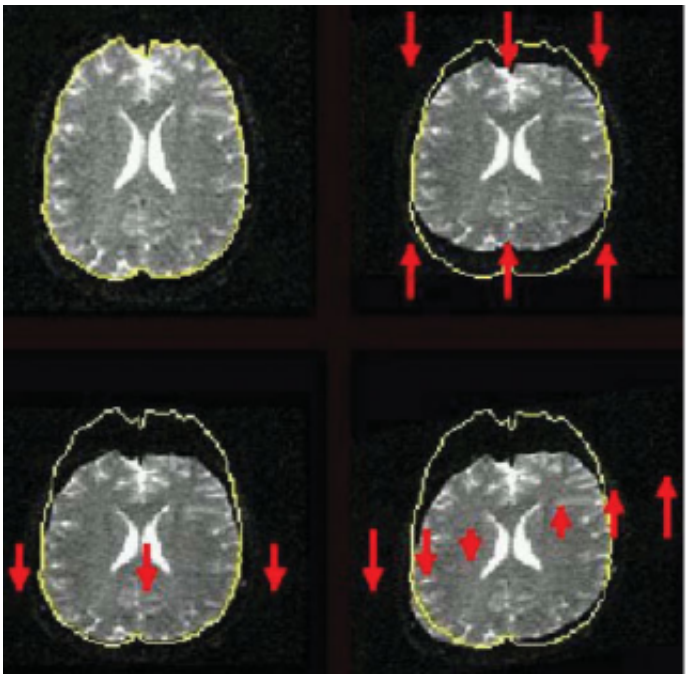

Figure 2.12: Eddy current artifacts, contraction(top), shift (bottom left), and shear(bottom right). [20]

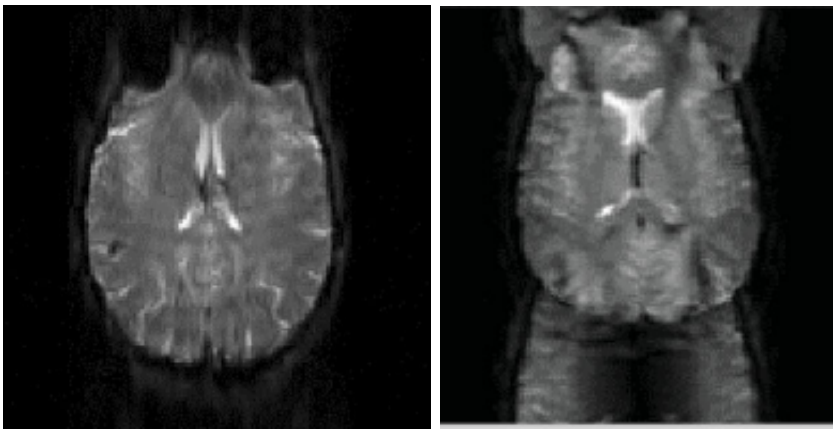

Figure 2.13: Susceptibility (left) and eddy current ghosting (right) artifacts.[20]

Ghosting can arise from both eddy currents and from motion, figure 2.13 shows the ghosting artifact caused by eddy currents. Due to the eddy currents changing the shape of the gradient pulse, a modulated signal in the phase-encoding direction appears. This modulation creates a difference in the echo center from line to line in k-space, and when Fourier transformed will cause the image to be duplicated at half the field of view, this artifact is also referred to as an "N/2" ghost. To reduce this, a scan without phase encoding

is used as a basis for determining the time-dependent phase shifts.[20]

2.2.1 Diffusion Tensor Imaging

DTI is a technique used in DWI in order to measure the directionally dependent diffusion. DWI is described by the single scalar ADC, but this is does not contain any information about the direction of diffusion, so a diffusion tensor **D** is introduced.

$$\mathbf{D} = \begin{bmatrix} D_{xx} & D_{xy} & D_{xz} \\ D_{yx} & D_{yy} & D_{yz} \\ D_{zx} & D_{zy} & D_{zz} \end{bmatrix} \tag{2.41}$$

In order to fill out the diffusion tensor, 6 directions needs to be measured in addition to a non-DWI (b = $0s/mm^2$), this is because the matrix is symmetric, in other words $D_{ij} = D_{ji}$ where i, j = x, y, z. Since D is now represented by a matrix and not a scalar, the echo attenuation equation changes from (2.36) to:

$$A = exp(-\sum_{i=x,y,z}\sum_{j=x,y,z} \mathbf{b_{ij}D_{ij}}) \tag{2.42}$$

Here the b-value has also changed from a single scalar to a matrix called **b**. [22]

In order to process the data from **D**, the reference frame is changed from [x, y, z] representing the laboratory frame, to [x', y', z'] representing the diffusion frame. The matrix is the diagonalized and the eigenvalues λ_1, λ_2, and λ_3 are the main directions of diffusivity. These are always determined so that $\lambda_1 > \lambda_2 > \lambda_3$.

Invariant Indices

In order to evaluate the DTI data, the need for invariant indices arises, the most common ones are the following.

$$MD:\ mean\,diffusivity = \frac{\lambda_1 + \lambda_2 + \lambda_3}{3} \tag{2.43}$$

$$RA:\ relative\,anisotropy = \sqrt{(\lambda_1 - \langle\lambda\rangle)^2 + (\lambda_2 - \langle\lambda\rangle)^2 + (\lambda_3 - \langle\lambda\rangle)^2}/3\langle\lambda\rangle \tag{2.44}$$

$$FA:\ fractional\ anisotropy = \sqrt{3(\lambda_1 - \langle\lambda\rangle)^2 + (\lambda_2 - \langle\lambda\rangle)^2 + (\lambda_3 - \langle\lambda\rangle)^2}/\sqrt{2(\lambda_1^2 + \lambda_2^2 + \lambda_3^2)} \tag{2.45}$$

$$VR:\ volume\ ratio = \lambda_1\lambda_2\lambda_3/\langle\lambda\rangle^3 \tag{2.46}$$

In all the equations $\langle\lambda\rangle = (\lambda_1+\lambda_2+\lambda_3)/3$. MD, equation 2.43 describe the mean diffusivity in the given voxel. RA, equation 2.44, is the ratio between anisotropy and isotropy in $\mathbf{D}$, while FA, equation 2.45, describes to what extent the magnitude of $\mathbf{D}$ can be ascribed to the anisotropy. RA and FA ranges from 0 to 1, isotropy to anisotropy respectively in both cases. The last one is VR, equation 2.46, this is the ratio between the ellipsoid volume $\lambda_1\lambda_2\lambda_3$ and the volume of a sphere with radius $\langle\lambda\rangle$. [23] VR ranges from 1 to 0, where 1 is isotropic diffusion and 0 is anisotropic diffusion, this confusion leads to some using (1-VR) instead, so that there is consistency in what the numbers represent.[24] Due to its higher resistance to noise and higher contrast-to-noise ratio, FA maps are generally more used than RA maps. [25]

Three other rotationally invariant indices used in this thesis contain information pertaining to the shape of the eigenvector. These indices are described by the equations (2.47 2.48 2.49) [26]. Cl, cp, and cs denote the linear, planar, and spherical anisotropy respectively.

$$cl:\ linear\ anisotropy = \frac{\lambda_1 - \lambda_2}{\lambda_1 + \lambda_2 + \lambda_3} \tag{2.47}$$

$$cp:\ planar\ anisotropy = \frac{2 \cdot (\lambda_2 - \lambda_3)}{\lambda_1 + \lambda_2 + \lambda_3} \tag{2.48}$$

$$cs:\ spherical\ anisotropy = \frac{3 \cdot \lambda_3}{\lambda_1 + \lambda_2 + \lambda_3} \tag{2.49}$$

λ_{123} denote the largest to the smallest components of the eigenvector, where λ_1 is always the primary direction.

Fiber Tractography

Water flows more freely along the axons than across them, the diffusion should then be greatest along the fibers. This is the idea behind mapping the neuronal fiber paths of the brain. One method of doing this is by assuming that the largest eigenvalue (λ_1) of $\mathbf{D}$ points in the same direction as the fiber tracts and therefore, the neuronal fiber path in the analyzed voxel. [27]

The methods for reconstructing the fiber paths vary in complexity, where each has flaws and strengths. They usually require a starting point, where the principal directions are found, which determines the next voxel to be analyzed, the same is then done for this voxel and so on. This method belongs to the line propagation algorithm group of techniques, they vary mainly in how to treat information from neighboring voxels in order to recreate the actual fiber tract. The other main group works by calculating the path of least resistance between two points. For line propagation, the voxel data is used to create a 3D vector field, where the most basic approach is to assign one direction to the whole voxel, then move on to the next. This technique has an obvious flaw, there might be more than one fiber tract through a given voxel. Other problems arise when for example two fibers merge then go apart again, the algorithms might not be able to follow the fibers correctly after separation. The other case is bad resolution, then the insufficient data will lead to phantom tracts, where the algorithm thinks there is a particular diffusion pattern that corresponds to white matter. In fiber tract visualization, the most common technique is to color code each tract depending on what direction the fiber goes, the image generated is very useful for the big picture of neuronal fiber paths in the brain. [28]

There are two ways of determining seeding, one involves only using seeds within a given ROI, the other calculates the entire brain by setting a given number of seeds in each voxel. The first technique uses a given ROI as the starting point and sets the seeds in each voxel within that ROI for the reconstruction. This technique is efficient when considering computation time and memory demands, it will however, miss fiber tracts that might be close to the ROI, this can cause misleading fiber tracts to be formed and an anatomically incorrect image generated. The other technique is the brute-force method, in this method the entire brain is done at once, each voxel will have a number of seeds specified by the parameters set before the calculation. The brute-force method is the technique mainly used, due to the much lower risk of incorrect fiber paths. The problem with the brute-force method is hardware related, it requires much more memory and a higher computational capability when compared to the ROI-based technique. [29] Figure 2.14 shows the fiber tracts of a random brain calculated using the brute-force technique.

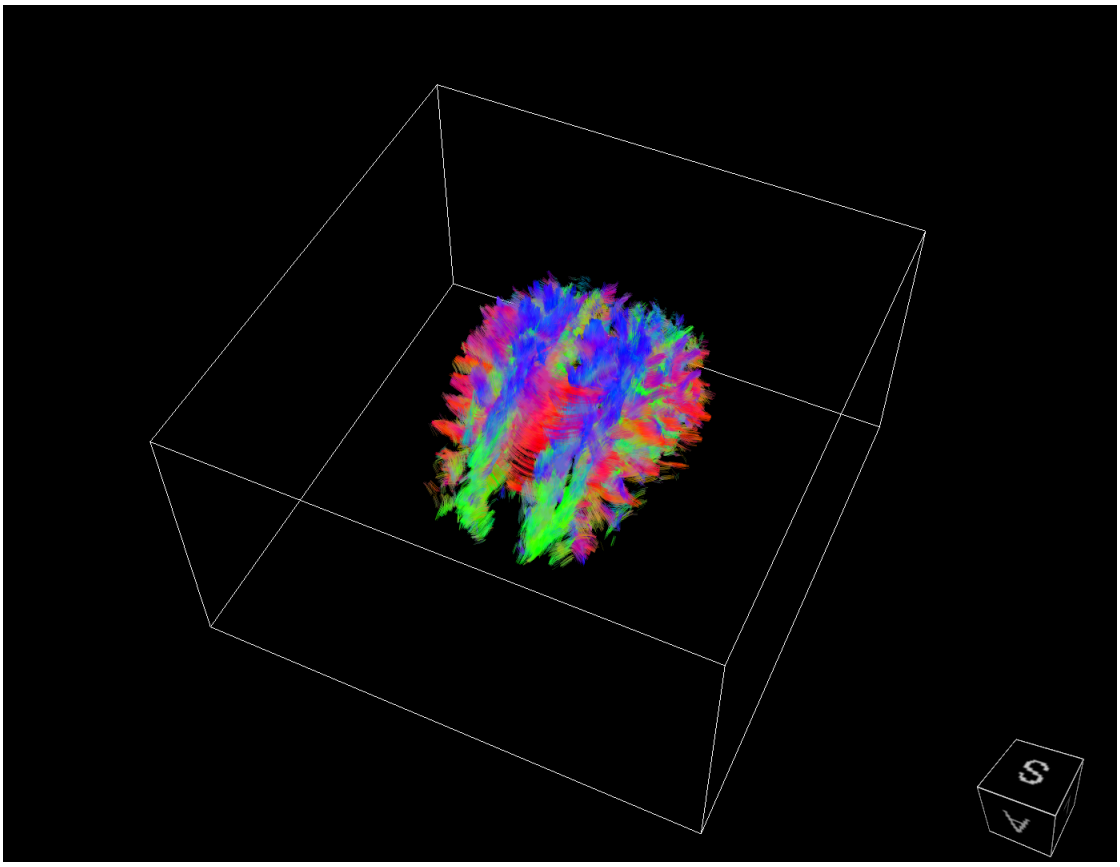

Figure 2.14: Fiber tracts of a random brain(NordicIce, Nordic NeuroLabs inc. Bergen, Norway). The colors represent the directions of water flow in the brain.

The most important parameters affecting the results of the reconstruction are: The minimum FA threshold and the maximum turning angle between voxels. The minimum FA threshold is the lowest FA required for the algorithm to continue a fiber tract in that direction, it is typically set between 0.1 and 0.3 for adults. Lowering this parameter further will lead to longer and more numerous fibers, it will also increase the number of false-positives. This is caused by the FA being set so low that the algorithm can not distinguish the noise from true-positives due to the SNR, or wrongly assume that isotropic tissue belong to the fiber structure.

The turning angle is usually set between 40° and 70°, higher angles are used when the fiber tracts being investigated contains hairpin turns. Increasing the angle also dramatically increases the number of false-positive fiber paths. When using the brute-force method, it also severely increases the computational load on the computer, due to the aforementioned dramatic increase in fiber paths, both true-positive and false-positive.

2.2.2 Free Water Elimination Model

limitations of Conventional Models

Traditionally the DWI models used in both animal and clinical settings are simple models. Most used are the ADC maps that simply map the ADC value of each voxel throughout the volume. These have the advantage that they are simple, have a proven track record, shorter scans, and short computation times. These maps can be generated online, while the more advanced models have to be computed offline and analyzed at a later time.

The disadvantage of these simple ADC maps is that they do not differentiate between different pathologies. A high ADC score means that the voxel volume has a high diffusivity, this could be caused by one of several sources, whether it is an indication of a disease or just temporary damage is impossible to tell without scanning again at a later date. Detecting the myelin is practically impossible in a conventional diffusion analysis since the volume fraction of the myelin is minute. Grey matter is another disadvantage, ADC maps have low sensitivity to grey matter changes. ADC maps also have severe uncertainties in tissue that is located close to CSF or large fiber tracts, such as the corpus callosum, due to the high water content leading to an artificially inflated ADC, and therefore, inaccurate DTI analysis.

Free Water Elimination

In order to combat the uncertainties mentioned earlier regarding the conventional diffusion models around tissue with high water content, a new model, FWE, was recently introduced by Prof Pasternak (Dept of Radiology, Harvard Medical School, Boston). [2] The FWE model assumes that within each voxel there is a part that is free water, for example CSF or edema.

It is possible to suppress the CSF signal by using the fluid-attenuated inversion recovery diffusion-weighted imaging sequence (FLAIR-DWI). This sequence does not however, correct contaminations caused by edemas, and does not allow for gating in order prevent artifacts caused by physiological processes.

The model starts off by attempting to predict the attenuation caused by free water contamination by describing it as the sum of two attenuations, the tissue compartment, $\mathbf{C}_{tissue}$ and the free water compartment $\mathbf{C}_{water}$. The bi-tensor is written as equation 2.50. This bi-tensor was first proposed by Pierpaoli and Jones [30], but the first proposed model had a severe fitting issue. The model proposed by Pasternak et al fixed the fitting issue by having several more measurements. [2]

$$\mathbf{A}_{bi-tensor}(\mathbf{D}, f) = \mathbf{C}_{tissue} + \mathbf{C}_{water} = f\mathbf{A}_{tissue}(\mathbf{D}) + (1-f)\mathbf{A}_{water} \tag{2.50}$$

In this equation $\mathbf{A}_{bi-tensor}(\mathbf{D}, f)$ represents the attenuation vector for each voxel, where $\mathbf{D}$ contains an entry for each applied gradient direction, and f is the tissue fraction in the voxel. The tissue compartment is expressed as equation 2.51.

$$[\mathbf{A}_{tissue}(\mathbf{D})]_k = exp(-b\mathbf{q}_k^t \mathbf{D}\mathbf{q}_k) \tag{2.51}$$

In equation 2.51, b is the b-value, $\mathbf{q}_k$ is the k-th applied gradient direction, $[\cdot]_k$ denotes the k-th entry in a vector. $\mathbf{D}$ is the diffusion tensor.

One assumption that is made in the constructing of the free water compartment is that there is no exchange of water molecules between voxels, another assumption is that the free water attenuation is a scalar expressed by equation 2.52.

$$[\mathbf{A}]_k = exp(-bd) \tag{2.52}$$

In this equation b is the b-value, and $d = 3 \cdot 10^{-3} mm^2/s$ is the free water ADC at 37°C. The bi-tensor model has to be fitted for two variables, f and $\mathbf{D}$, this is done by minimizing the distance between calculated attenuation and measured attenuation. Measured attenuation is a vector comprised of the DWIs normalized by the b0 images. It is possible to choose any arbitrary f- value ($0 < f \leq 1$), and get a corresponding $\mathbf{D}$ that fits the data, therefore, there are in theory infinite (f,$\mathbf{D}$) couples.

Due to noise it is very unlikely that there is a perfect fit of the (f,$\mathbf{D}$) couples, and so, a global minimum is selected among several local minima. In order to choose the correct minimum, additional constraints are added. The first is to require a smooth continuity between voxels. This represents the continuous diffusivity between voxels in the same tissue, so unless two neighboring voxels belong to different tissues, the expectation is that the tissue compartment is smooth.

A further reduction of the solution space is achieved by adding constraints to the volume fraction, f. Originally this is set to be $0 < f \leq 1$. This range can however be limited by the expected diffusivity in a given tissue. By applying this restriction, a contraction on both side is achieved, since the tissue is also expected to have a minimum diffusivity, a new range $f_{min} < f < f_{max}$ is then calculated for each voxel. By applying this, the free water portion is calculated and can be removed from the original data set. [2]

By eliminating this part of the data, the DTI indices should more accurately represent the underlying tissue. This is done by utilizing a bi-exponential expansion of DTI, as shown in equation 2.53.

$$S_i = S_0[fexp(-bD_{iso}) + (1-f)exp(-bg_i Dg_i)] \tag{2.53}$$

Here, f is the same as above, it is a matrix of the same dimensions as the original DWI data. D Is the tissue diffusion tensor. D_{iso} is the same free water diffusion coefficient as was used in equation 2.52, b is the diffusion weighting factor.

By utilizing equation 2.53, the effect of the free water contamination can be estimated and removed from the data set. This will remove the effect of contamination from, for example the CSF or an edema when calculating anisotropy or other indices. In fiber tractography, this process will remove false positives and false negatives caused by free water contamination.

Applications of FWE

FWE has been shown to be an effective technique in various cases; Parkinson's disease [31], Alzheimer's disease [32], schizophrenia [33], even physical injuries like concussions [34]. MS has however, never been studied using FWE, even though it is a disease that mainly attack the white matter and should lead to noticeable lower anisotropy within this brain region.

MS is a chronic, inflammatory and demyelinating disease that affects the central nervous system. Macroscopically this presents itself as lesions within the white or gray matter, the lesions cause damage to the blood-brain barrier leading to a local oedema. [35] The lesions are visible on an MRI scan, and show up differently depending on the contrast used. The microscopic demyelination caused by MS damages the myelin sheath that surrounds the axons. The myelin sheath is a cylindrical sheath that has the same effect as the insulation around a cable, its job is to reduce the current loss to the environment, thus ensuring faster information transport in the nerves. This sheath is also what stops water from diffusion isotropically as it acts like a membrane that hinders water diffusion, demyelination then, will be detectable as a lowering of anisotropy where it happens.

This is why MS is a good fit for FWE analysis. The demyelination of the nerve fibers should be more readily detectable when the free water contamination is removed, revealing the loss of anisotropy attributable to the demyelination. MS can also have varying degrees of remyelination, this will increase the local anisotropy and might hide the disease, demonstrating the importance of longitudinal study, with new scans at regular intervals. [35]

2.3 Project Aim

The aim of the current thesis is to evaluate the effect of the FWE model on the estimation of the diffusion indices described in section 2.2.1. Based on the current information, the indices are expected to change in the direction of higher anisotropy, this will not be a uniform change across the different brain tissues analyzed. By removing a spherical contribution from the free

water diffusion, all eigenvalues are assumed to be reduced by approximately the same value, it is then also assumed that the relative change will differ between the three eigenvalues.

The selected ROI in corpus callosum lies within a structure in the brain with very well defined fibers going in the same direction, it will therefore be affected by the correction to a smaller degree than the grey matter, an area of relatively high estimated isotropy due to much less defined fiber orientations. White matter is expected to be affected by the free water correction to a smaller degree than the grey matter and the whole brain due to more well defined fiber orientation. In fiber tractography, it is expected that FWE will increase the number of fibers found, due to an increase in FA and removal of free water contamination that might hide potential fiber tracts.

The effect of FWE should however, be significant for the large regions, but not necessarily for the ROI in corpus callosum due to the homogeneity of the region covered, and because the manual placement of the ROI might lead to more noise. The difference between the two groups is expected to be small, while MS is a demyelinating disease leading to a higher degree of isotropy, it is recently diagnosed and is not expected to have made enough of an impact to be seen in the whole brain analysis, but might be visible in the white matter analysis.

This thesis will not comment on the effect of FWE on the anatomical accuracy of the data. It will investigate the tissue dependency of FWE, and to a smaller degree the spatial dependency. This is done by comparing the non corrected and corrected data in selected brain regions; whole brain analysis, segmented white and grey matter, and a small region-of-interest analysis in the corpus callosum. The same analyses will then be redone on participants with recently diagnosed MS to see how the free water correction affects the indices in someone who has a known neurodegenerative disease. The white matter of the participants with MS should be different than that of the healthy volunteers if the demyelination has progressed enough. By removing the free water contamination, a more accurate estimation of the diffusion indices is achieved. The data gathered on the participants with MS could be used as a starting point for a longitudinal study in the effect of FWE on MS after it has progressed more.

Chapter 3

Methods

3.1 MRI Acquisition

All image acquisitions were performed on a whole body 3 Tesla MRI Prisma system (Siemens Healthineers Inc, Erlangen, Germany) using a vendor provided 20 channel head coil. The machine is located at the Department of Radiology at Haukeland University Hospital.

All patients were scanned using the same EPI diffusion sequence. Some of the parameters used in the sequence are outline in table 3.2. The sequence parameters used for extracting the brain volume in the pre-processing stage is outlined in table 3.1.

3D T1 Weighted	
Parameter	Value
Flip angle	8°
FoV	256mm x 256mm
Voxel size	1mm x 1mm x 1mm
Matrix	256 x 256
Nr. of slices	192
TR/TE	1800ms/2.28ms
TA	07:42
BW	200 Hz/Px

Table 3.1: Imaging parameters for the brain volume extraction used in pre-processing. FoV = field of view, TR = repetition time, TE = echo time, TA = acquisition time, and BW = bandwidth.

DTI 74shots TE82	
Parameter	Value
Flip angle	90°/180°
FoV	256mm x 256mm
Voxel size	2mm x 2mm x 2mm
Matrix	128 x 128
Nr. of slices	72
Nr. of B0 images	5
Nr. of directions	69
TR/TE	9000ms/82ms
TA	12:00
BW	1502 Hz/Px
b-values	[0, 250, 500, 1000, 2500]s/mm^2

Table 3.2: Diffusion protocol parameters. FoV = field of view, TR = repetition time, TE = echo time, TA = acquisition time, and BW = bandwidth.

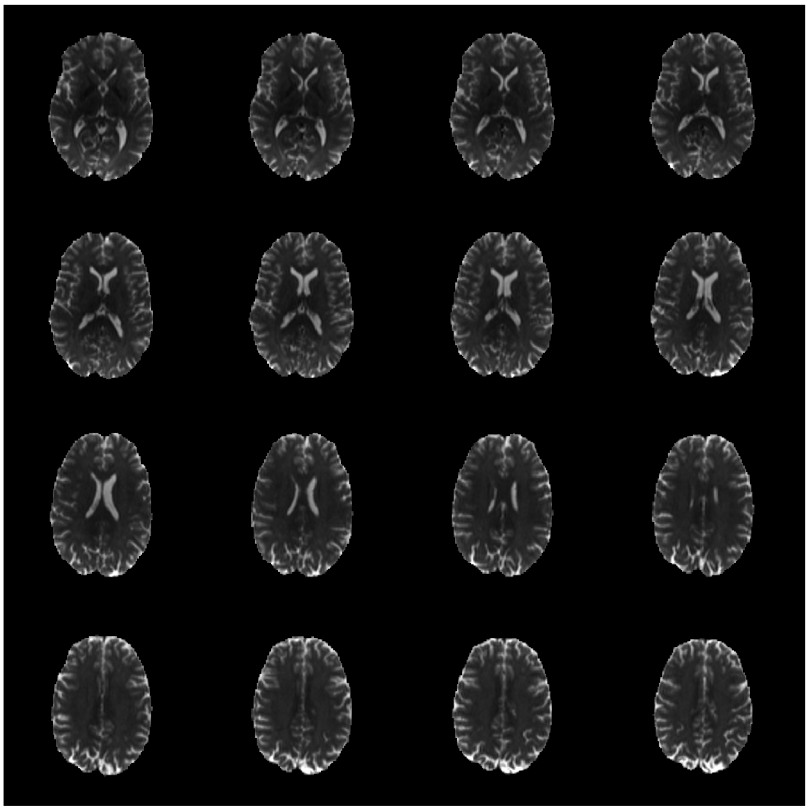

Figure 3.1: Montage of 16 out of 17 slices used in the analysis, the images are B_0 images from a random brain.

This is part of an extensive imaging protocol in an ongoing study on brain microstructure and function in healthy volunteers, section (3.2.1), and participants with newly diagnosed MS, section (3.2.2). Imaging parameters were determined based on an active collaboration with Prof Pasternak (Dept of Radiology, Harvard Medical School, Boston) as were initial estimations of subsequent voxelwise free water estimations. All images were software corrected to reduce the eddy current artifacts before analysis. Figure 3.1 shows 16/17 slices used in the analysis.

3.2 Study Participants

The age difference between the two groups were not significant (P=0.04), table 3.3 due to one outlier in the group of healthy volunteers.

Group	N	Mean (yrs)	Std (yrs)
Healthy Volunteers	20	30	12
Participants with MS	20	43	14

Table 3.3: Mean age of participants at the time of imaging.

3.2.1 Healthy Volunteers

Image data (structural 3DT1 and diffusion image data) from a group of healthy volunteers were used to study the effect of FWE by comparing the diffusion estimates before and after correction. The participants were randomly selected from two large ongoing image studies by the Bergen fMRI group on brain function and structure (the EMNDMN study and the DLvisCue study). Image data were acquired following all ethical guidelines. For the current evaluation, only anonymized image data and the individual participant ages were available.

3.2.2 Participants with MS

Image data (structural 3DT1 and diffusion image data) from a group of MS patients were included in the current evaluations. The participants were randomly selected from a larger ongoing clinical follow up study, BICAMS (Brief International Cognitive Assessment in MS) aiming at investigating cognitive function in an early stage of MS. The image data were acquired following ethical guidelines, and only age was provided with the double-blinded image data of each participant. The image data were from the first baseline examinations, this means that all the participants with MS are recently diagnosed and not medicated, they are currently in their third follow-up visit.

It is beyond the current thesis to discuss any clinical implications of the evaluations performed, the data are not linked to the clinical patient scores. The reason for including this group is to have a preliminary investigation into the effects of FWE on a patient population, and because this is the first such evaluation in this particular patient group, the thesis is an important contribution to the upcoming analyses of the complete data material.

3.2.3 Group Comparison

To have a valid comparison, all image data were acquired using identical MRI systems and identical imaging protocols. The average age in the MS group was higher than the healthy volunteers, this is a result of the random selection of participants. None of the participants were excluded from the evaluations of the current thesis.

3.3 Image Analysis

FWE was done using scripts written in MatLab (Mathworks inc., Massachusetts, USA). Estimates of the free water portion f, described in section 2.2.2, were provided by a "black-box" analysis provided by the collaborators in Boston (Prof. Pasternak et al). Additional programming was performed as part of this thesis to apply the free water correction to the DWIs.

3.3.1 Overview of Image Analysis

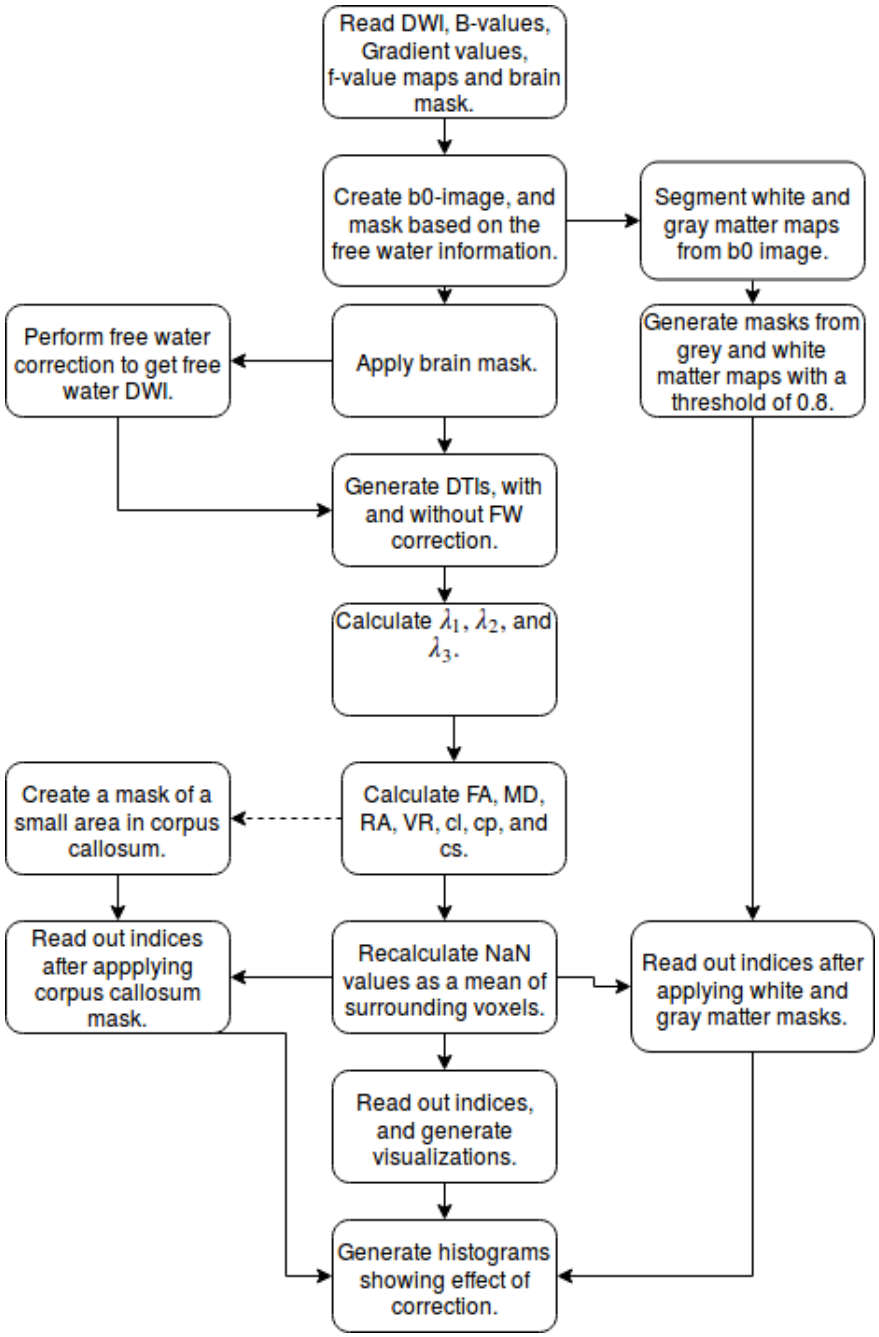

Figure 3.2: The workflow from scan to index calculation.

Figure 3.2 shows the workflow diagram of the analysis. From the diffusion image, the relevant diffusion measures are extracted before and after the application of FWE. White and grey matter are segmented using the spm package (Matlab, Mathworks inc. Massachusetts, USA).

Figure 3.3 shows the masks used for the grey and white matter segmentation data, and table 3.4 has the total number of voxels in these masks. The top image is the mask created for the white matter with a threshold of 80%, meaning that it covers area that is 80% likely to be white matter. The same threshold is applied to the grey mask, the middle image, the bottom image is of the b0 image used for the segmentation. The b0 image is the average of the 5 b0 images provided in the data set, this is done for each participant. In order to avoid corruption of the results due to the brain segmentation cutting off large sections of the lower part of some of the participants, 17 slices from the middle of the brain were used.

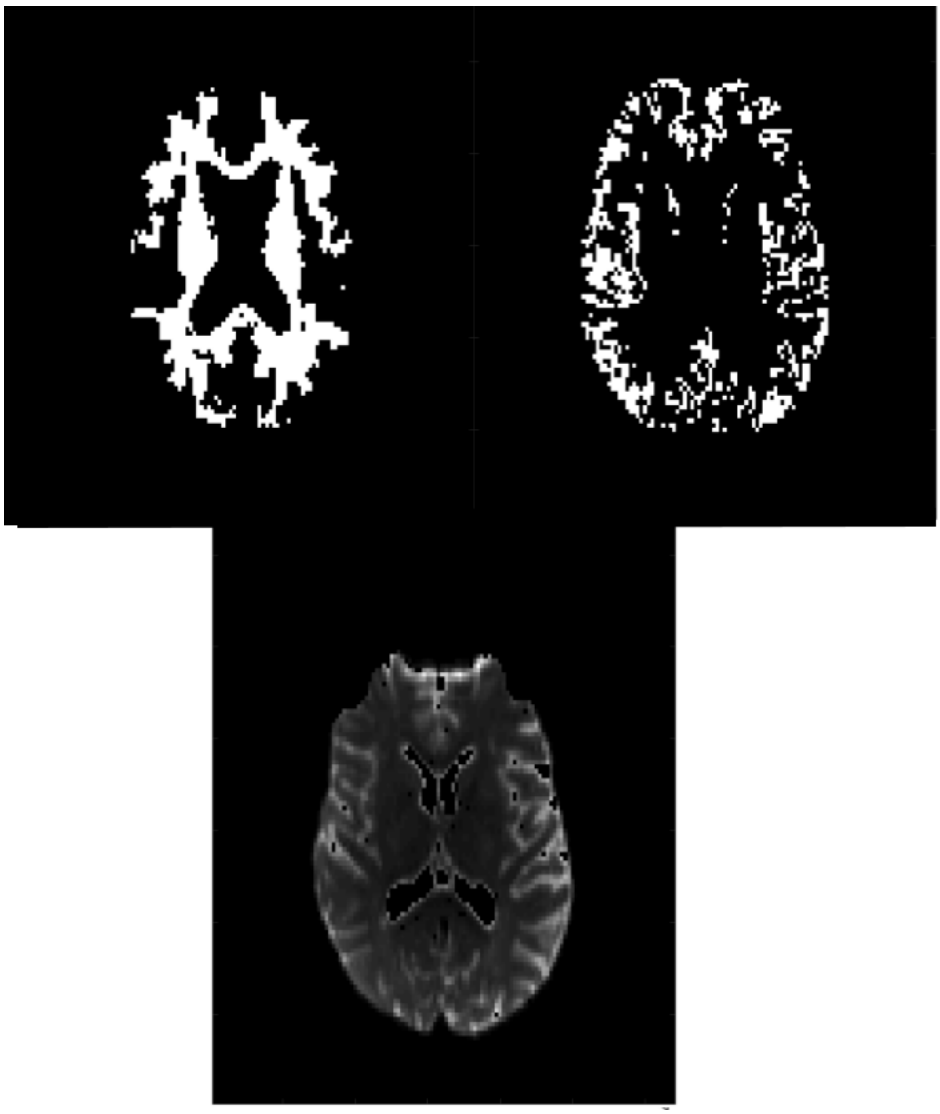

Figure 3.3: White(left) and grey(right) matter masks estimated from the b0 image(bottom) in each participant.

The images are then corrected for free water, as shown originally by Pasternak et al. [2]

Mask	No. of voxels	Std
Grey matter	21135	7742
White matter	21635	3884
Grey matter MS	17510	3849
White matter MS	22158	3628

Table 3.4: The average total number of voxels covered by the grey and white matter segmentation masks.

In order to do this, the script DWI2FWI.m is used, mathematically equation 2.53 is changed to 3.1.

$$\frac{\frac{S_i}{S_0} - f \cdot exp^{(-bD_{iso})}}{1-f} = exp^{(-bg_i D_{gi})} \tag{3.1}$$

The right side of the equation is then put used as input in the DWI2DTI.m script to get the free water corrected DTI. The same data points are then extracted from this FWE corrected data set in order to compare it to the non-corrected data. These two data sets are then compared using ttest2 (MatLab, Mathworks inc., Massachusetts, USA) function to determine significance.

3.3.2 Implementation

The masterscript, imagesearch.m, lists all the subfolders with MRI data in the given folder. It then parses the folder name to the main script, where the data points to be compared are calculated and sent back into the masterscript. The data is used to fill out a matrix where a statistical significance test, ttest2 (MatLab, Mathworks inc., Massachusetts, USA), is run in order to determine the significance of the correction. All of these data points are then organized written out to the main folder.

The main script, main.m, reads in the NIFTI, the masks, gradient values, free water map, and b-values from the folder specified by the ID input given by the masterscript. The nifti file when read has the dimensions 128x128x72x76 where the last two dimensions represent the slices and gradient directions respectively.

A mask is created based on the free water map in order to be able to gather data from the same voxels and exclude effects from the ventricles. This new mask is then applied to the data set before proceeding with the analysis.

A baseline image is needed for the calculation of the DTI, this image is created by taking the average of all b=0 images and setting it as the first image when sorting by gradient directions. The elements in the gradient and b-value matrix are removed where b=0, so that

the matrices have the same amount of directions after the baseline image is created, this does not have any adverse effect on further calculation because at b=0 all the gradients are zero.

The free water is eliminated from the DWI by utilizing equation 3.1, dwi2fwi.m, the free water corrected DTI is calculated from the free water corrected DWI. This returns a free water corrected DTI and DWI, used for evaluating the effect of FWE. The corrected DWI and DTI are saved in folders based on the ID provided at the beginning for easy access later, or analysis in an external program.

Once the DTIs are created, the eigenvalues, λ_{123}, are calculated. The invariant indices are then calculated from λ_{123}, These are cl, cs, cp, FA, MD, VR, and RA, as described in section 2.2.1. These are the values used in comparing the non-corrected with the corrected data.

Due to the free water mask containing several NaN values, a recalculation of those NaN values is performed. This is done by using the recalc.m script, this script goes through all the voxels in the given image and checks for two things, whether or not the voxel is within the brain mask, and whether or not the voxel contains a NaN value. This value is then recalculated so that it equals the average of a 3x3 voxel box with the NaN value in the middle.

All the indices are written to tables for comparison and graphed together to better determine the effect of FWE graphically. These graphs are saved in the same folder as the corrected DWI and DTI. Images are also generated of the brain to better visualize the change when correcting for free water. Difference images are generated by taking the absolute value difference between the free water data from the non-corrected data and dividing by the non-corrected data. The absolute value is used to better visualize where the change happens, but it does lose some information as to what direction the change is, this was deemed the best approach due to the difficulty in discerning small differences when using the $[-1, 1]$ scale. The MatLab scripts in their entirety are provided in Appendix A.

3.3.3 Fiber Tractography

The fiber tractography was done using NordicIce(NordicNeuroLabs Inc., Bergen, Norway). The DWI data is read in and run through the fiber reconstruction in the program with varying parameters, keeping one constant and varying the others. Limits on the parameters were due to computational limitations, the minimum fiber length was kept at 5mm, while cutoff angle and FA threshold were variable. Brute-force whole-brain tracking was used in order to not miss any tracks that can be overlooked using the ROI-based seeding as laid out in 2.2.1.

A very thin ROI is then created in corpus callosum, this is an area where the fibers are

highly organized, therefore, small changes should be easily discernible. Data is then read out and compared to see how the free water correction has affected fiber tractography in a region of high diffusion. The ROI is created to the best of my ability, with no formal training in neurology, it is drawn based purely on the conceptual understanding that corpus callosum is the area where the fibers connecting the two brain halves lie.

In order to compare the fiber tractography between the corrected and non-corrected data, varying parameters were used. The termination angle and the FA threshold were variables, while the minimum fiber length was kept constant at 5mm. The termination angle was set to be $30° - 60°$ in steps of $10°$ giving three separate termination angle values. Likewise, the FA threshold was set to be $0.100 - 0.300$ in steps of 0.100 giving a total of three different threshold values. This resulted in 9 points of comparison used for the fiber tractography part. To get a visualization of the fiber tractography, the FA threshold was set to $FA > 0.300$ with a termination angle of $60°$.

3.4 Statistical Analysis

To determine if the change induced by the free water correction is significant, ttest2 (MatLab, Mathworks Inc. Massachusetts, USA) was used. This is a two-sample t-test used to determine if the data in two vectors are from two samples with different means and different variance. To determine significance, the threshold was set to $p < 0.01$.

The two-sample t-test was performed on the means of the indices from FWE and conventional DTI, meaning that there were 20 data points in each sample group. The test was performed on the 20 participants in the healthy volunteers and participants with MS separately.

Chapter 4

Results

4.1 Healthy Volunteers

4.1.1 Eigenvalues

Whole Brain Analysis

All the eigenvalues were reduced when the free water component is removed from the original data. The largest eigenvalue (λ_1) is less reduced than the middle (λ_2) and smallest eigenvalue (λ_3) in all subjects, table 4.1. The relative decrease in value goes like $\lambda_1 < \lambda_2 < \lambda_3$.

Index	Mean (10^{-4})	Std (10^{-4})	P-value	Change(%)
λ_1	7.9	0.3		
$\lambda_1 FW$	6.2	0.1	$p < 0.01$	-21.95
λ_2	6.5	0.3		
$\lambda_2 FW$	4.7	0.1	$p < 0.01$	-26.61
λ_3	5.7	0.2		
$\lambda_3 FW$	3.96	0.05	$p < 0.01$	-30.12

Table 4.1: The eigenvalues from 20 healthy volunteers, FW denotes free water corrected values, showing a larger relative decrease in λ_1 compared to λ_{23}.

Figure 4.1 shows the histogram of table 4.1.

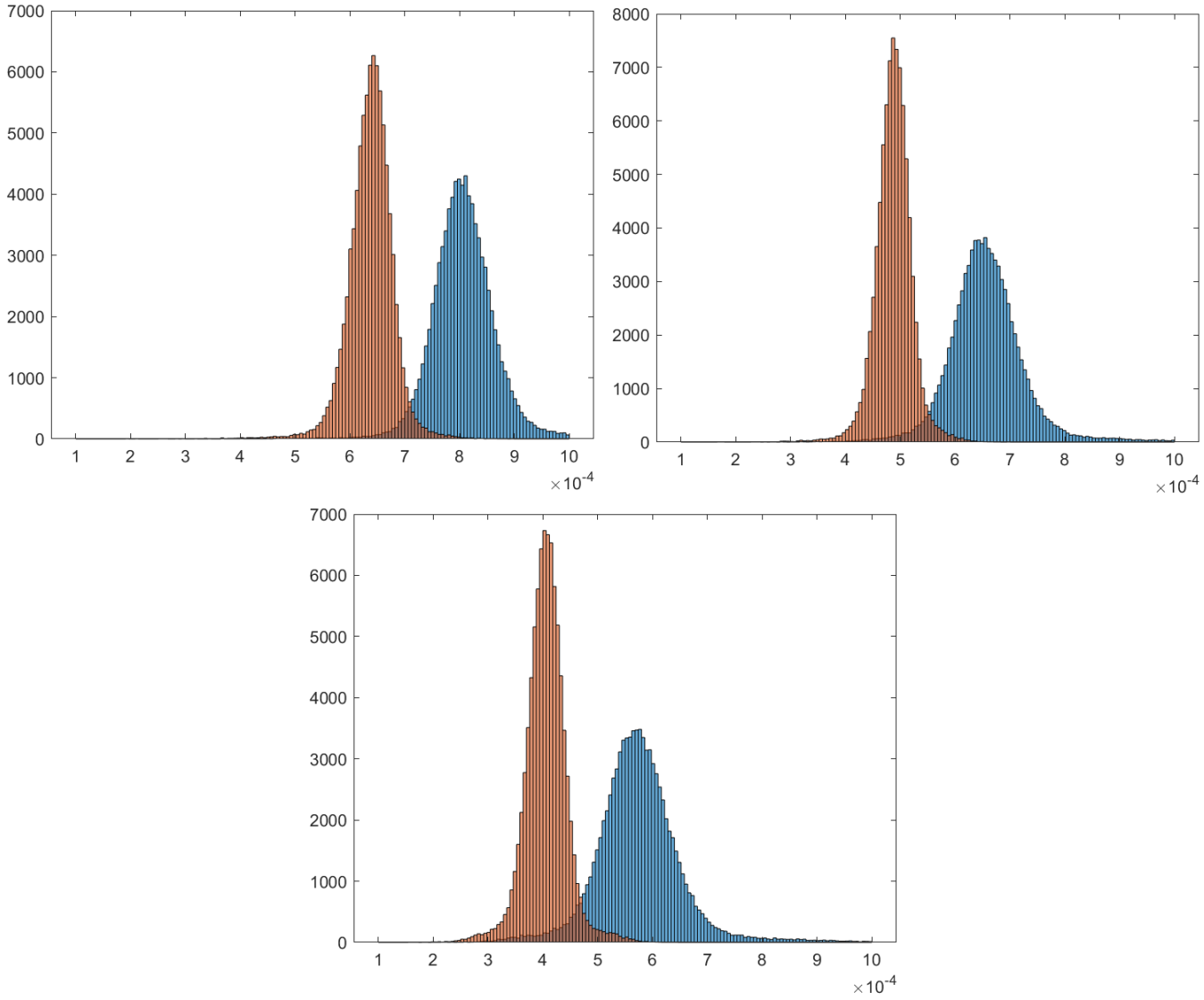

Figure 4.1: The three eigenvalues from top left: λ_1, λ_2 and λ_3 (bottom). Orange represents the free water correction data.

Grey Matter Analysis

Segmenting out the areas that are most probably grey matter, $> 80\%$ probability, allows the measuring of the effect of FWE on the grey matter, table 4.2 and figure 4.2. The grey matter had more similar λ_{123}, than the whole brain analysis, before the free water correction. The free water correction increased the difference between λ_{123}, but not to the same degree as the whole brain, white matter, or corpus callosum.

Index	Mean(10^{-4})	Std(10^{-4})	P-value	Change(%)
λ_1	8.0	0.5		
$\lambda_1 FW$	6.5	0.3	$p < 0.01$	-19.50
λ_2	7.0	0.4		
$\lambda_2 FW$	5.5	0.3	$p < 0.01$	-22.28
λ_3	6.4	0.3		
$\lambda_3 FW$	4.8	0.2	$p < 0.01$	-24.58

Table 4.2: λ_{123} for the segmented grey matter part of the brain.

The decrease in λ_{123} is significant, and similar to what was observed for the whole brain analysis.

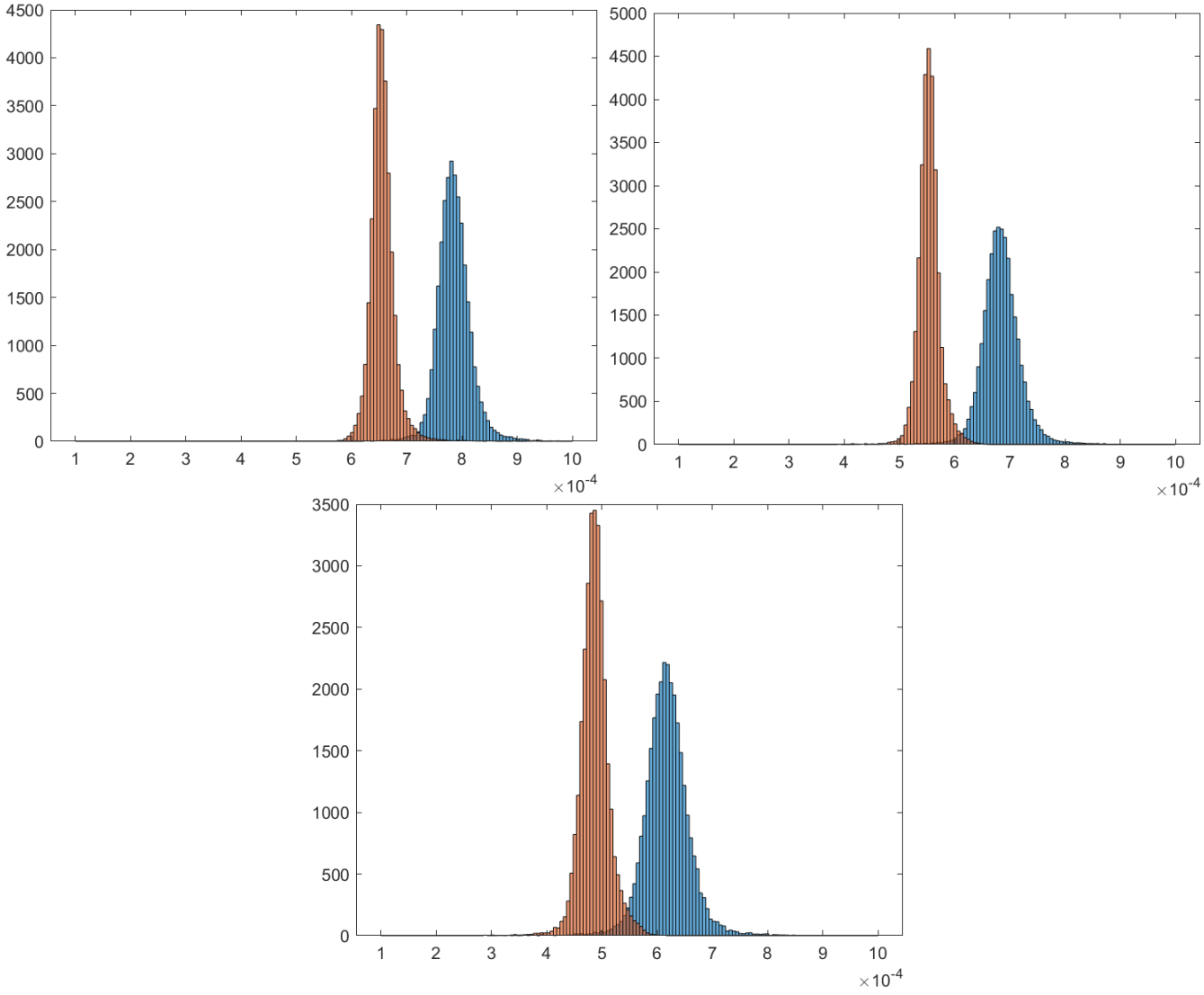

Figure 4.2: The three eigenvalues from the grey matter segmentation, from the top left: λ_1, λ_2 and λ_3 (bottom). Orange represents the free water correction data.

White Matter Analysis

The difference between λ_1 and λ_{23} when looking at the segmented white matter, table 4.3, is higher before and after correction compared to indiscriminately looking at the whole brain, table 4.1, or the grey matter segmentation, table 4.2.

Index	Mean (10^{-4})	Std(10^{-4})	P-value	Change (%)
λ_1	7.57	0.08		
$\lambda_1 FW$	6.88	0.07	$p < 0.01$	-9.11
λ_2	5.0	0.2		
$\lambda_2 FW$	4.33	0.04	$p < 0.01$	-13.90
λ_3	3.9	0.2		
$\lambda_3 FW$	3.2	0.1	$p < 0.01$	-18.12

Table 4.3: λ_{123} for the whole brain in the segmented white matter.

After correction there is a larger difference between λ_1 and λ_{23} than in the indiscriminate whole brain analysis. Suggesting a larger general anisotropy in the white matter portions of the brain. Additionally there is a lower general spread when compared to the grey matter. Figure 4.3 shows the histograms of table 4.3.

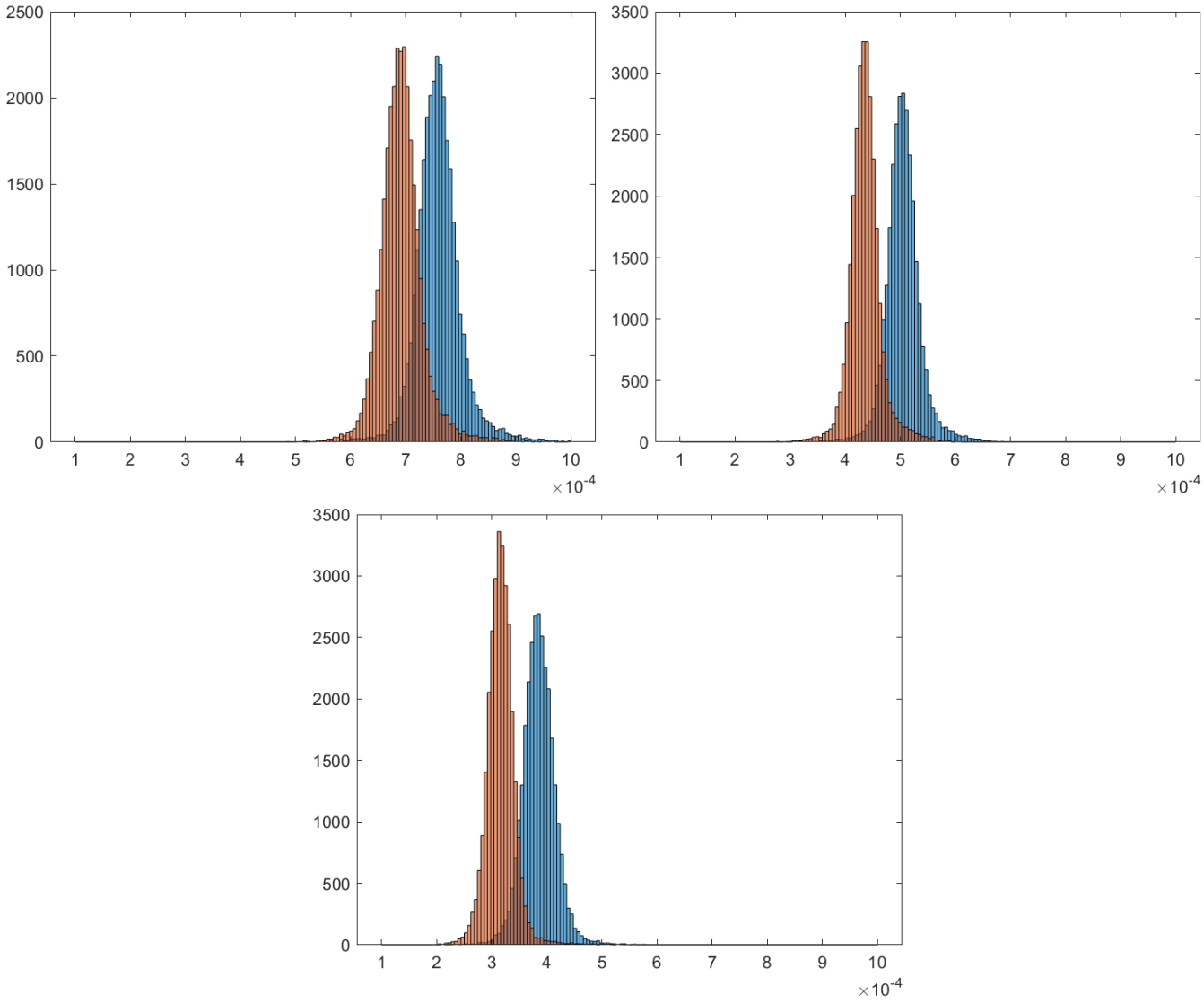

Figure 4.3: The three eigenvalues from the white matter segmentation, from the top left: λ_1, λ_2 and λ_3 (bottom). Orange represents the free water correction data.

Selected ROI in Corpus Callosum

The selected ROI in corpus callosum, hereby referred to as just corpus callosum, has a more pronounced difference in the indices, $\lambda_1 >> \lambda_2, \lambda_3$, table 4.4, than in the white matter, table 4.3, the whole brain, table 4.1, or the grey matter, table 4.2. This is due to the structure of corpus callosum, it is a region of high homogeneity, clearly defined fiber paths and a high degree of anisotropy.

Index	Mean (10^{-4})	Std (10^{-4})	P-value	Change(%)
λ_1	9.0	0.2		
$\lambda_1 FW$	8.4	0.3	$p < 0.01$	-6.18
λ_2	3.19	0.09		
$\lambda_2 FW$	2.6	0.1	$p < 0.01$	-17.95
λ_3	2.5	0.1		
$\lambda_3 FW$	1.96	0.09	$p < 0.01$	-22.33

Table 4.4: The eigenvalues (λ_{123}) in a small area in Corpus Callosum.

Figure 4.4 shows the histogram of table 4.4. Figure 4.5 shows the ellipsoids created by the eigenvalues in corpus callosum, in the non-corrected(top) and corrected(bottom) case. The axes have been kept the same to show the decrease in all eigenvalues in addition to the more pronounced λ_1. Figures 4.6, 4.7, and 4.8 shows λ_{123} respectively. In all three figures, the top left image is the non-corrected, the top right image is corrected, and the bottom image is the difference between the two, higher intensity denotes larger change.

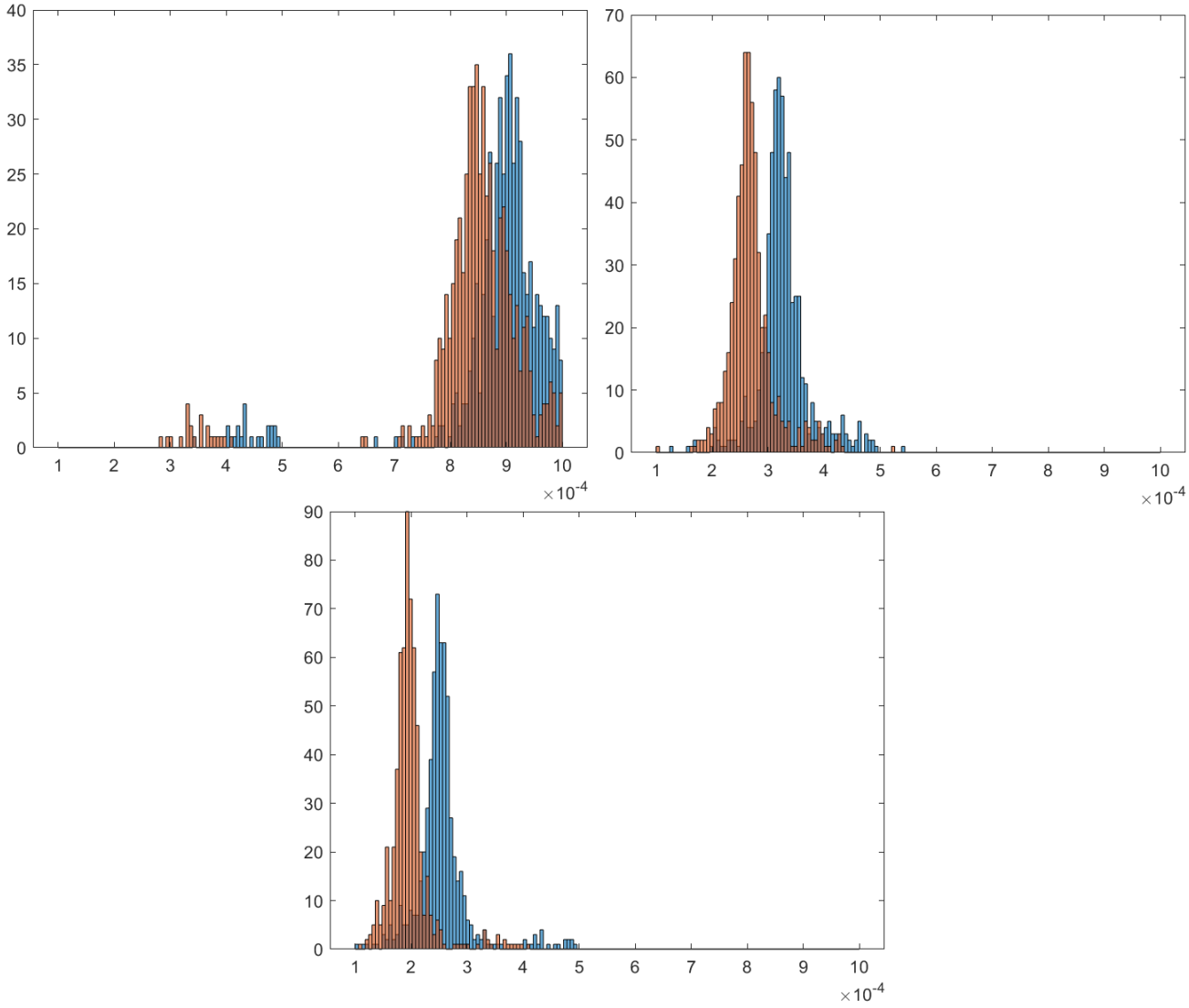

Figure 4.4: Histograms of λ_{123} in corpus callosum. From top left to bottom: $\lambda_1\,\lambda_2\,\lambda_3$. Orange represents the free water correction data.

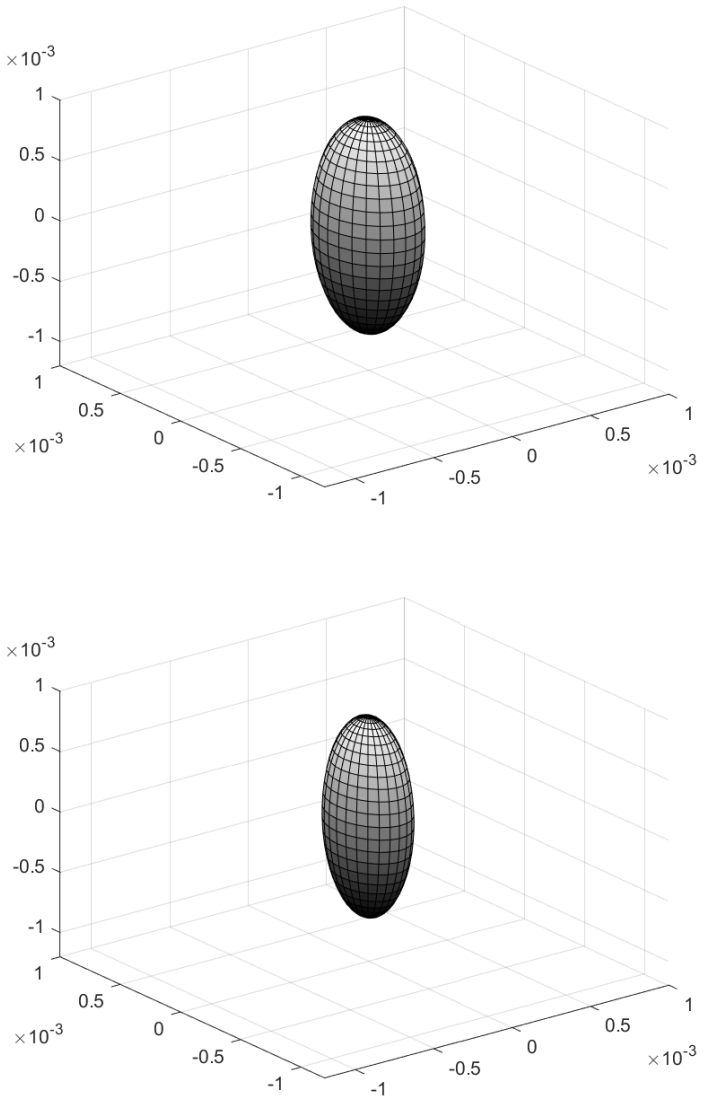

Figure 4.5: Ellipsoids constructed using λ_{123}, from corpus callosum, the non-corrected ellipsoid is on top and the corrected is on the bottom. Axes are set to the same scale for a better comparison.

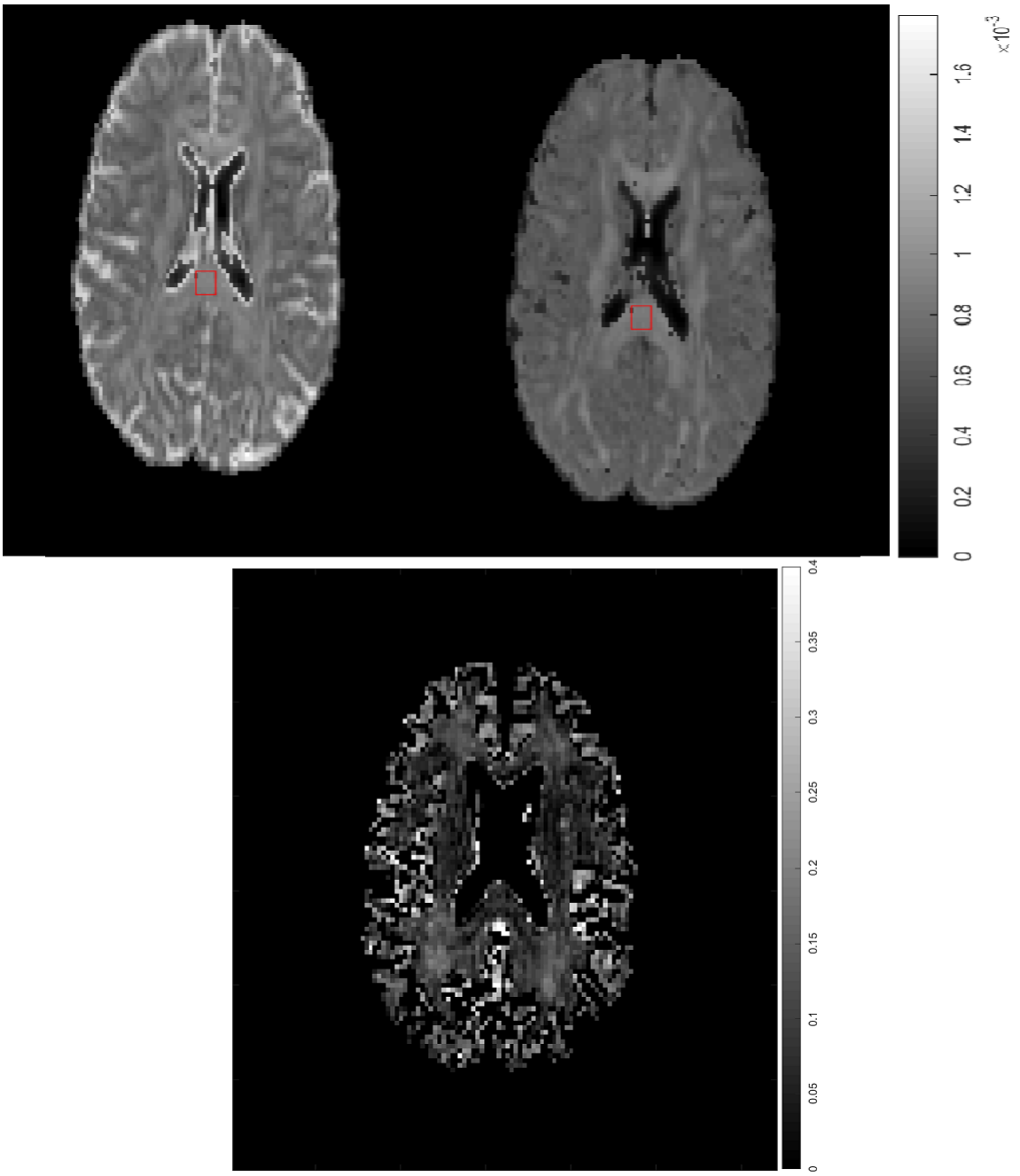

Figure 4.6: λ_1, the top left and right are the non-corrected and corrected visualizations respectively. The bottom is the difference image.

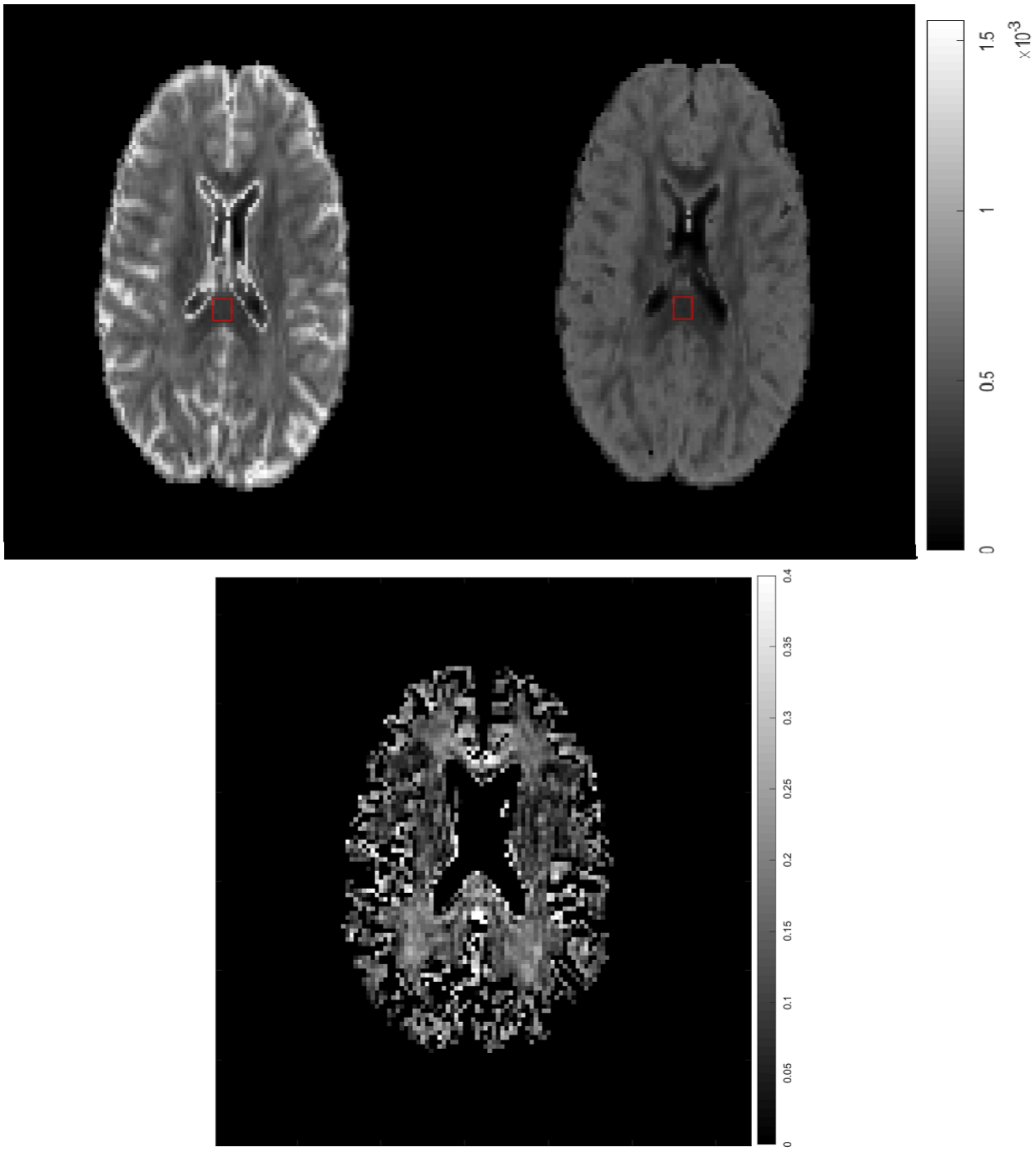

Figure 4.7: λ_2, the top left and right are the non-corrected and corrected visualizations respectively. The bottom is the difference image.

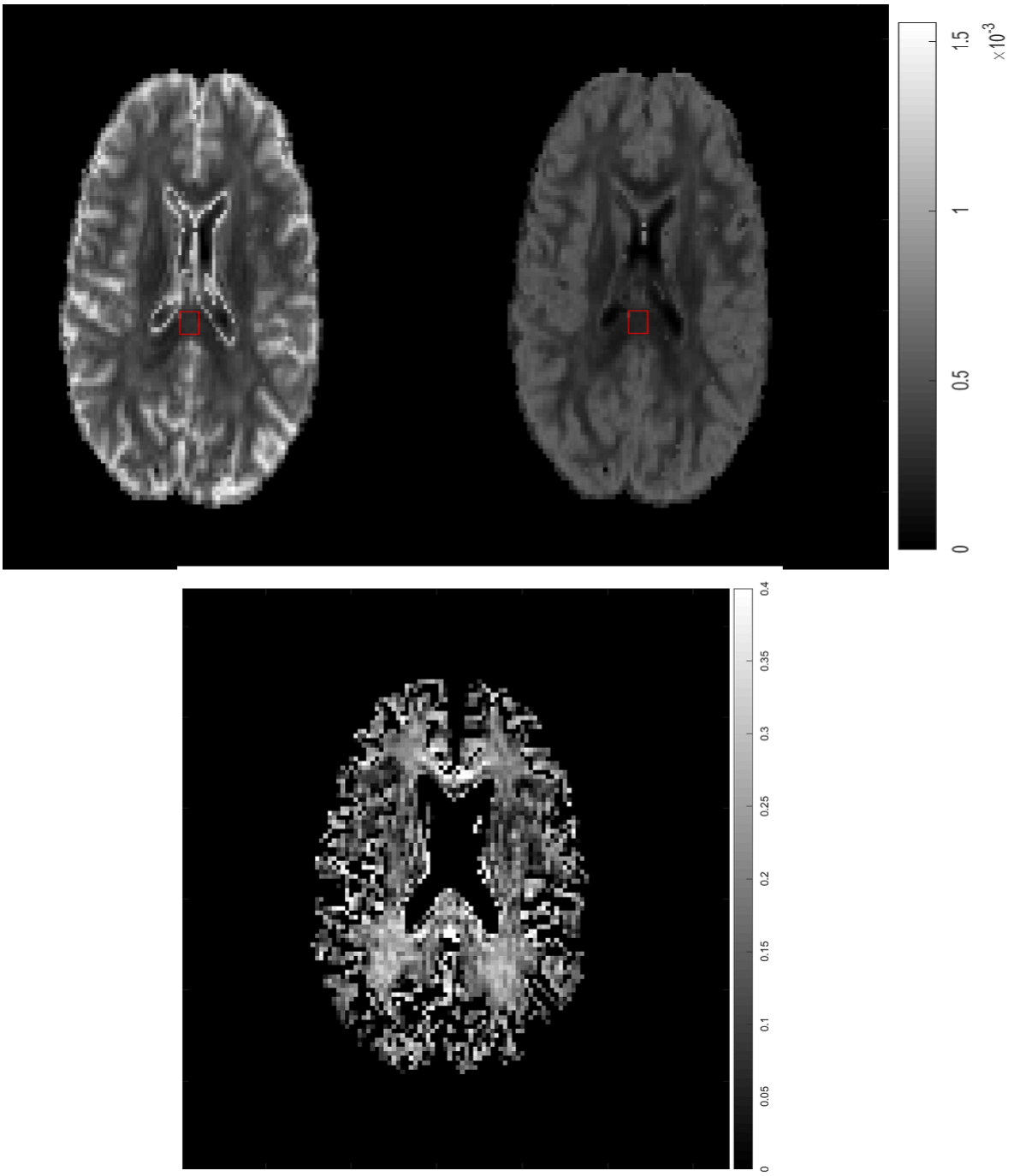

Figure 4.8: λ_3, the top left and right are the non-corrected and corrected visualizations respectively. The bottom is the difference image.

4.1.2 Anisotropy and Diffusivity

Whole Brain Analysis

The anisotropy indices, FA, MD, RA, and VR, show a significantly higher degree of directionality after the free water correction, table 4.5 and figure 4.9. The influence of FWE on the microstructure of the brain is significant, this is reflected in the anisotropy indices, as well as in λ_{123}, table 4.1.

Index	Mean	Std	P-value	Change(%)
FA	0.20	0.01		
FA-fw	0.237	0.009	$p < 0.01$	18.05
MD(10^-4)	6.7	0.3		
MD-fw(10^-4)	5.0	0.1	$p < 0.01$	-25.77
RA	0.095	0.008		
RA-fw	0.114	0.006	$p < 0.01$	19.20
1-VR (10^{-2})	6.2	0.1		
1-VR-fw(10^{-2})	8.1	0.1	$p < 0.01$	31.13

Table 4.5: Values of FA, MD, RA, and VR for non-corrected and free water corrected data.

Due to the higher relative value of the primary eigenvalue after the correction, FA, RA, and VR, has increased substantially. Likewise due to the reduction in all eigenvalues after the correction, MD has decreased.

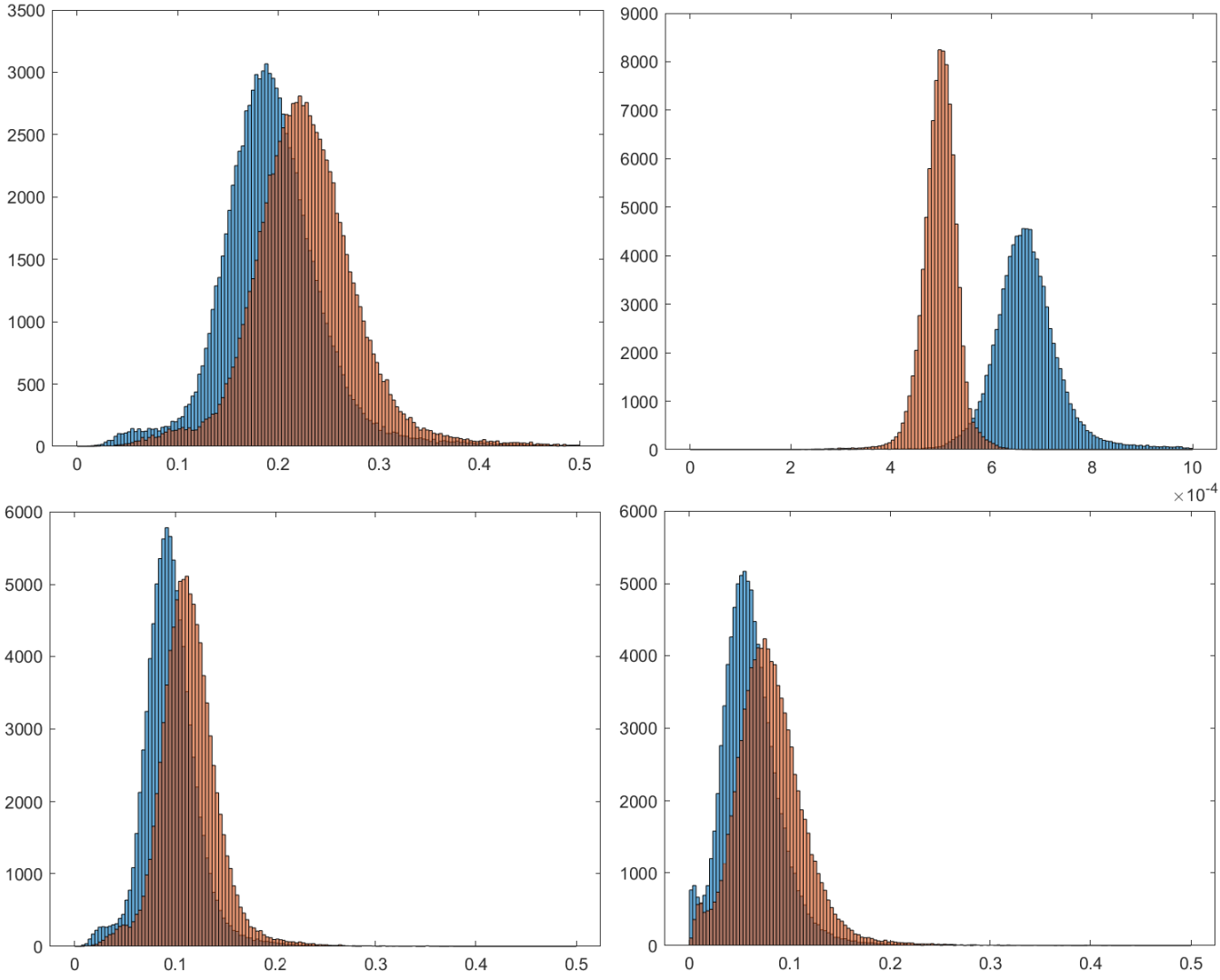

Figure 4.9: Histograms of FA, MD, RA, and VR from the whole brain analysis. From top left to bottom right: FA, MD, RA, VR. Orange represents the free water correction data.

Grey Matter Analysis

Grey matter is inherently more isotropic, table 4.6 and figure 4.10, than the rest of the brain, table 4.5. The free water correction had a larger relative effect in the grey matter than the whole brain, but even correcting for free water contamination, grey matter remains the most isotropic region of the brain. This is due to the chaotic nature of the fiber structure of the grey matter, complicating the task of determining a primary direction in each voxel.

Index	Mean	Std	P-value	Change(%)
FA	0.13	0.02		
FA-fw	0.15	0.02	$p < 0.01$	21.83
MD(10^{-4})	7.1	0.5		
MD-fw (10^{-4})	5.6	0.3	$p < 0.01$	-21.93
RA	0.060	0.008		
RA-fw	0.074	0.008	$p < 0.01$	22.53
1-VR(10^{-2})	2	1		
1-VR-fw(10^{-2})	3	1	$p < 0.01$	42.83

Table 4.6: FA, MD, RA, and VR for the segmented grey matter in the brain. There is generally less anisotropy in the grey matter parts, when compared to the brain in general.

As expected, the anisotropy is lower than when looking at the brain as a whole, when segmenting white matter, or when looking at a small area in corpus callosum. There is still a significant increase in anisotropy when removing the free water portion in the grey matter.

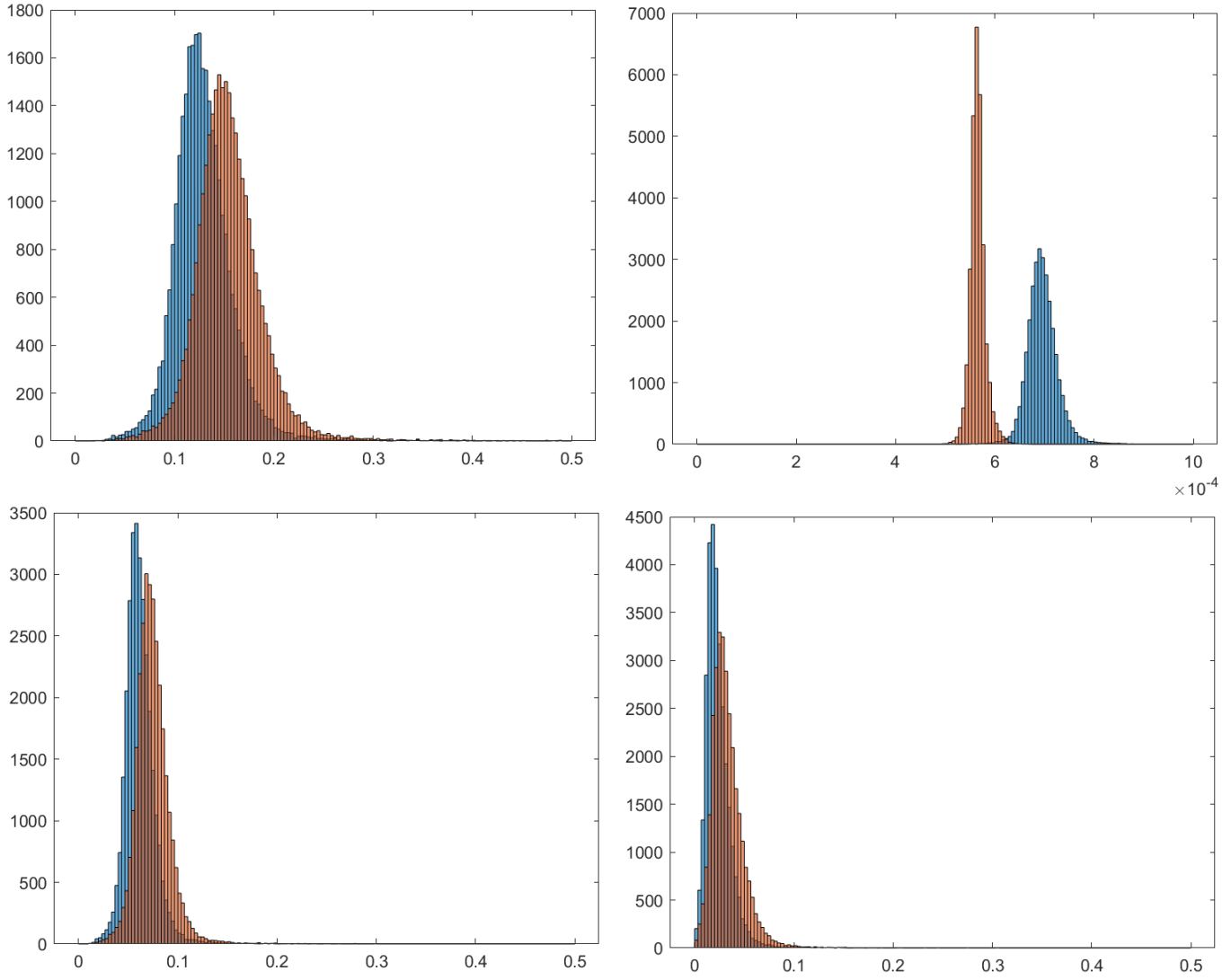

Figure 4.10: Histograms of FA, MD, RA, and VR from grey matter. From top left to bottom right: FA, MD, RA, VR. Orange represents the free water correction data.

White Matter Analysis

White matter is the most aniostropic large region of the brain, the indices are therefore also larger, table 4.7, than the other two major regions, grey matter and the whole brain. The free water correction has a significant impact on all indices. Due to the inherently higher degree of anisotropy, the free water correction induced the smallest relative change when compared to the other major regions.

Index	Mean	Std	P-value	Change(%)
FA	0.340	0.009		
FA-fw	0.381	0.009	$p < 0.01$	12.16
MD(10^{-4})	5.5	0.2		
MD-fw (10^{-4})	4.80	0.06	$p < 0.01$	-12.16
RA	0.171	0.006		
RA-fw	0.195	0.006	$p < 0.01$	14.12
1-VR(10^{-2})	13	1		
1-VR-fw(10^{-2})	17	1	$p < 0.01$	26.58

Table 4.7: FA, MD, RA, and VR for the segmented white matter in the brain. Anisotropy is generally higher in these parts of the brain when compared to grey matter or the whole brain.

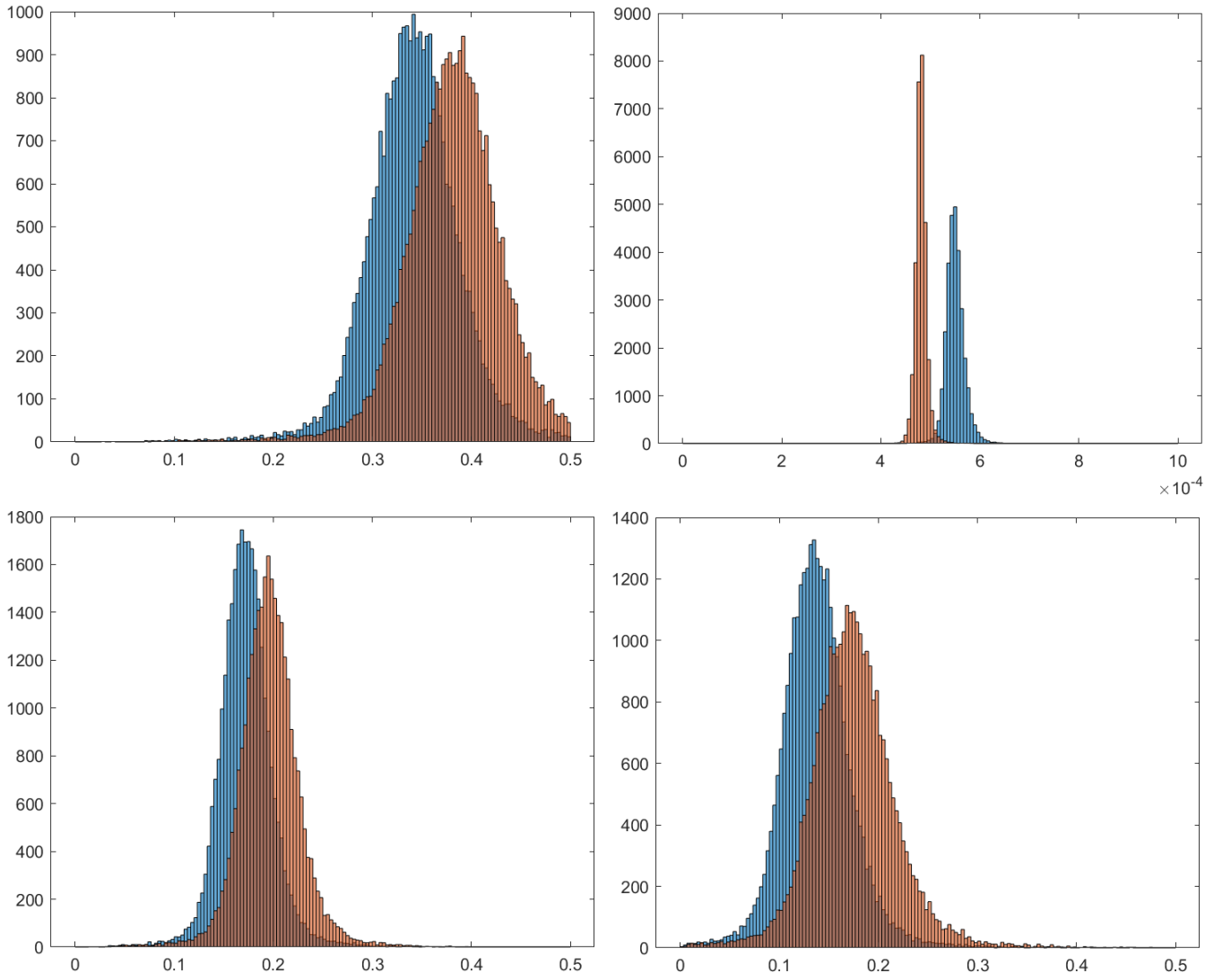

Figure 4.11: Histograms of FA, MD, RA, and VR from white matter. From top left to bottom right: FA, MD, RA, VR. Orange represents the free water correction data.

Selected ROI in Corpus Callosum

Corpus callosum has a very organized fiber structure, the anisotropy is therefore higher than the three major regions above. The anisotropy indices both before and after the correction, table 4.8 and figure 4.12, compared to the three major regions of grey matter, white matter and the composite brain.

Index	Mean	Std	P-value	Change(%)
FA	0.64	0.01		
FA-fw	0.70	0.01	$p < 0.01$	8.47
MD(10^{-4})	4.90	0.06		
MD-fw(10^{-4})	4.3	0.1	$p < 0.01$	-11.51
RA	0.36	0.01		
RA-fw	0.41	0.02	$p < 0.01$	13.02
1-VR(10^{-2})	43	1		
1-VR-fw(10^{-2})	51	2	$p < 0.01$	19.72

Table 4.8: Values of FA, MD, RA, and VR for corpus callosum.

Figures 4.13, 4.14, 4.15, and 4.16 are the visualizations of the various invariant indices for the corrected, non-corrected data, and the difference between them. The top left is non-corrected, the top right is corrected, while the bottom is the difference. Figure 4.17 is VR with a threshold applied($VR < 0.8$) to better visualize the difference between the corrected and non-corrected data.

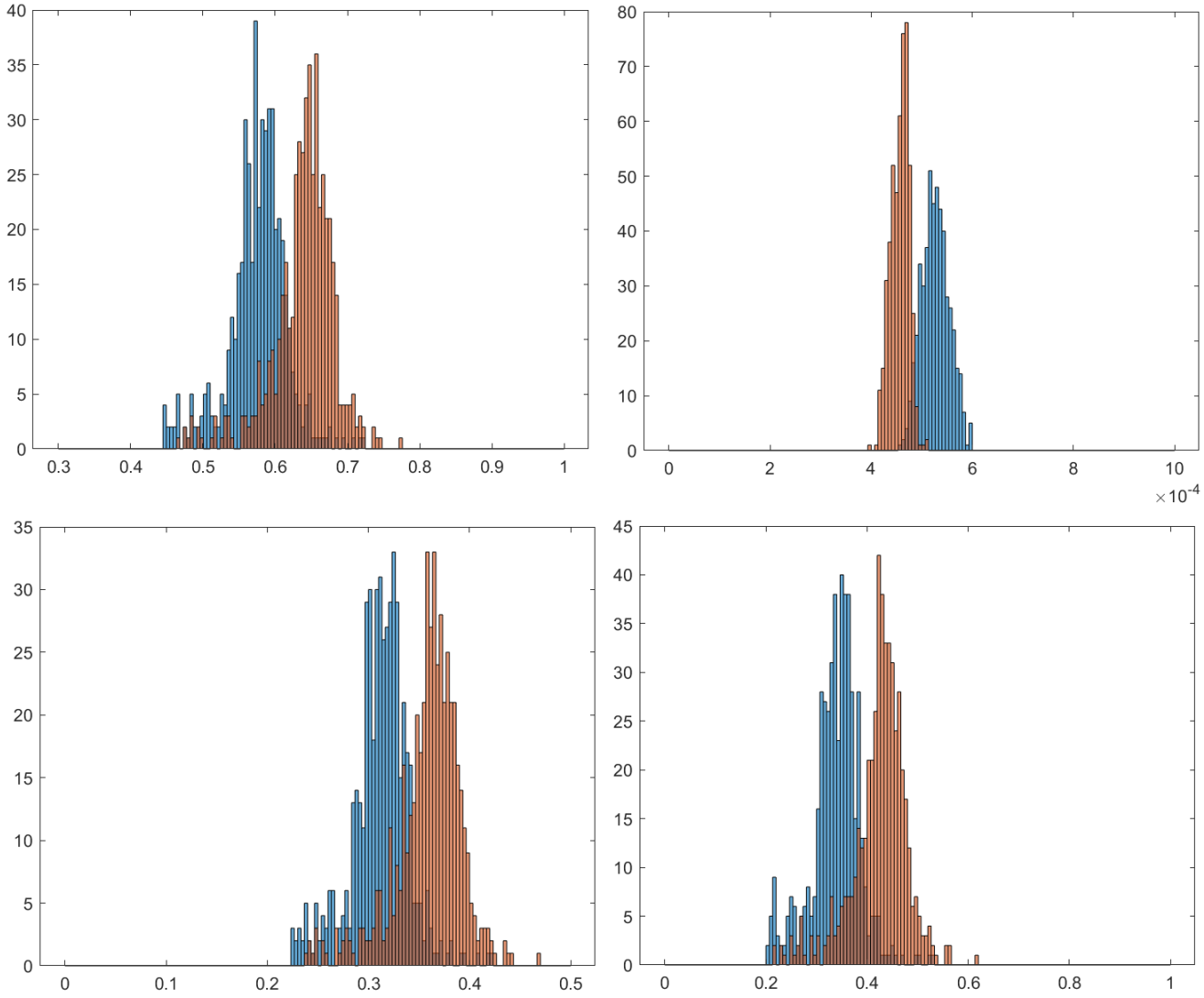

Figure 4.12: Histograms of FA, MD, RA, and VR from corpus callosum. From top left to bottom right: FA, MD, RA, VR. Orange represents the free water correction data.

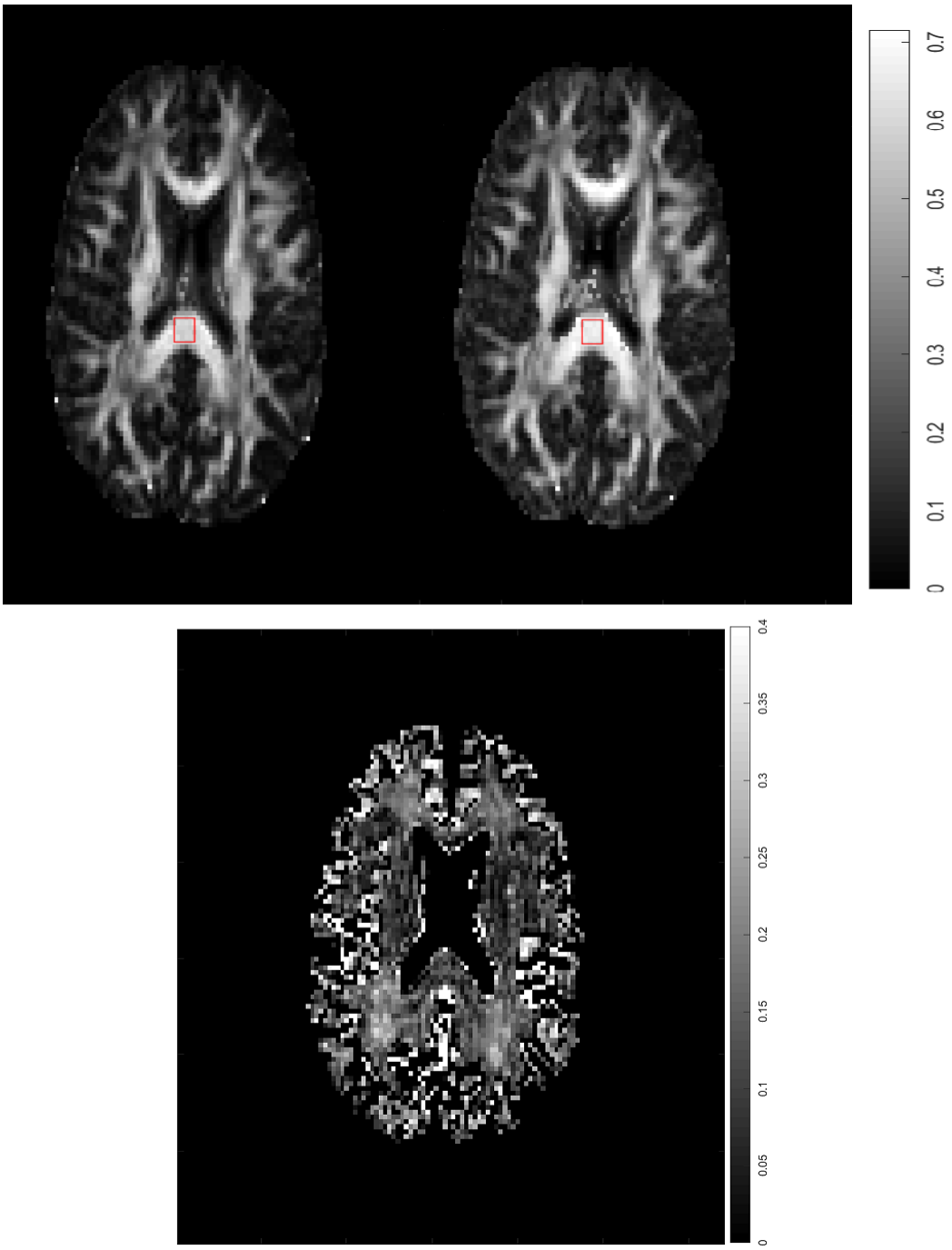

Figure 4.13: FA maps, top left visualization is non-corrected while the top right visualization has been corrected. Window level is the same in both pictures.

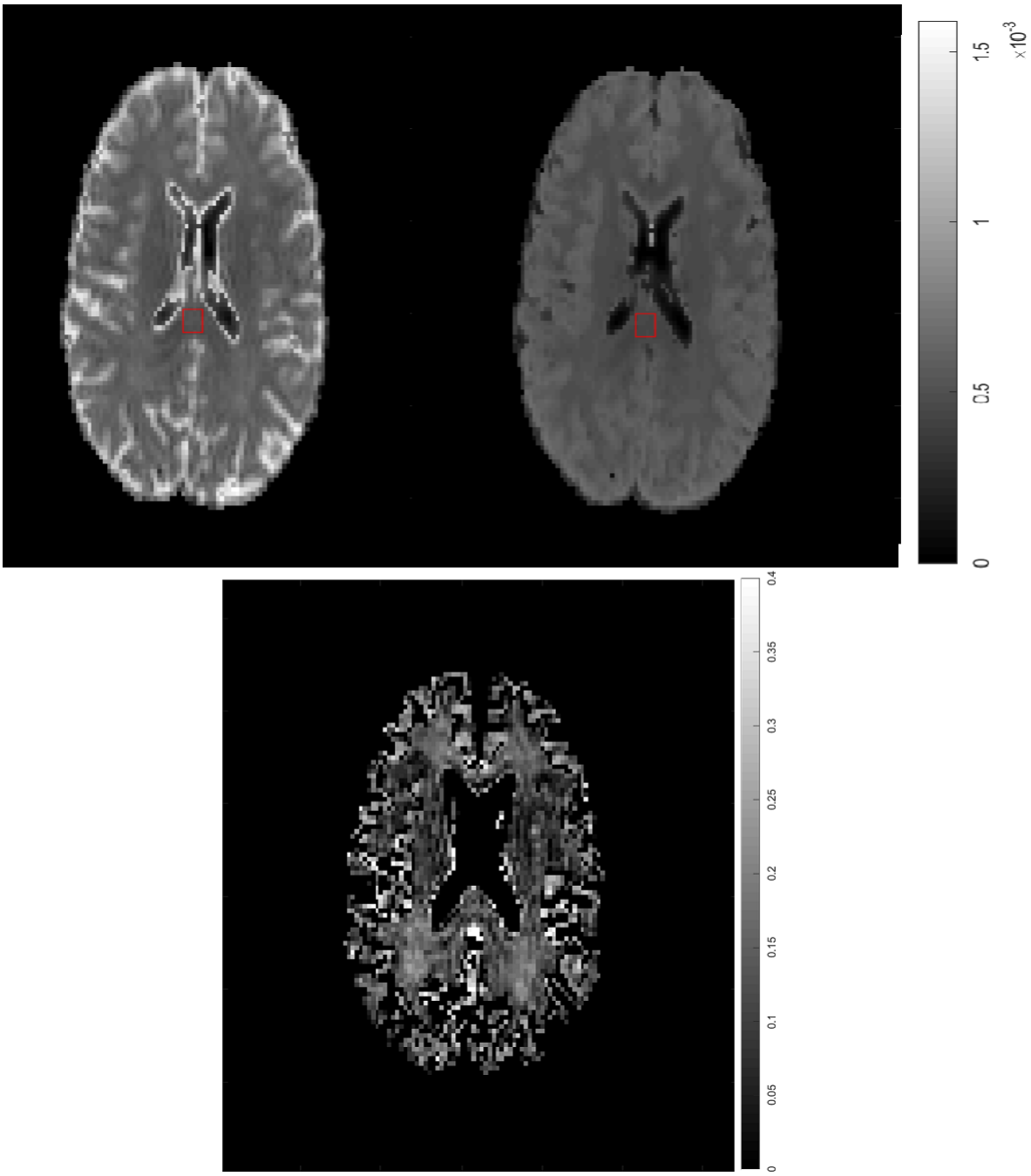

Figure 4.14: MD maps, top left visualization is non-corrected while the top right visualization has been corrected. Window level is the same in both pictures.

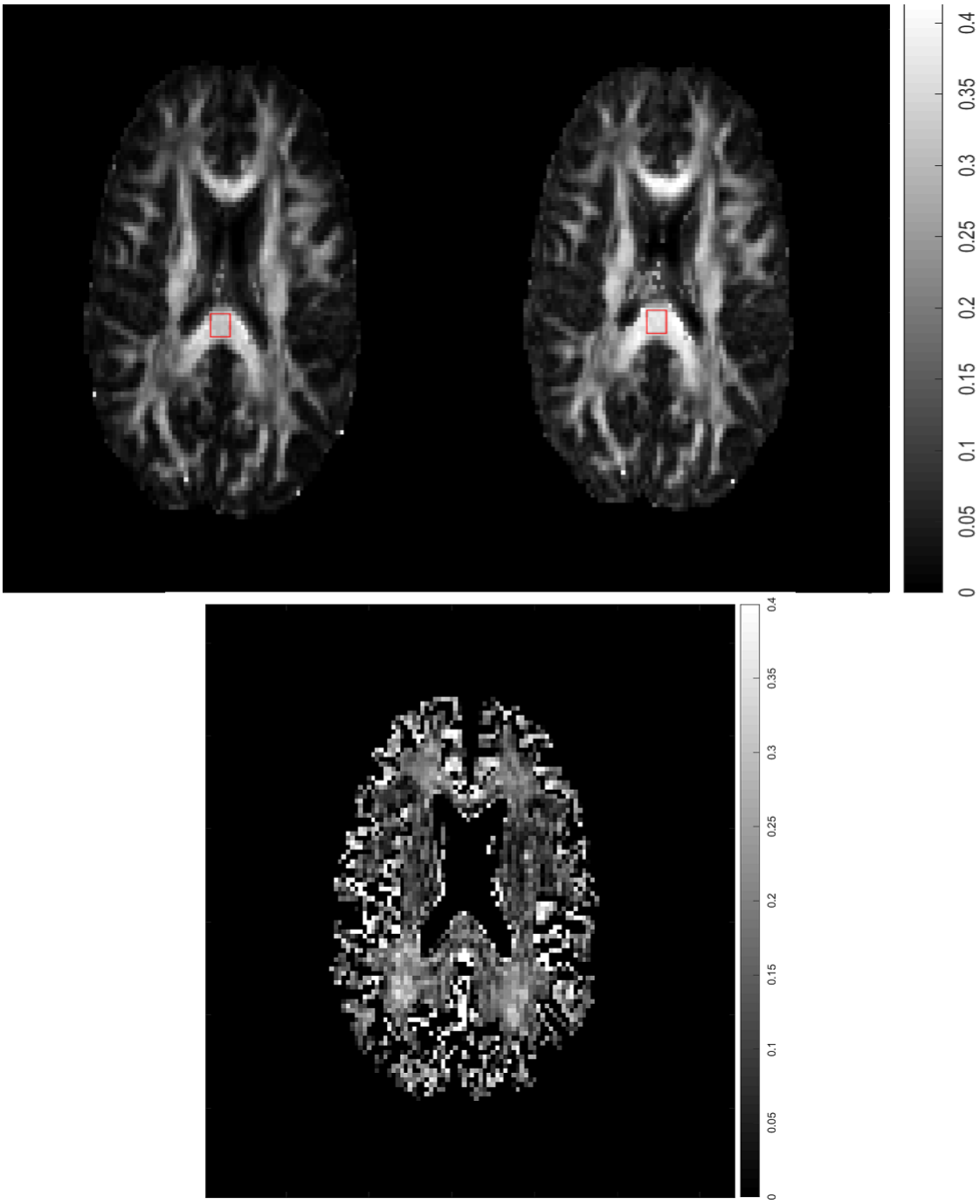

Figure 4.15: RA maps, top left visualization is non-corrected while the top right visualization has been corrected. Window level is the same in both pictures.

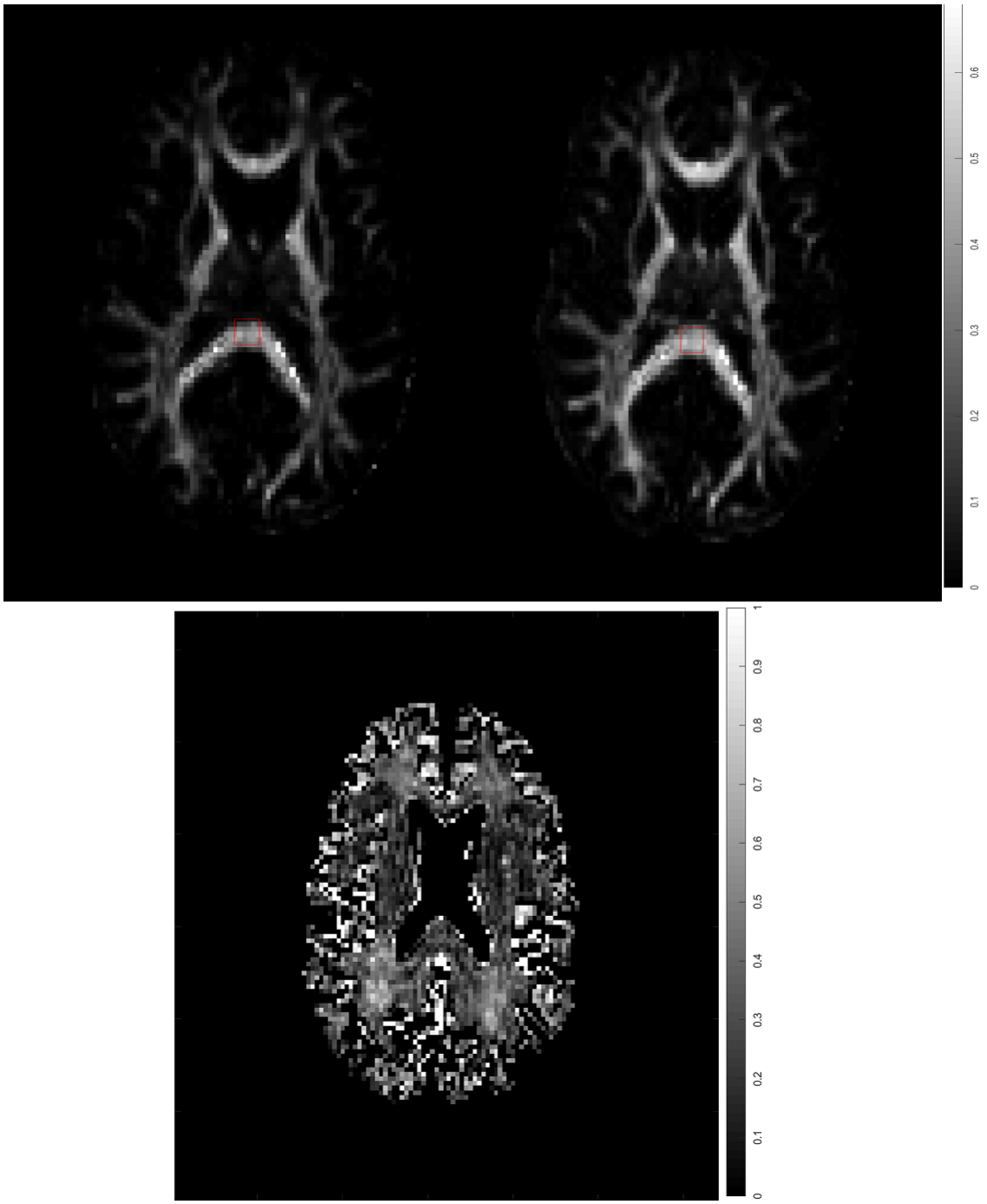

Figure 4.16: VR maps, top left visualization is non-corrected while the top right visualization has been corrected. Window level is the same in both top pictures, note that the window level in the difference picture is not the same as that used in FA, MD, and RA.

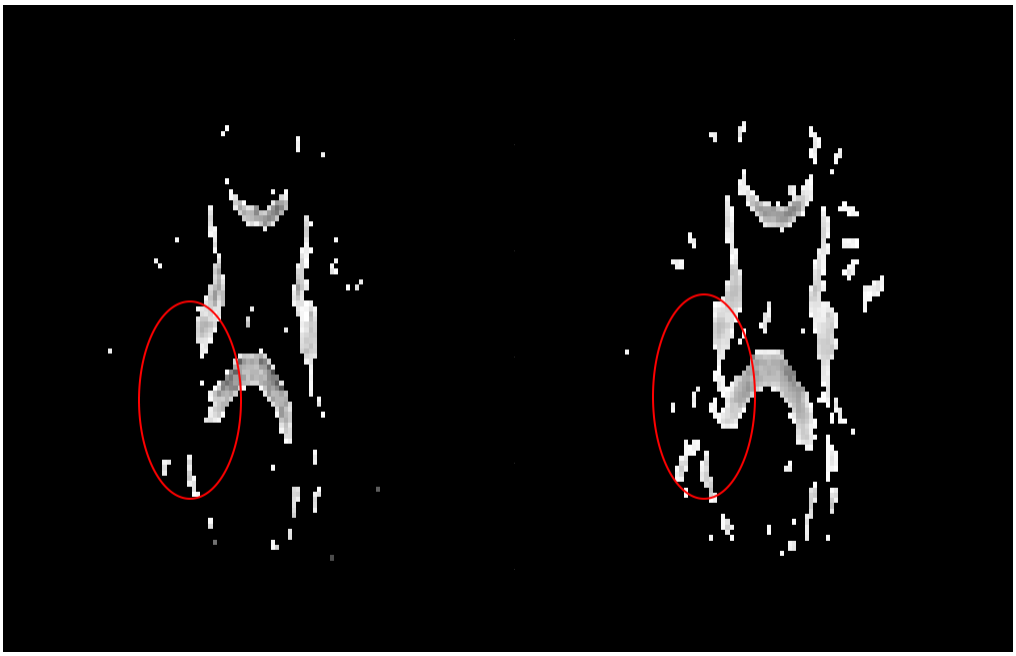

Figure 4.17: Non-corrected(top) and corrected(bottom) VR image with an applied threshold ($VR < 0.8$), showing a change in corpus callosum.

4.1.3 Other Rotationally Invariant Indices

Whole Brain Analysis

The invariant indices discussed in section 2.2.1 are important in regards to this project, as they contain information on the size relation of the three eigenvalues as shown in equations 2.47, 2.48, and 2.49. Due to how the free water correction affected λ_{123} causing $\lambda_1 >> \lambda_2, \lambda_3$, the indices showing the relationship between them are also changed significantly, table 4.9 and figure 4.18.

Index	Mean (10^{-2})	Std (10^{-2})	P-value	Change(%)
cl	8.7	0.7		
cl FW	10.0	0.7	$p < 0.01$	19.43
cp	9.0	0.6		
cp FW	10.7	0.5	$p < 0.01$	19.54
cs	80	2		
cs FW	76	2	$p < 0.01$	-5.84

Table 4.9: Invariant indices for the non-corrected and free water corrected data for the whole brain.

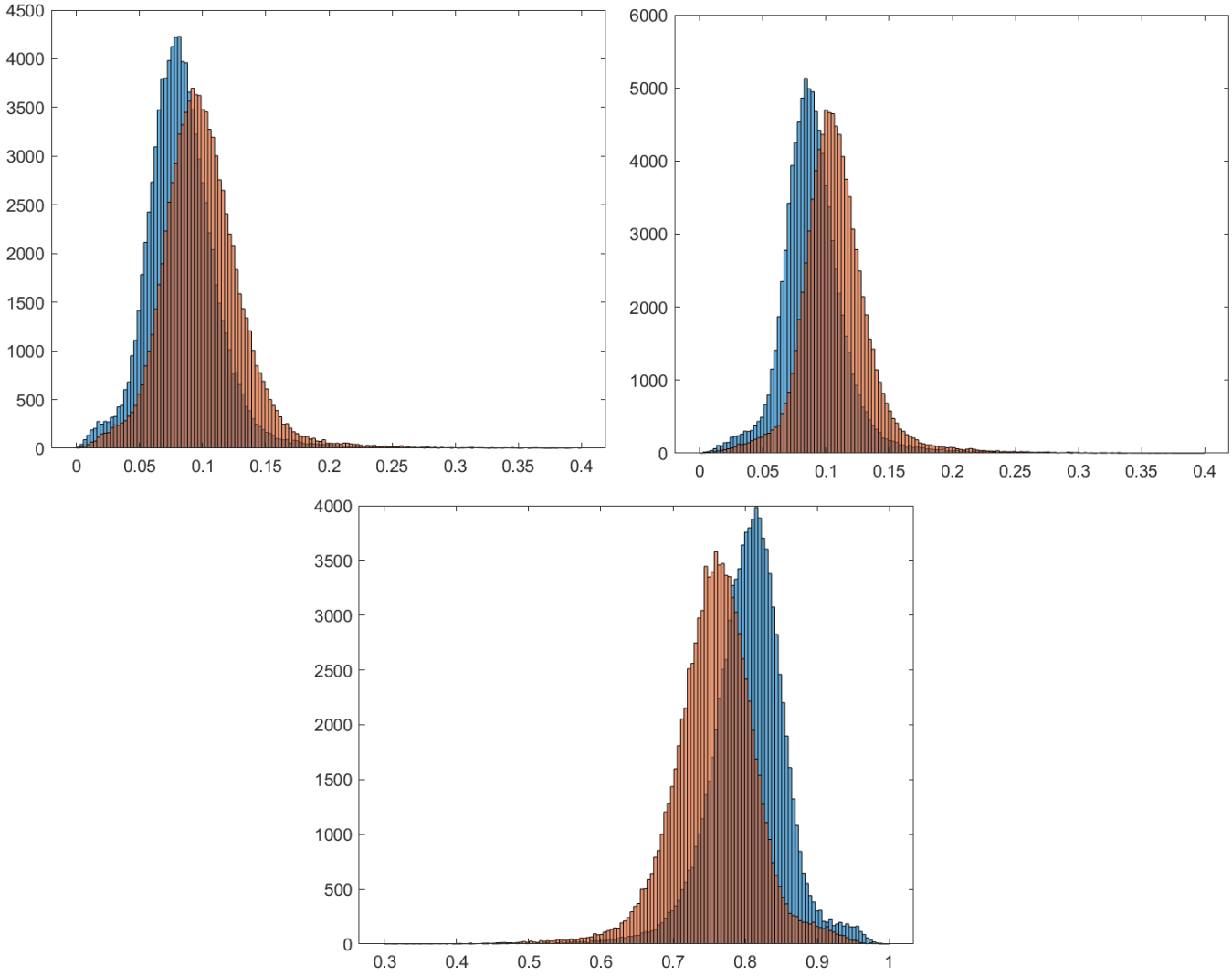

Figure 4.18: Histograms of cl, cp, and cs from the whole brain analysis. From top left to bottom right: cl, cp, cs. Orange represents the free water correction data.

Grey Matter Analysis

Grey matter is shown to be more isotropic, cl and cp are therefore lower in this region than in the rest of the brain, table 4.10, while cs is larger.

The invariant indices in the grey matter are generally lower when compared to the whole brain, table 4.9, the white matter, table 4.11, and corpus callosum, table 4.12. The change however, is greater in the grey matter than any of the other areas looked at.

Index	Mean (10^{-2})	Std (10^{-2})	P-value	Change(%)
cl	5	1		
cl FW	6.1	0.9	$p < 0.01$	22.45
cp	6.6	0.9		
cp FW	8.1	0.7	$p < 0.01$	23.98
cs	88	3		
cs FW	85	4	$p < 0.01$	-3.52

Table 4.10: Invariant indices for the segmented grey matter in the brain.

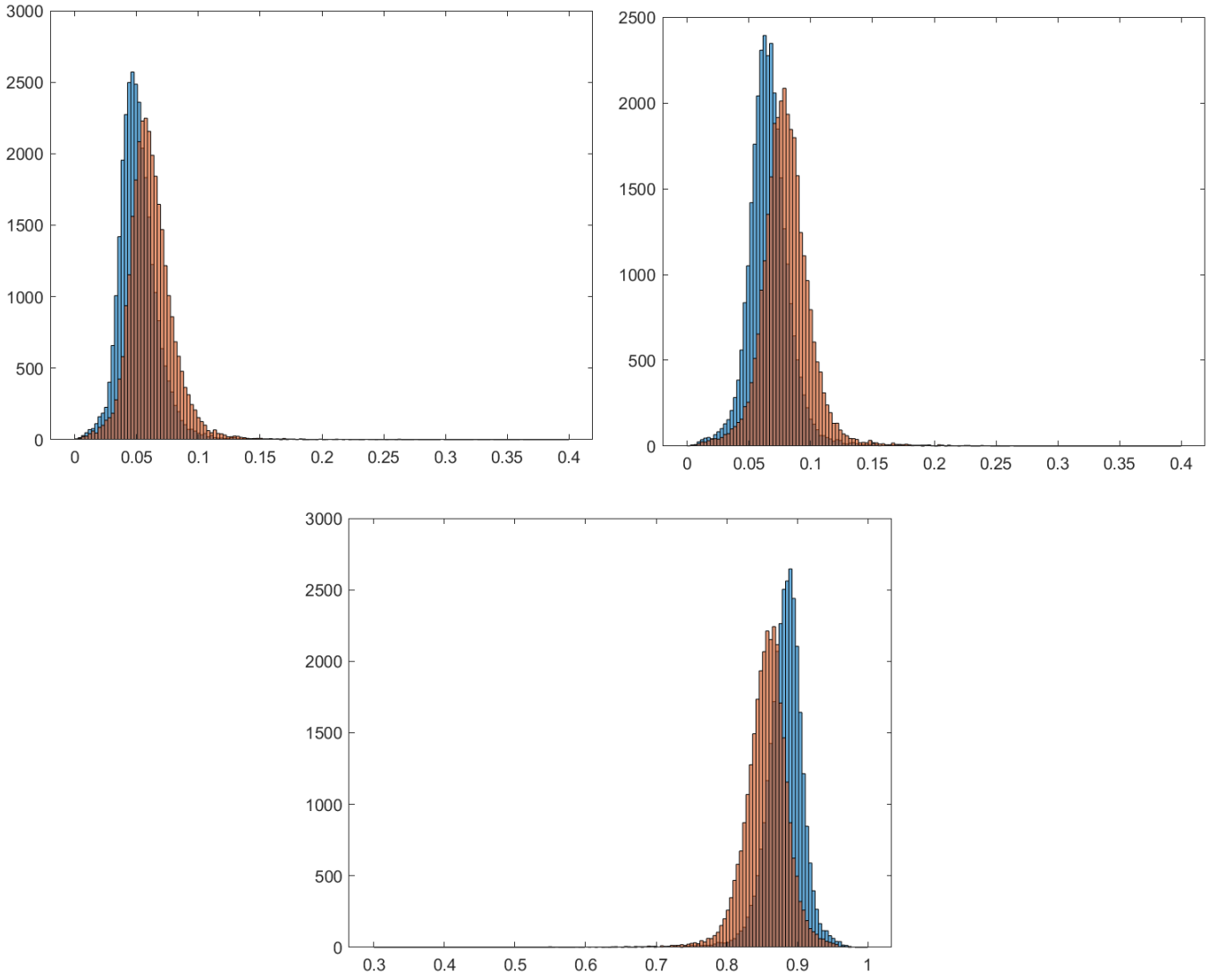

Figure 4.19: Histograms of cl, cp, and cs from grey matter. From top left to bottom right: cl, cp, cs. Orange represents the free water correction data.

White Matter Analysis

White matter is the major region with the highest degree of anisotropy, table 4.11 and figure 4.20, this is confirmed by the indices.

Index	Mean (10^{-2})	Std (10^{-2})	P-value	Change(%)
cl	15.9	0.7		
cl FW	18.2	0.7	$p < 0.01$	14.21
cp	14.4	0.4		
cp FW	16.3	0.4	$p < 0.01$	13.35
cs	70	1		
cs FW	65	1	$p < 0.01$	-6.16

Table 4.11: Invariant indices for the segmented white matter in the brain.

The white matter indices lies in between the whole brain analysis, table 4.9 and corpus callosum, table 4.12. The change is less than the grey matter, table 4.10.

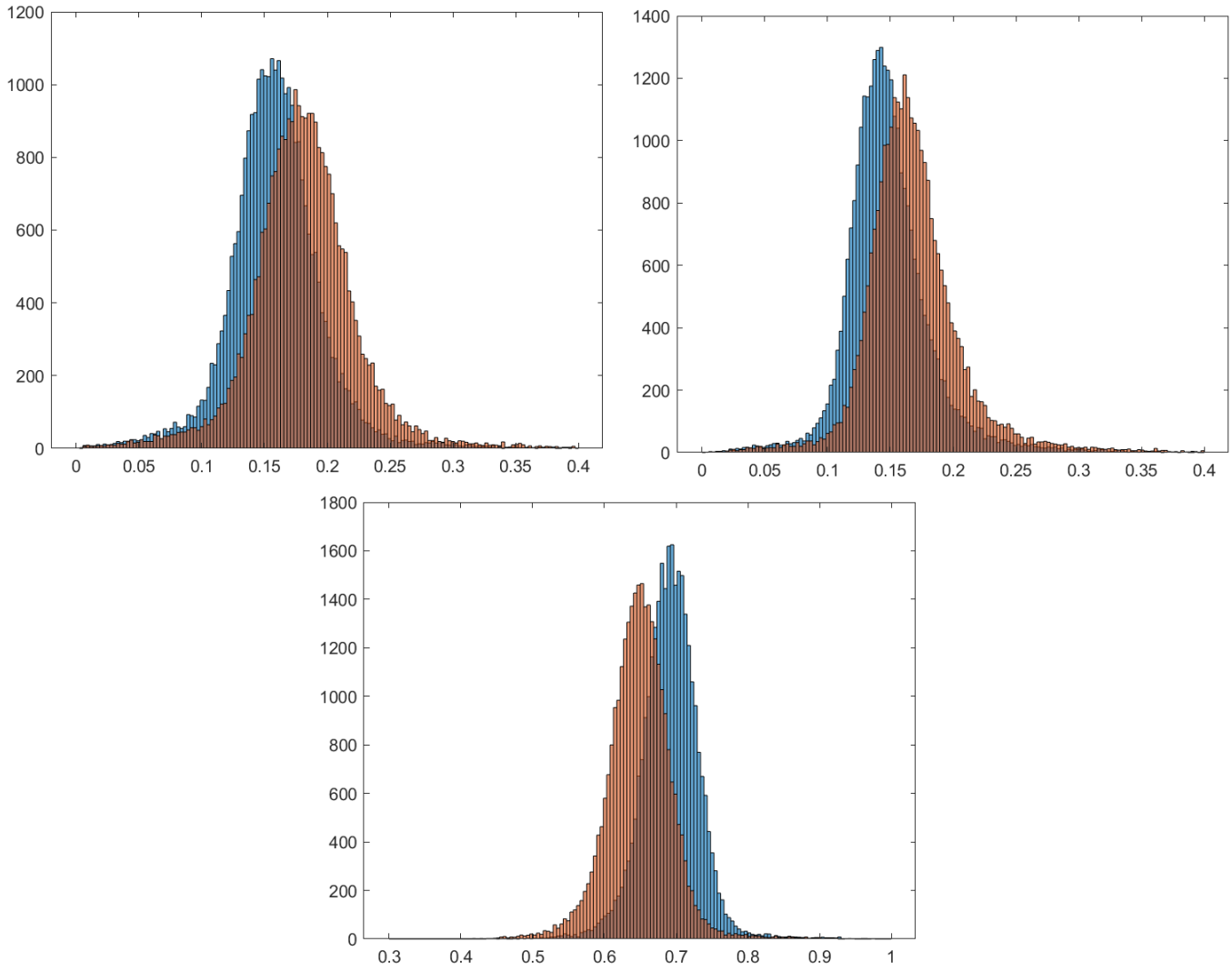

Figure 4.20: Histograms of cl, cp, and cs from white matter. From top left to bottom right: cl, cp, cs. Orange represents the free water correction data.

Selected ROI in Corpus Callosum

Corpus callosum, due to its fibers being in mainly the same direction, has the highest anisotropy indices, table 4.12 and figure 4.21.

Index	Mean(10^{-2})	Std(10^{-2})	P-value	Change(%)
cl	42	2		
cl FW	46	2	$p < 0.01$	10.81
cp	10	1		
cp FW	11	1	$p = 0.08$	9.82
cs	48.2	0.9		
cs FW	42	2	$p < 0.01$	-13.50

Table 4.12: Invariant indices for corpus callosum, note the increase in the cl and cp indices and subsequent decrease of the cs index.

This is the expected behavior of these invariant indices, the increase in linear anisotropy is due to the fact that λ_1 decreased much less than λ_2. The effect of the free water correction is exemplified in the spatial domain in figures 4.22, 4.24, and 4.25. Figure 4.23 shows the same slice as figure 4.22, where a more conservative window level is selected ($0.2 < cl < 0.6$) to better visualize the difference between the corrected and non-corrected images.

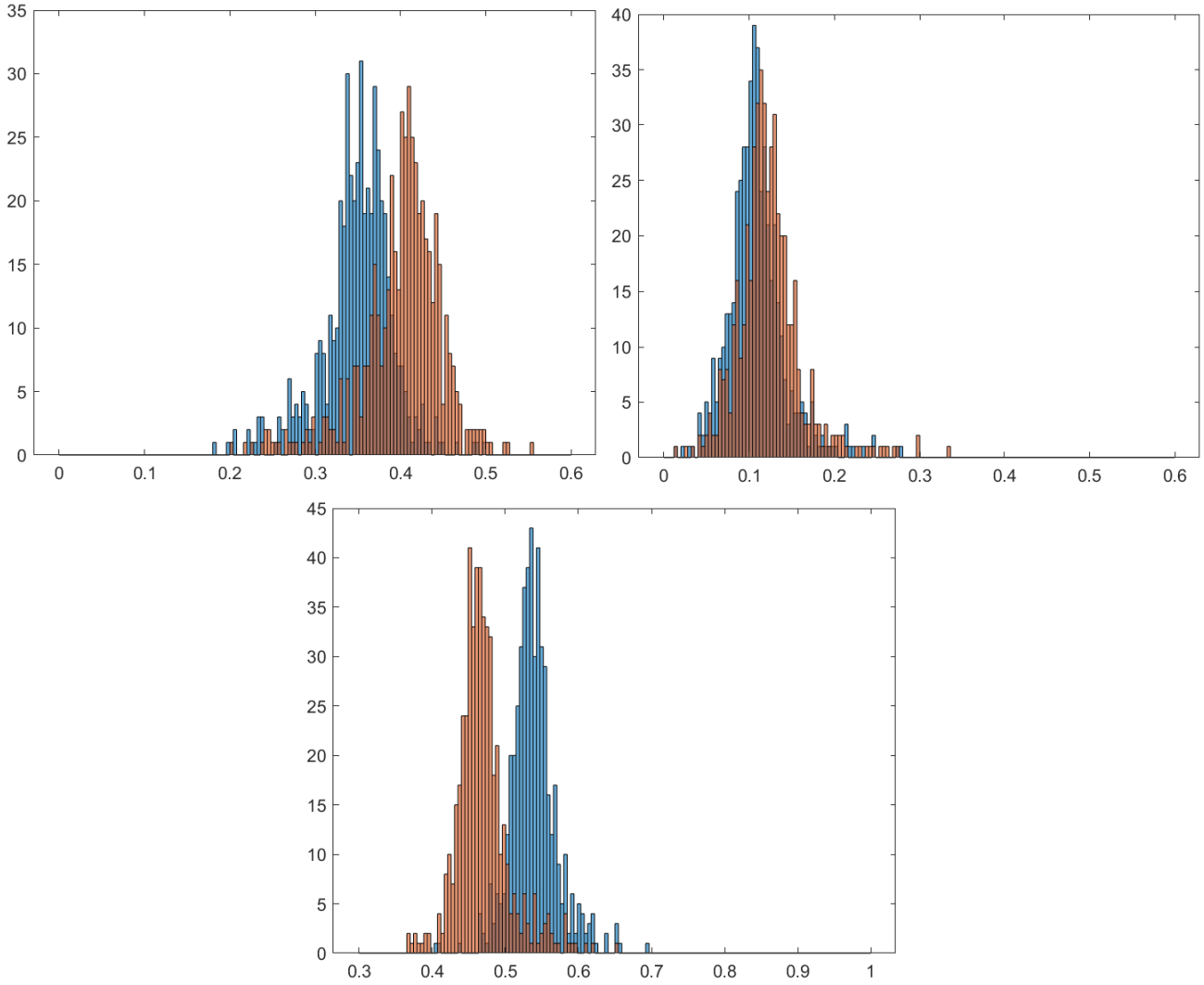

Figure 4.21: Histograms of cl, cp, and cs from corpus callosum. From top left to bottom right: cl, cp, cs. Orange represents the free water correction data.

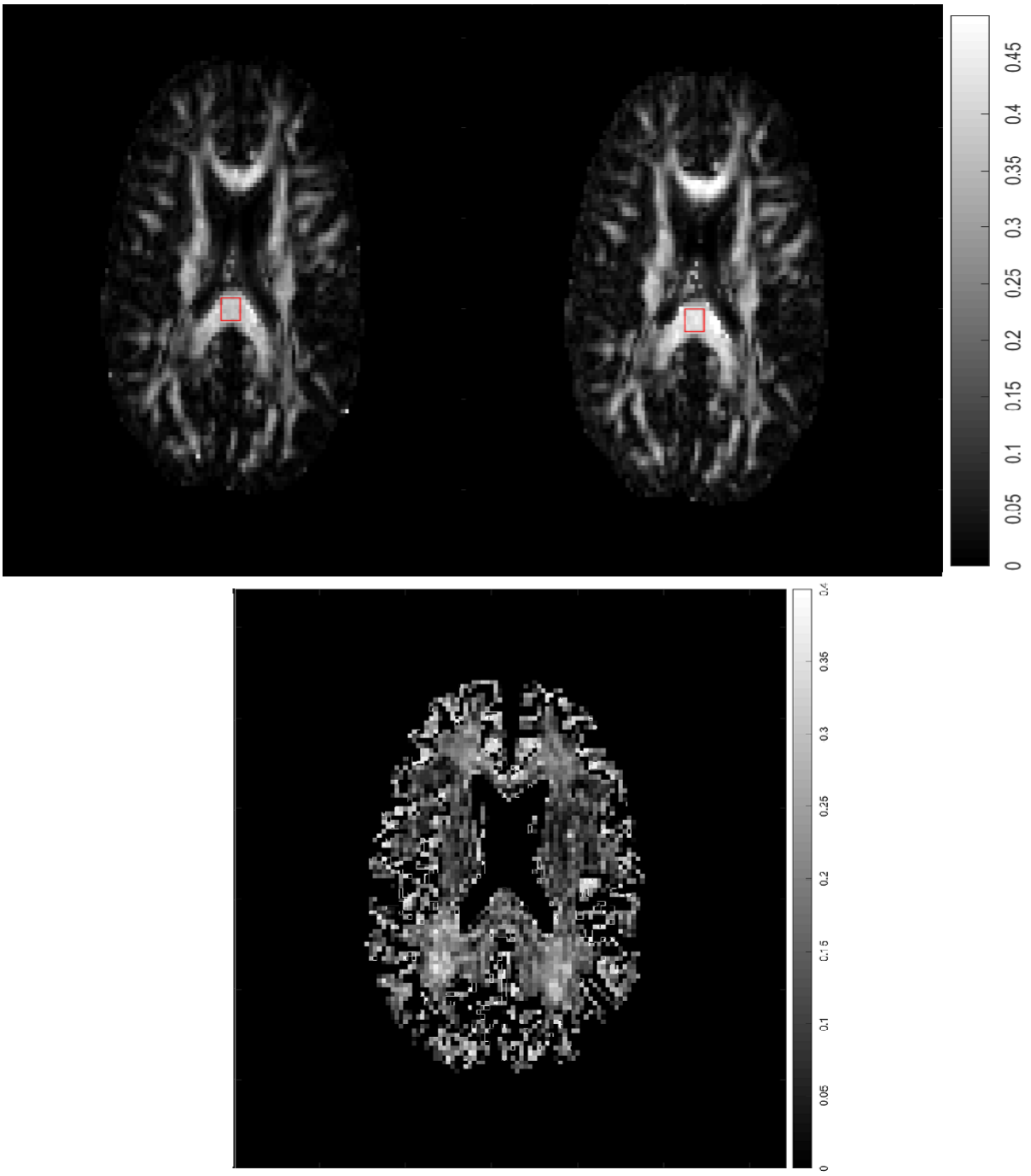

Figure 4.22: Cl, equation 2.47. Top left is non-corrected, top right is corrected, and the bottom is the difference.

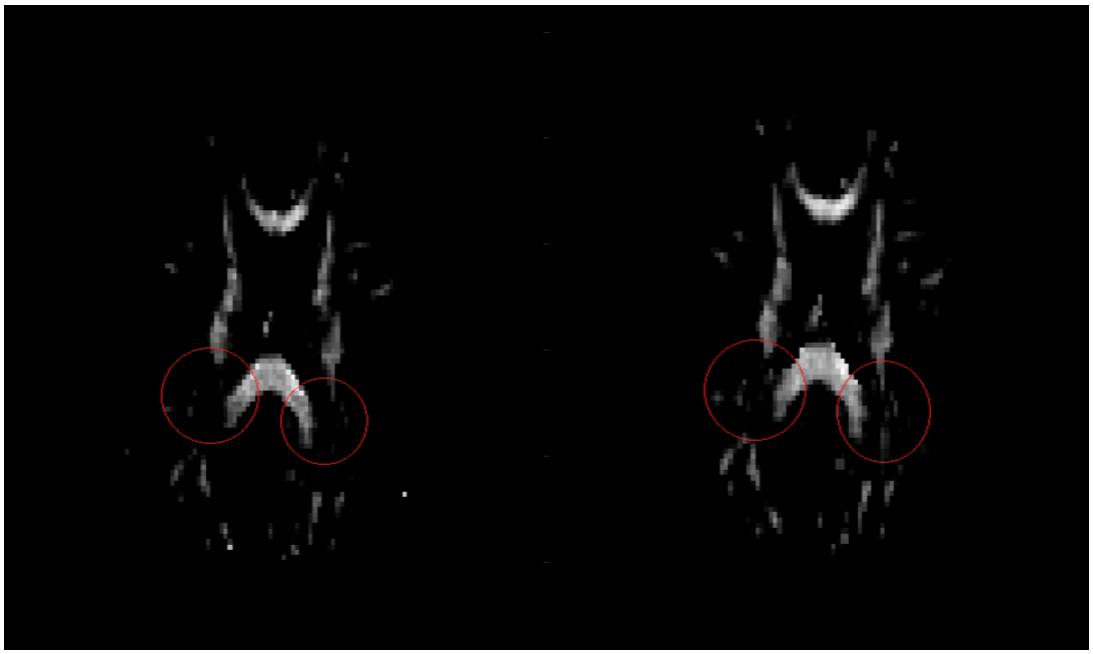

Figure 4.23: The linear anisotropy shown in figure 4.22 with the high ($cl > 0.6$) and low ($cl < 0.2$) values removed to better visualize the difference between the two, the red rings show the areas where the correction is the most visible. Left image is non-corrected and right is corrected.

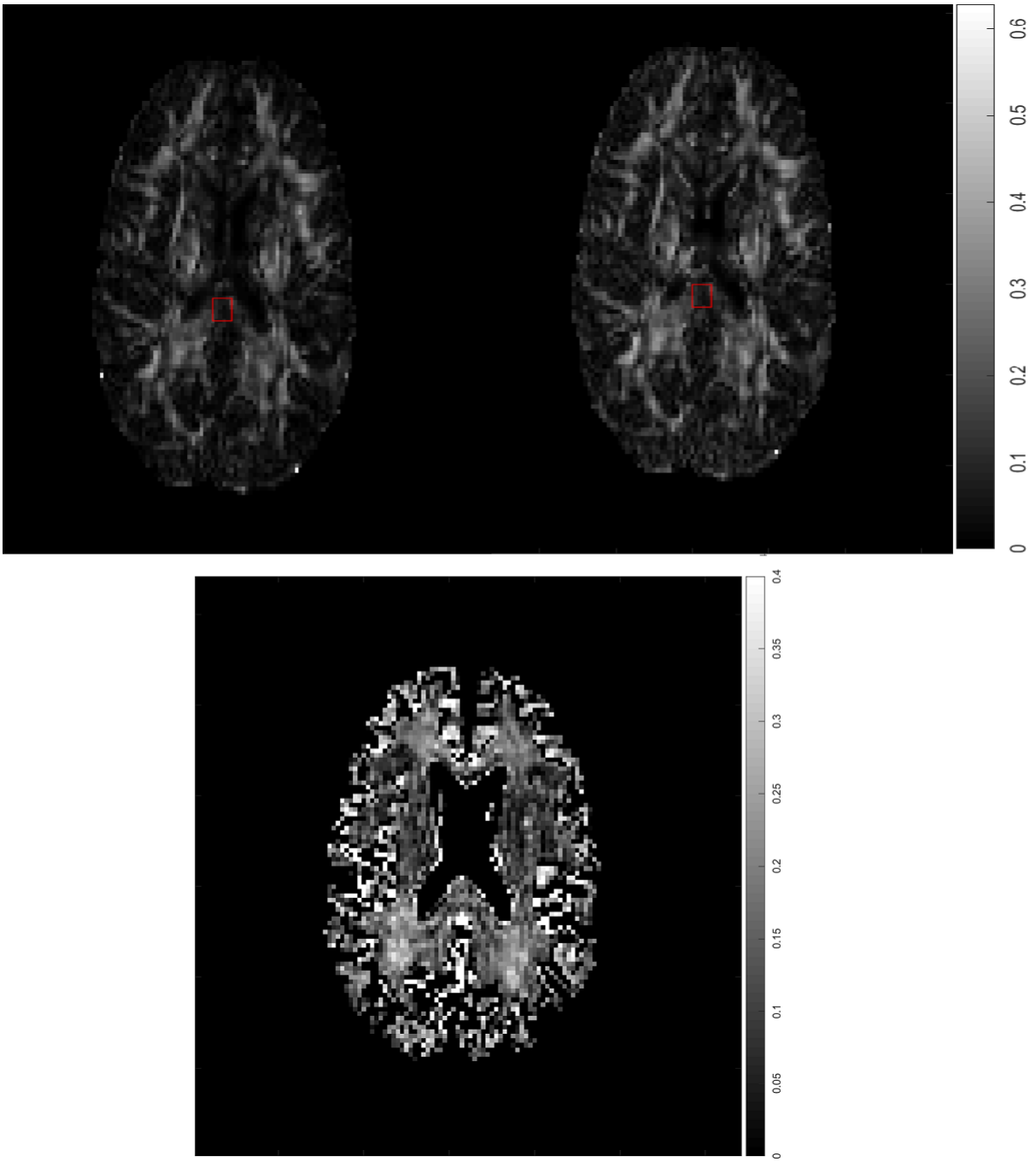

Figure 4.24: Cp, equation 2.48. Top left is non-corrected, top right is corrected, and the bottom is the difference.

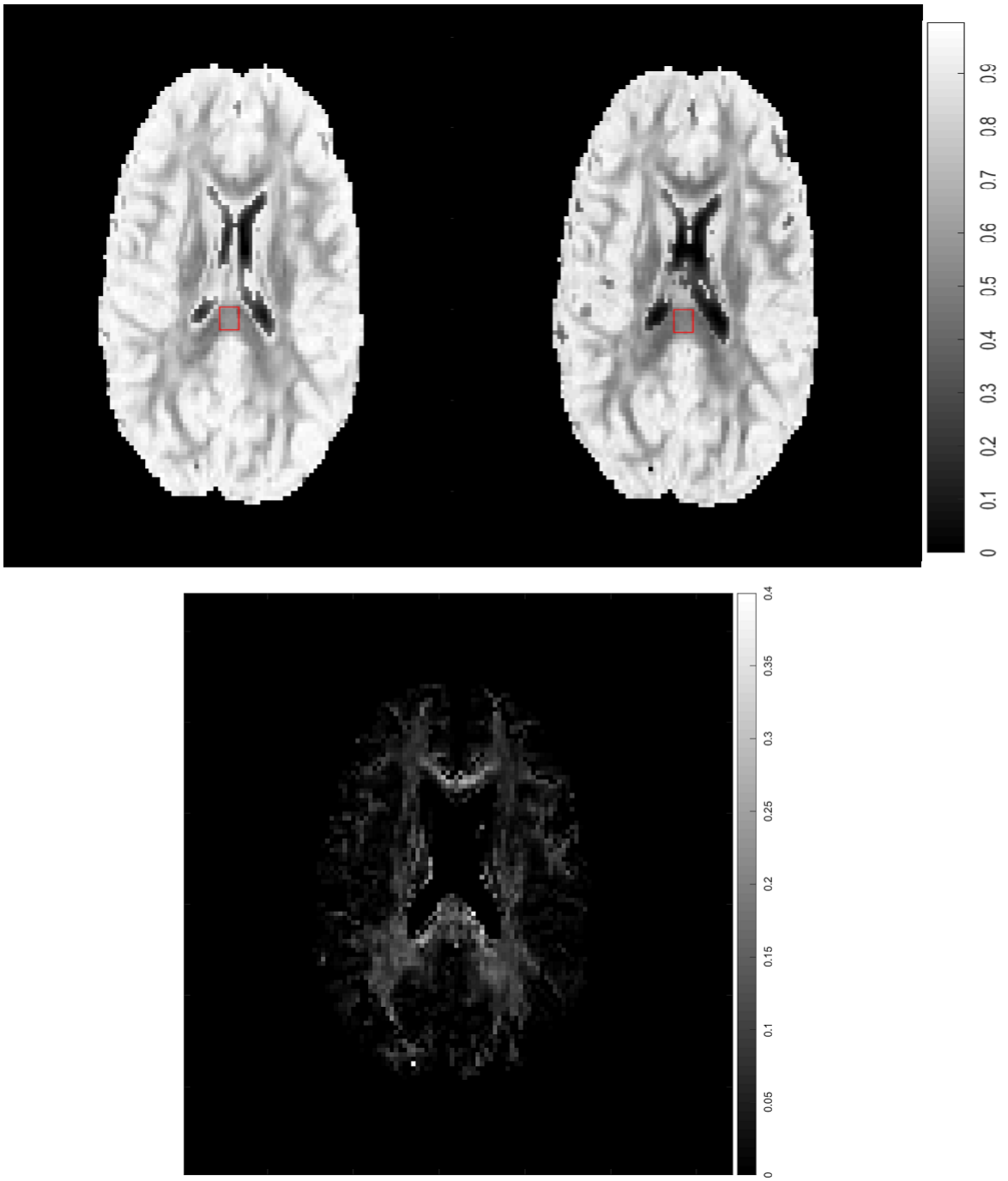

Figure 4.25: Cs, equation 2.49. Note that due to $cl + cp + cs = 1$ the intensity in the visualization is inverted, areas with high anisotropy are darker. Top left image is non-corrected,the top right is corrected, and the bottom image is the difference.

4.1.4 Fiber Tractography

Selected ROI in Corpus Callosum

The fiber tractography results follows the brute-force technique laid out in section 2.2.1. The analysis was done on one random brain. The results were gathered around the corpus callosum area, using the fiber tractography algorithm used in NordicIce (Nordic NeuroLabs inc, Bergen, Norway), as can be seen in table 4.13. The reasons for this are discussed in the discussion chapter.

Parameters	Fiber FW	FA FW	Std FW	Fiber	FA	Std
40°, $FA > 0.300$	4200	0.6	0.1	2562	0.5	0.1
40°, $FA > 0.200$	4608	0.6	0.2	3357	0.5	0.1
40°, $FA > 0.100$	6194	0.5	0.2	5469	0.4	0.2
50°, $FA > 0.300$	4018	0.6	0.1	2483	0.5	0.1
50°, $FA > 0.200$	5042	0.5	0.2	3356	0.5	0.1
50°, $FA > 0.100$	5962	0.5	0.2	5309	0.4	0.2
60°, $FA > 0.300$	3953	0.5	0.2	2480	0.5	0.1
60°, $FA > 0.200$	4912	0.5	0.2	3386	0.5	0.1
60°, $FA > 0.100$	5670	0.5	0.2	4914	0.4	0.2

Table 4.13: Fiber tractography data from NordicIce, the parameters denote the cutoff angle and the FA threshold as discussed in section 2.2.1.

Figures 4.26 and 4.27 shows the different fiber tractographies. These are the ROI used for the analysis, they were made very thin in the middle of corpus callosum. The top images belonging to figure 4.26 shows the non-corrected fiber tractography. The bottom images 4.27 are the corrected fiber tractographies. The expertise to comment on the anatomical accuracy of these two images is not present in this thesis. The parameters used for the visualizations are: $FA < 0.300$, termination angle=60°, and minimum fiber length= 5mm.

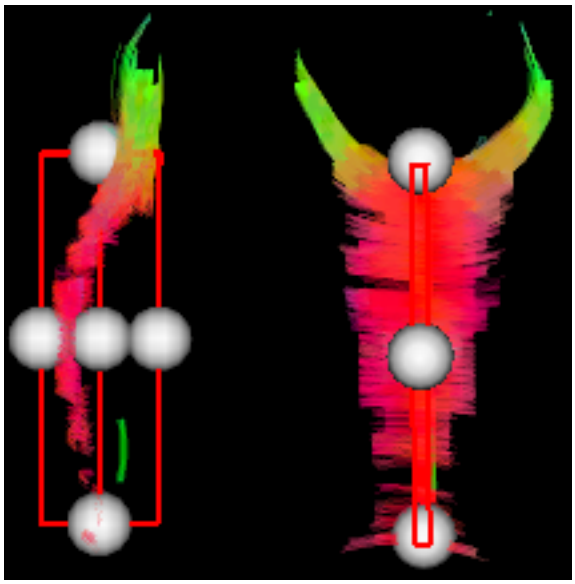

Figure 4.26: The Fiber tractography with ROI shown as the red box for the non-corrected data. The left image is shot sagitally, while the right image is shot axially. The ROI boxes are the same.

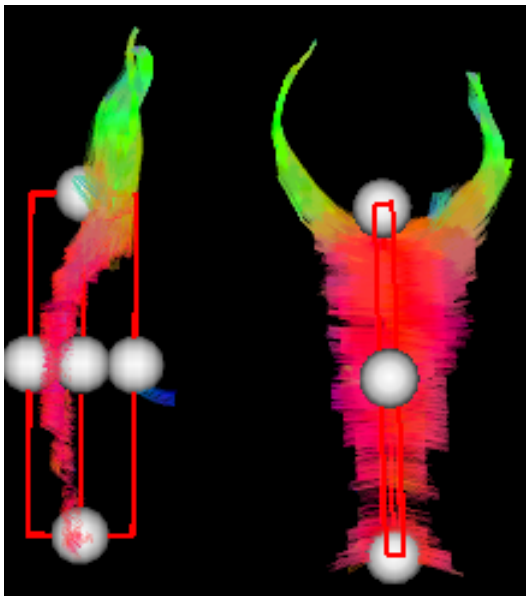

Figure 4.27: The fiber tractography with ROI shown as the red boxes for the corrected data. The left image is shot sagitally, while the right image is shot axially. The ROI boxes are the same, and almost identical to the non-corrected ROI.

4.2 Participants with MS

4.2.1 Eigenvalues

Whole Brain Analysis

As seen in the 20 healthy volunteers in section 4.1, the eigenvalues are reduced significantly when the free water is removed. Removing a sphere of free water will affect λ_{123} significantly, table 4.14, in the participants with MS, similar to how λ_{123} from the healthy volunteers were affected.

Index	Mean (10^{-4})	Std (10^{-4})	P-value	Change(%)
λ_1	7.9	0.3		
$\lambda_1 FW$	6.1	0.2	$p < 0.01$	-23.75
λ_2	6.5	0.3		
$\lambda_2 FW$	4.7	0.1	$p < 0.01$	-28.58
λ_3	5.8	0.3		
$\lambda_3 FW$	3.91	0.08	$p < 0.01$	-32.24

Table 4.14: The eigenvalues from 20 participants with MS, FW denotes free water corrected values, showing a larger relative decrease in λ_{23} compared to λ_1.

The free water estimation reduced the spread of the eigenvalues, but not to the same extent as in the healthy volunteers. Figure 4.28 shows the histogram of table 4.14.

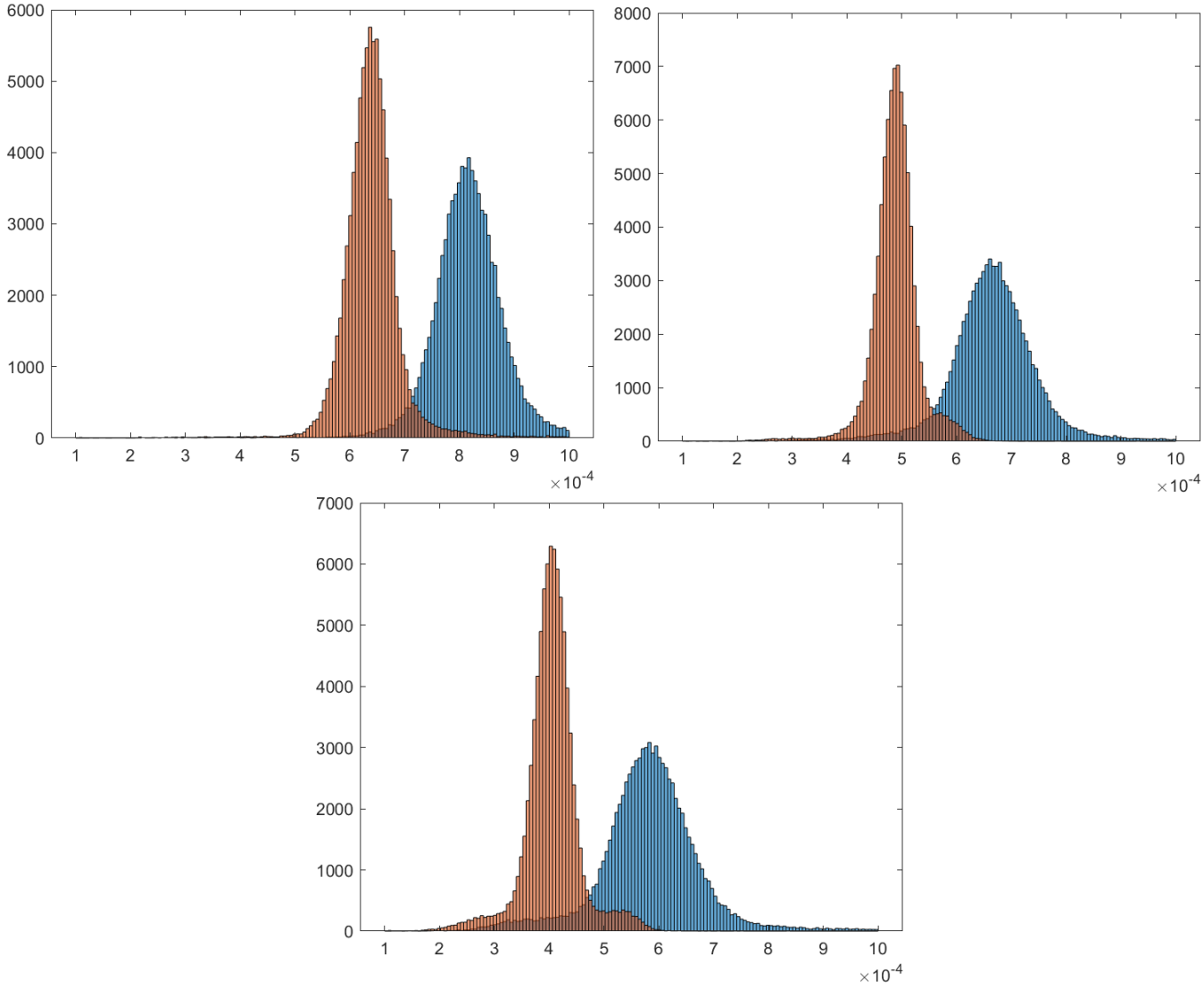

Figure 4.28: The three eigenvalues from top left: λ_1, λ_2 and λ_3 (bottom). Orange represents the free water correction data.

Grey Matter Analysis

Segmenting out the areas that are most probably grey matter, $> 80\%$ probability, the same analysis as in section 4.1 is repeated for the participants with MS. Because grey matter is highly isotropic, the free water correction should remove a large sphere from the vector, this is reflected in the values of λ_{123}, table 4.15.

There is a significant decrease in λ_{123}. Figure 4.29 shows the histograms of table 4.15.

Index	Mean(10^{-4})	Std(10^{-4})	P-value	Change(%)
λ_1	8.0	0.1		
$\lambda_1 FW$	6.44	0.07	$p < 0.01$	-19.88
λ_2	7.2	0.2		
$\lambda_2 FW$	5.57	0.05	$p < 0.01$	-22.34
λ_3	6.6	0.1		
$\lambda_3 FW$	4.95	0.03	$p < 0.01$	-24.52

Table 4.15: λ_{123} for the segmented grey matter part of the participants with MS.

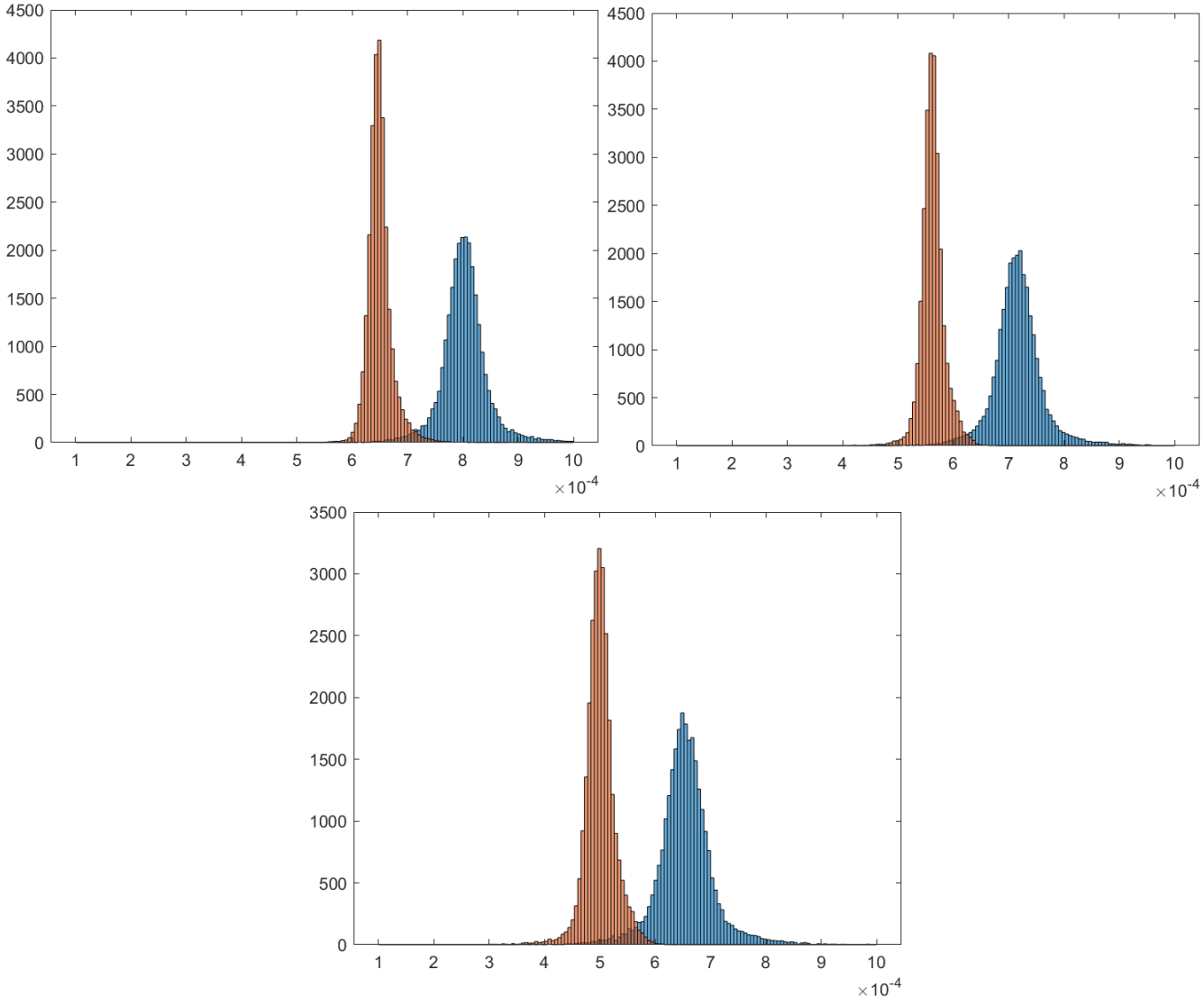

Figure 4.29: The three eigenvalues from the grey matter segmentation, from the top left: λ_1, λ_2 and λ_3 (bottom). Orange represents the free water correction data.

White Matter Analysis

Segmenting out the white matter part of the brain with the same threshold value as the grey matter segmentation, $> 80\%$ probability of white matter. There is a smaller reduction in λ_{123} in white matter, table4.16, when compared to the the grey matter, table 4.15, and the whole brain analysis, table 4.14.

Index	Mean (10^{-4})	Std(10^{-4})	P-value	Change (%)
λ_1	7.60	0.06		
$\lambda_1 FW$	6.93	0.05	$p < 0.01$	-8.39
λ_2	5.08	0.06		
$\lambda_2 FW$	4.39	0.04	$p < 0.01$	-13.46
λ_3	3.89	0.05		
$\lambda_3 FW$	3.21	0.03	$p < 0.01$	-17.64

Table 4.16: λ_{123} for the whole brain of participants with MS in the segmented white matter.

As seen in the healthy volunteers, the white matter λ_1 is larger than λ_{23} when compared to the grey matter, or whole brain analysis, the spread is also lower when comparing this white matter analysis to the grey matter and whole brain analysis. Figure 4.30 shows the histograms of table 4.16.

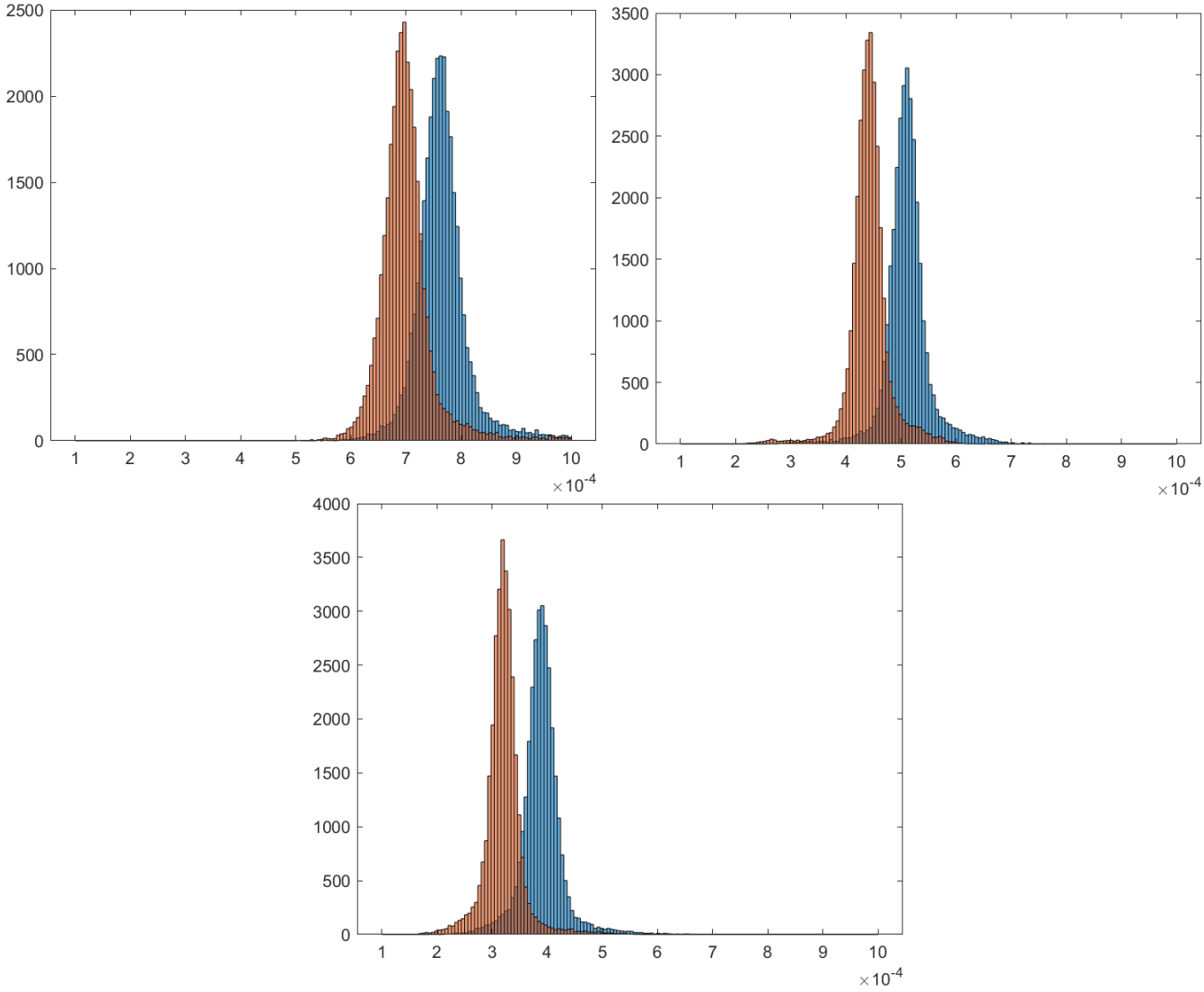

Figure 4.30: The three eigenvalues from the white matter segmentation for the participants with MS, from the top left: λ_1, λ_2 and λ_3 (bottom). Orange represents the free water correction data.

Selected ROI in Corpus Callosum

Corpus callosum in the participants with MS, table 4.17, has the same $\lambda_1 >> \lambda_2, \lambda_3$ hierarchy as the healthy volunteers. They are also affected in the same way, less than white matter, grey matter and whole brain analysis.

Index	Mean (10^{-4})	Std (10^{-4})	P-value	Change(%)
λ_1	9.0	0.2		
$\lambda_1 FW$	8.5	0.2	$p < 0.01$	-5.88
λ_2	3.2	0.1		
$\lambda_2 FW$	2.7	0.1	$p < 0.01$	-17.00
λ_3	2.5	0.1		
$\lambda_3 FW$	2.0	0.1	$p < 0.01$	-21.51

Table 4.17: The eigenvalues (λ_{123}) in a small area in Corpus Callosum, very close to the ventricles, in the participants with MS.

Figure 4.31 shows the histogram of the eigenvalues in corpus callosum and figure 4.32 shows the ellipsoids created by the eigenvalues in corpus callosum. The axes has been kept the same to show the decrease in all eigenvalues in addition to the more pronounced λ_1. Figures 4.33, 4.34, and 4.35, are visualizations of λ_{123}, in all figures, the red box denotes the area used for the corpus callosum analysis, the top image is the non-corrected, and the bottom has been corrected for free water.

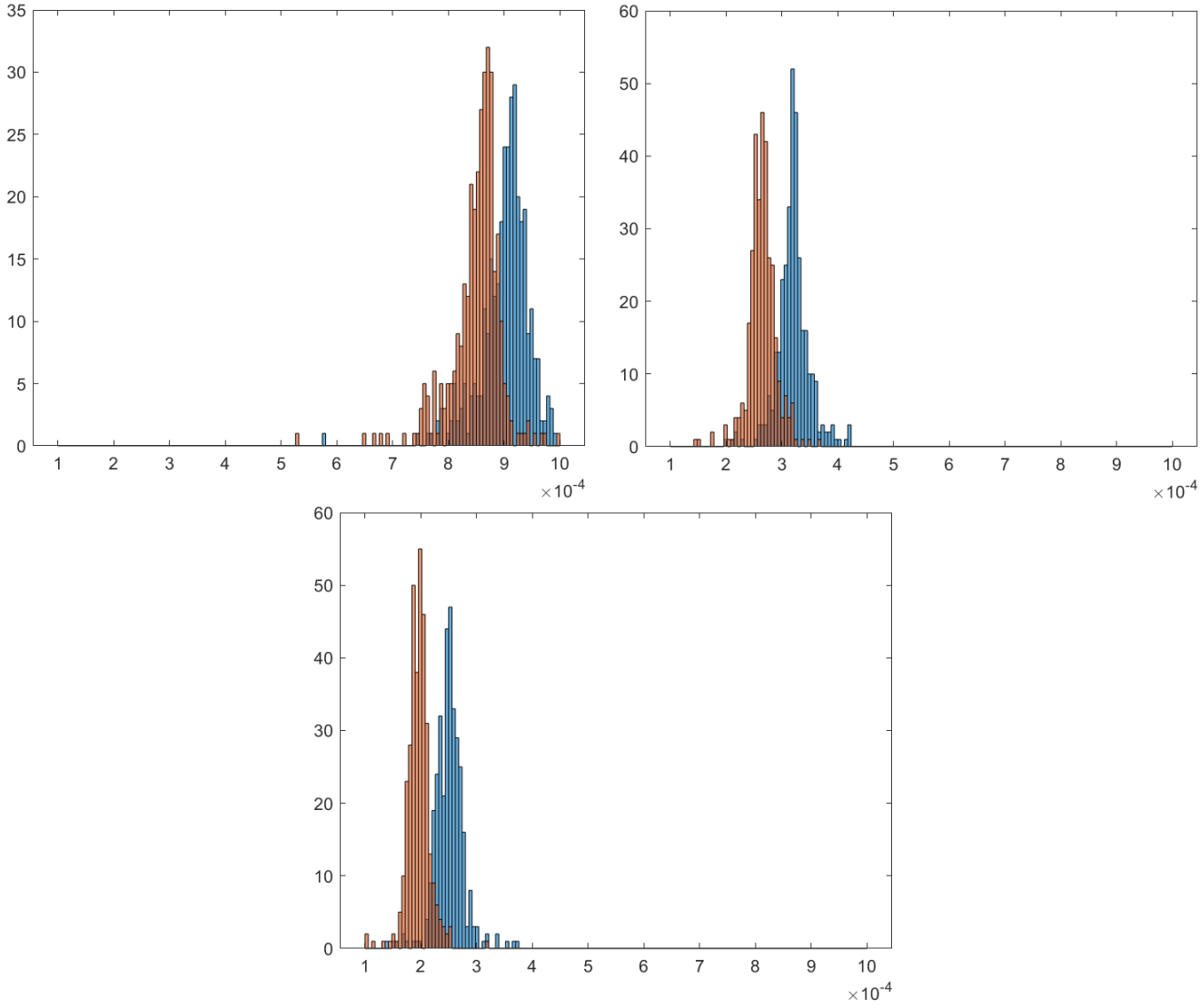

Figure 4.31: Histograms of λ_{123} for corpus callosum in the participants with MS. From top left to bottom: $\lambda_1\lambda_2\lambda_3$. Orange represents the free water correction data.

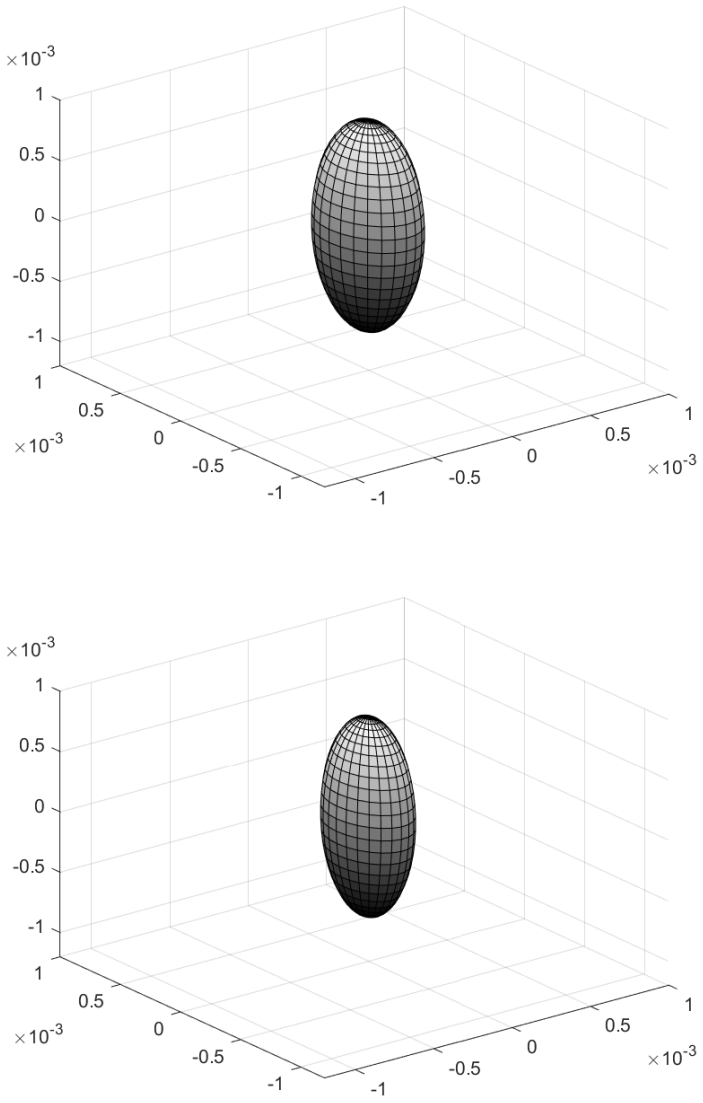

Figure 4.32: Ellipsoids constructed using λ_{123}, from corpus callosum, in the participants with MS, found in table 4.17, the non-corrected ellipsoid is on top and the corrected is on the bottom. Axes are set to the same scale for a better comparison.

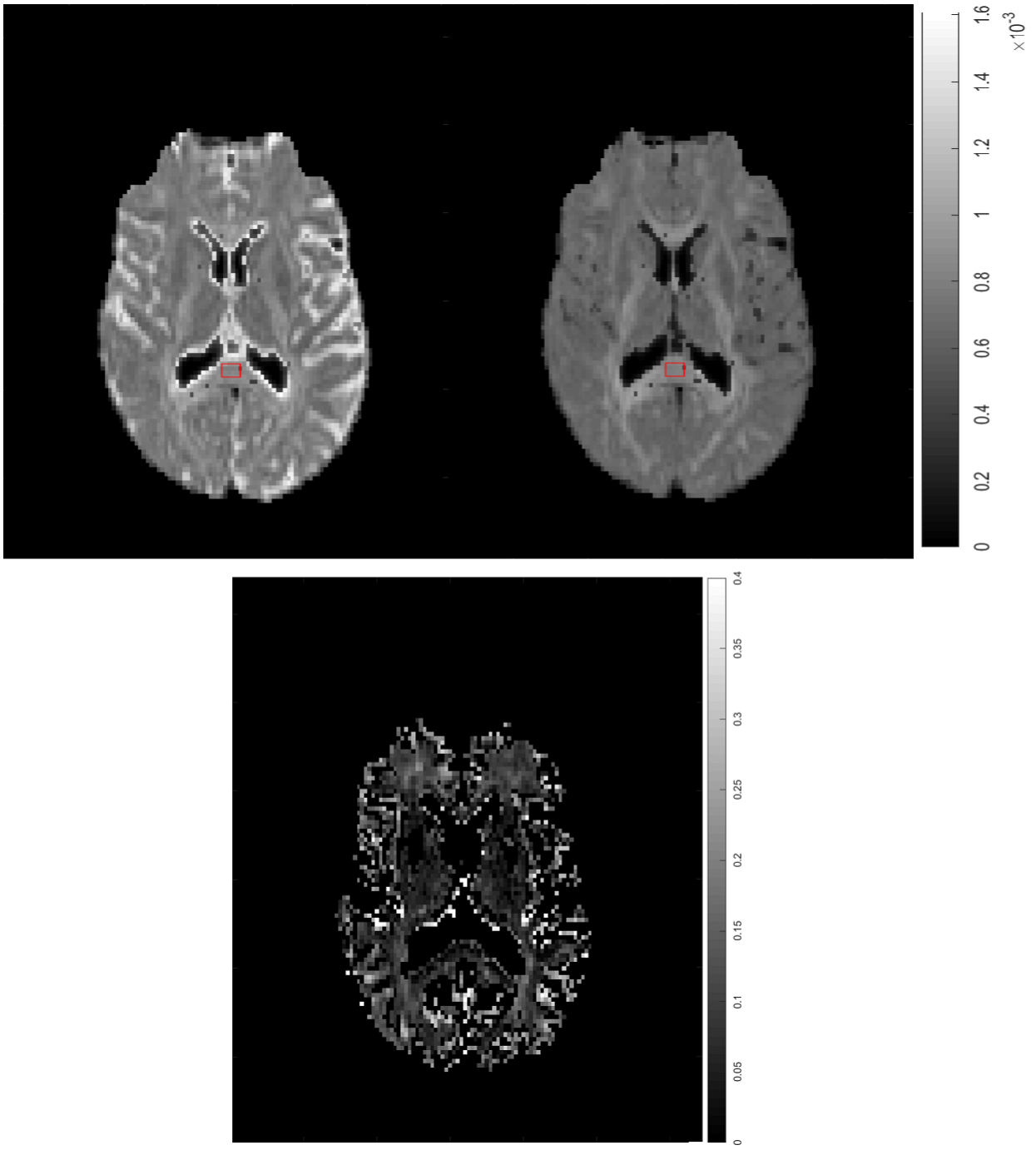

Figure 4.33: λ_1, from a random participant with MS the non-corrected visualization is on the top left, the top right is corrected, and the bottom is the difference.

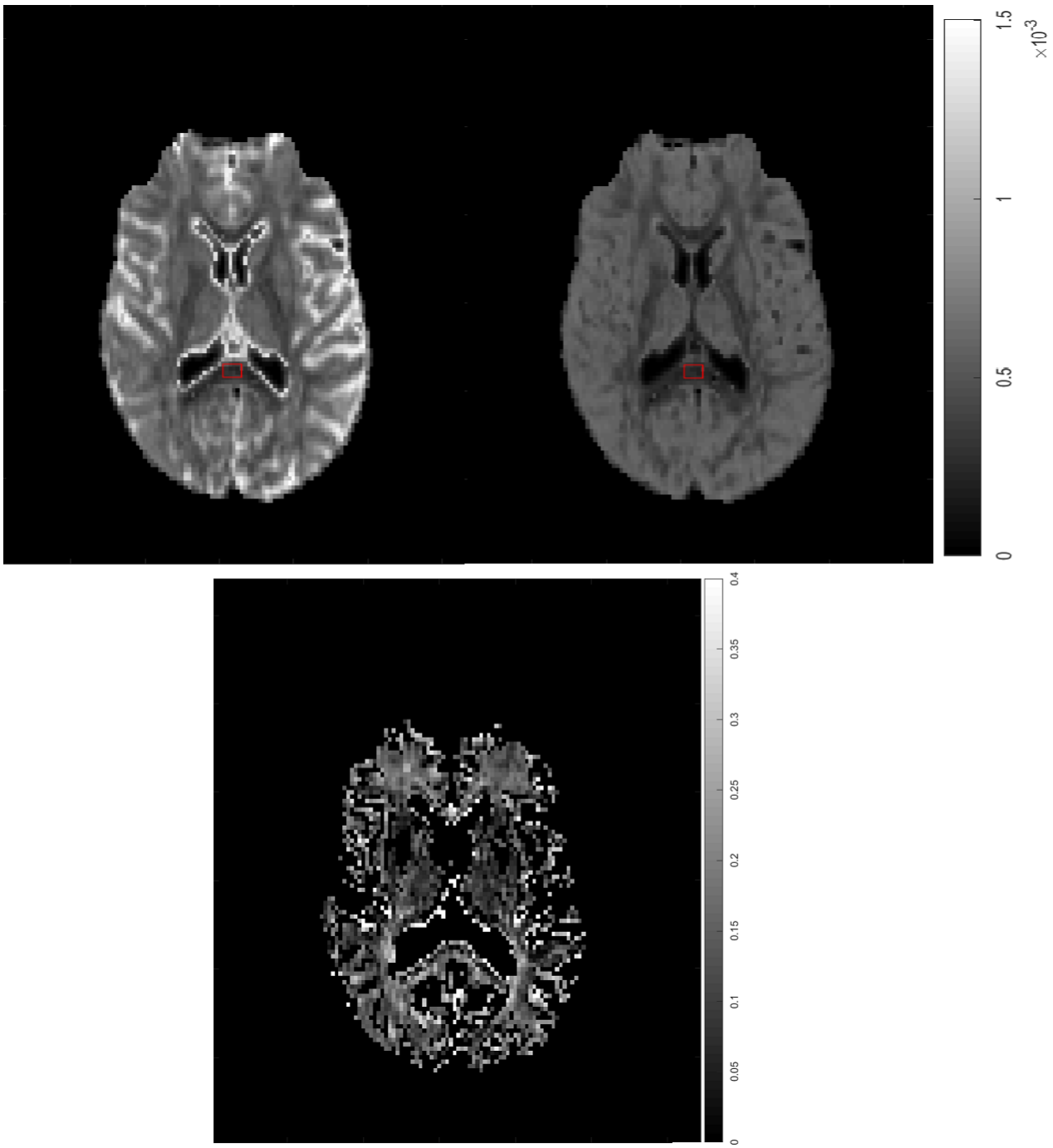

Figure 4.34: λ_2, from a random participant with MS the non-corrected visualization is on the top left, the top right is corrected, and the bottom is the difference.

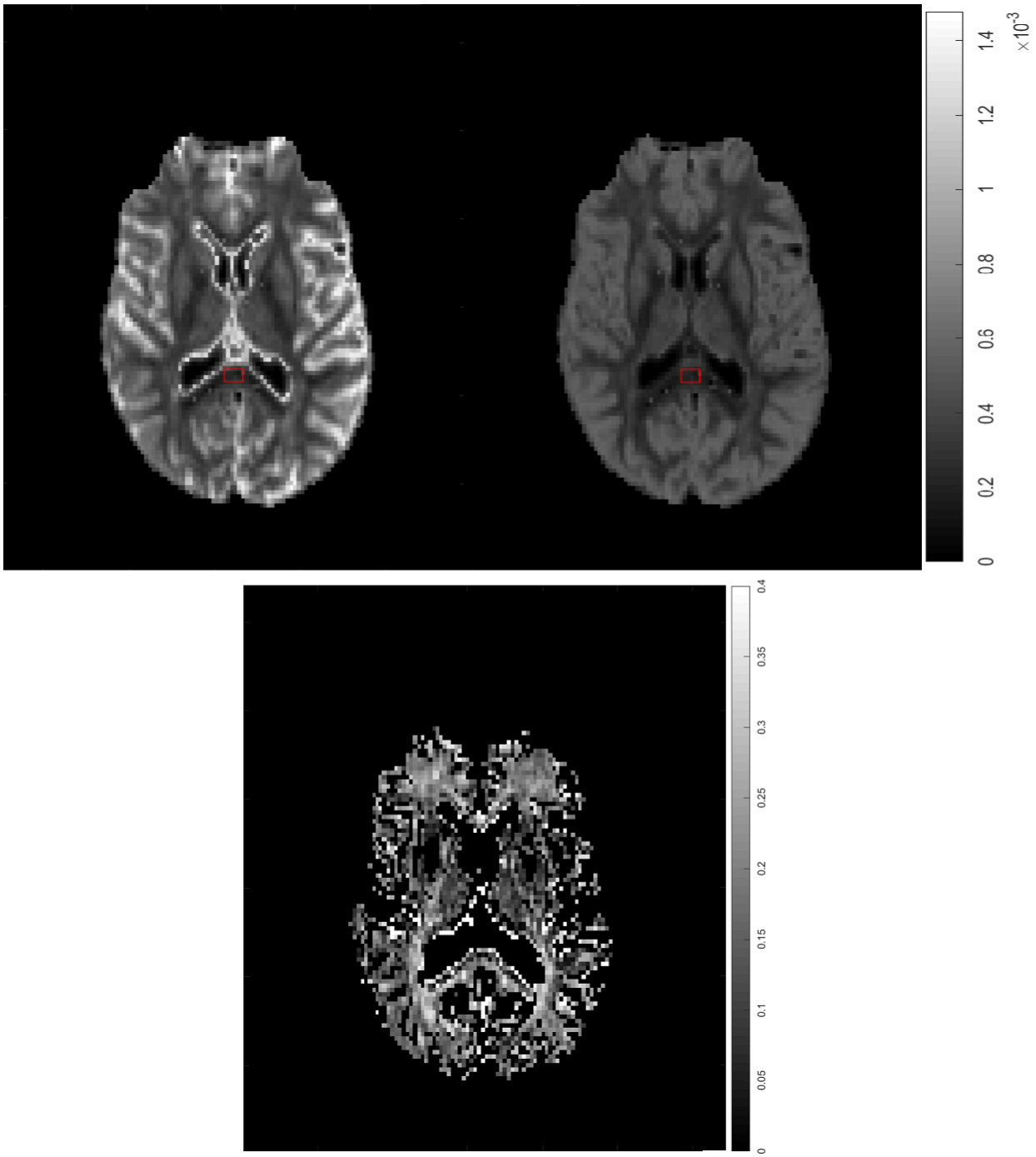

Figure 4.35: λ_3, from a random participant with MS the non-corrected visualization is on the top left, the top right is corrected, and the bottom is the difference.

4.2.2 Anisotropy and Diffusivity

Whole Brain Analysis

Because FWE changed λ_{123} similarly in the participants with MS and the healthy volunteers, the anisotropy indices are also affected similarly, table 4.18 and figure 4.36.

Index	Mean	Std	P-value	Change(%)
FA	0.185	0.006		
FA-fw	0.221	0.006	$p < 0.01$	19.27
MD(10^-4)	6.8	0.3		
MD-fw(10^-4)	4.9	0.1	$p < 0.01$	-27.73
RA	0.091	0.004		
RA-fw	0.110	0.004	$p < 0.01$	20.36
1-VR (10^-2)	6	1		
1-VR-fw (10^-2)	7.7	0.6	$p < 0.01$	32.50

Table 4.18: Values of FA, MD, RA, and VR for non-corrected and free water corrected data, for the whole brain of the participants with MS.

There is a significant increase in the FA, RA, and VR indices, indicating a significant increase in the anisotropy. MD is significantly decreased because λ_{123} were decreased by the free water correction.

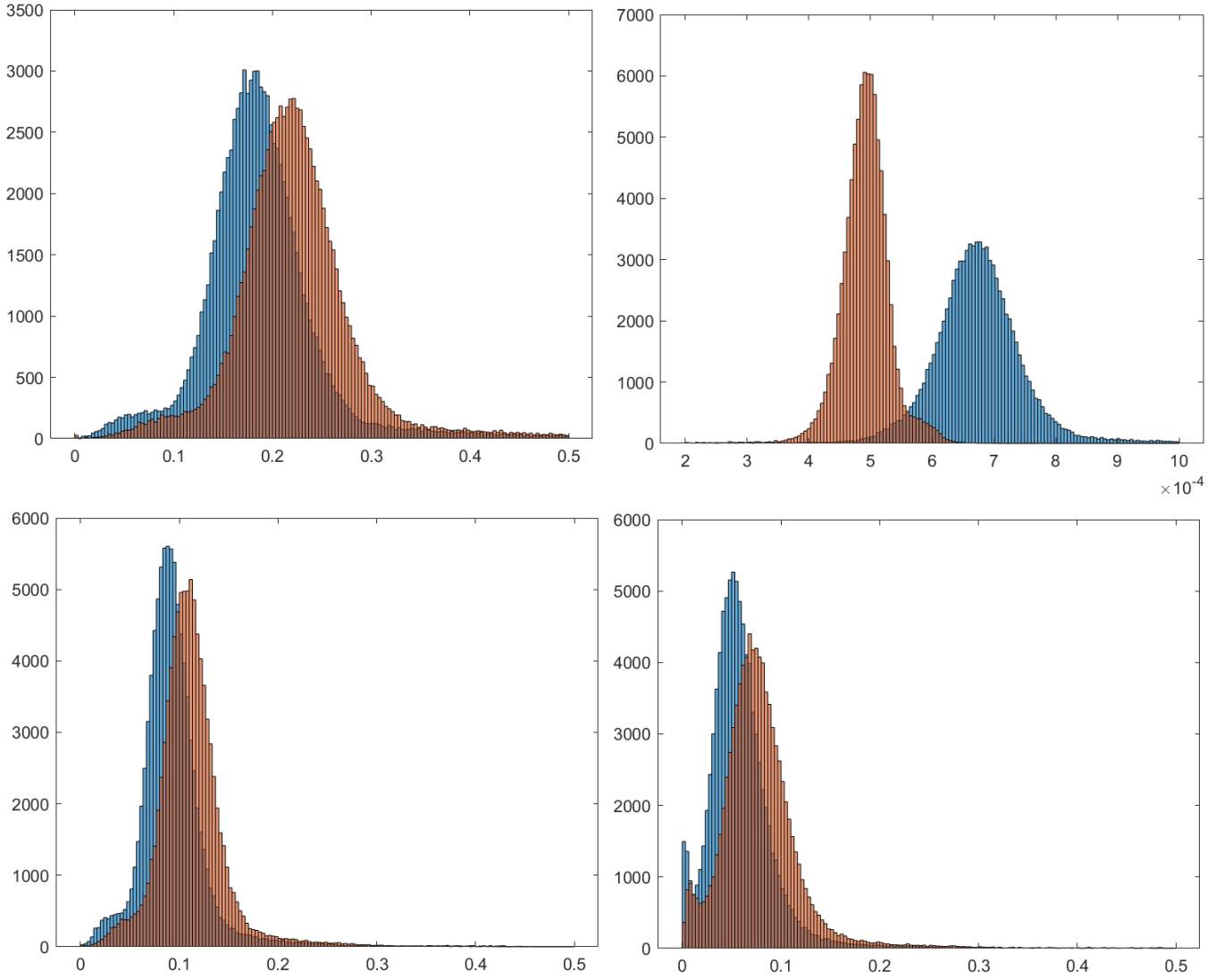

Figure 4.36: Histograms of FA, MD, RA, and VR from the whole brain analysis of the participants with MS. From top left to bottom right: FA, MD, RA, VR. Orange represents the free water correction data.

Grey Matter Analysis

Grey matter, being more isotropic than the rest of the brain, also has lower anisotropy indices, table 4.19 and figure 4.37, than the white matter or whole brain.

Index	Mean	Std	P-value	Change(%)
FA	0.108	0.004		
FA-fw	0.137	0.004	$p < 0.01$	26.03
MD(10^{-4})	7.3	0.2		
MD-fw (10^{-4})	5.65	0.07	$p < 0.01$	-22.09
RA	0.052	0.002		
RA-fw	0.065	0.003	$p < 0.01$	26.70
1-VR($10^{-}2$)	1.5	0.3		
1-VR-fw ($10^{-}2$)	2.4	0.4	$p < 0.01$	57.60

Table 4.19: FA, MD, RA, and VR for the segmented grey matter in the participants with MS.

The anisotropy indices show a significant increase from the free water correction. The anisotropy indices were lower than the white matter, corpus callosum and whole brain analysis, but the increase when correcting for free water contamination was slightly higher than when looking at the brain indiscriminately.

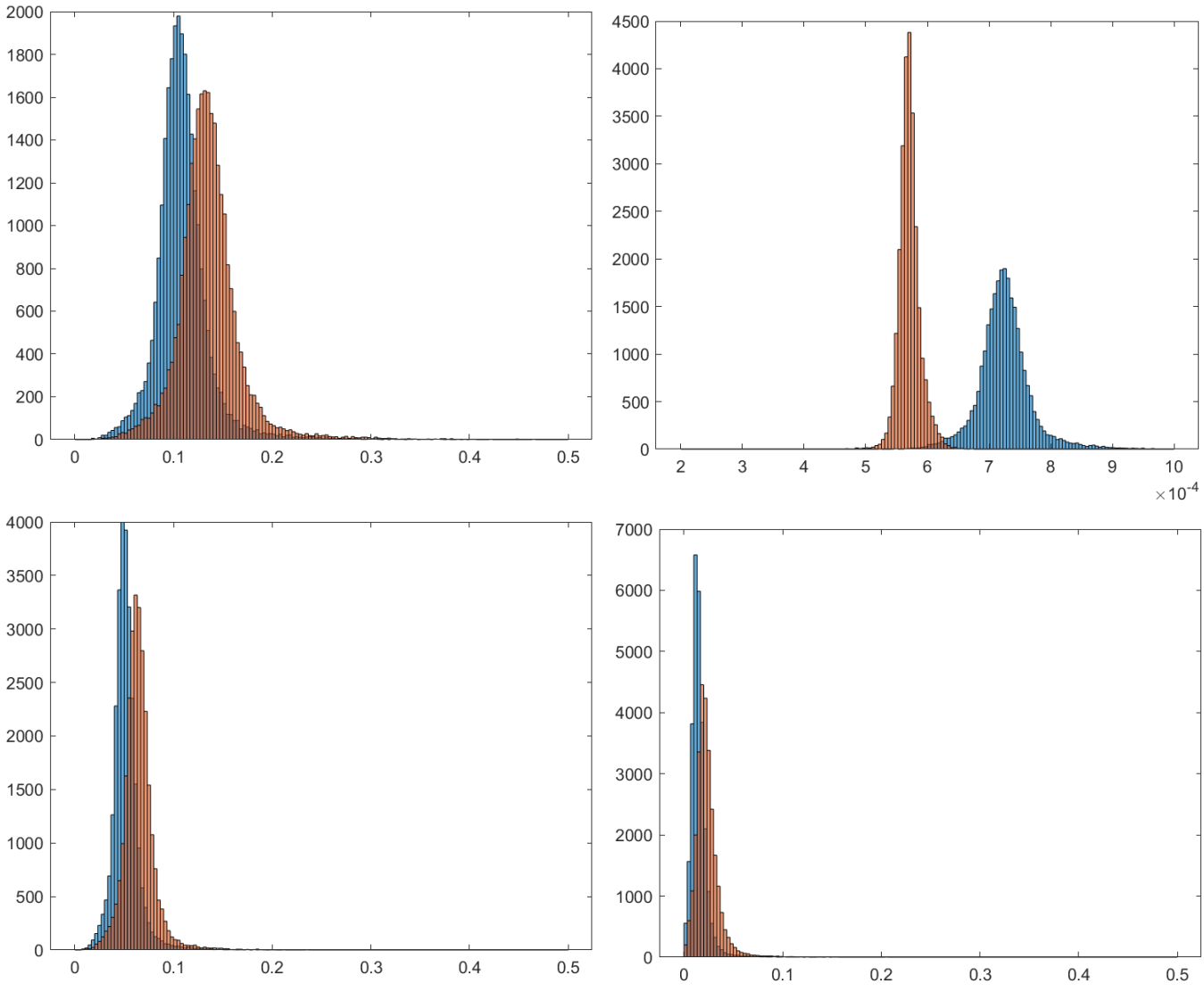

Figure 4.37: Histograms of FA, MD, RA, and VR from grey matter in the participants with MS. From top left to bottom right: FA, MD, RA, VR. Orange represents the free water correction data.

White Matter Analysis

The anisotropy indices in the white matter in the participants with MS are changed significantly, table 4.20 and figure 4.38, but the change is less for most indices in the white matter compared to grey matter or whole brain.

Index	Mean	Std	P-value	Change(%)
FA	0.338	0.005		
FA-fw	0.379	0.005	$p < 0.01$	12.21
MD(10^{-4})	5.53	0.06		
MD-fw (10^{-4})	4.84	0.04	$p < 0.01$	-12.32
RA	0.170	0.003		
RA-fw	0.193	0.004	$p < 0.01$	14.05
1-VR ($10^{-}2$)	13.4	0.6		
1-VR-fw ($10^{-}2$)	17.0	0.7	$p < 0.01$	26.86

Table 4.20: FA, MD, RA, and VR for the segmented white matter in participants with MS.

The anisotropy indices are larger than in the segmented grey matter and when the whole brain is indiscriminately analyzed. This is as expected, since the white matter is expected to be more anisotropic, the change introduced by the free water correction is also lower than the two previous analyses. The VR changed more in the white matter than in the whole brain analysis.

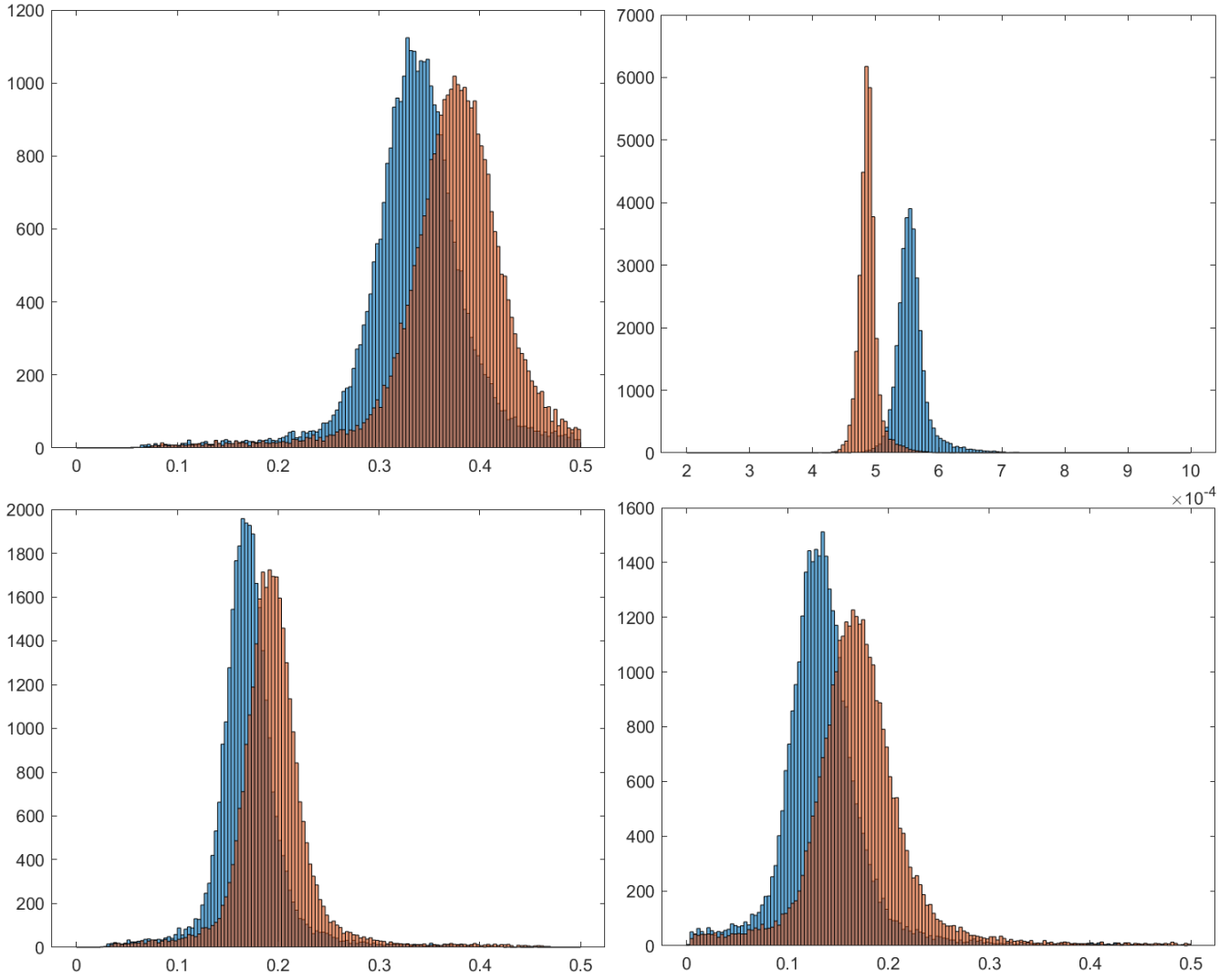

Figure 4.38: Histograms of FA, MD, RA, and VR from white matter in the participants with MS. From top left to bottom right: FA, MD, RA, VR. Orange represents the free water correction data.

Selected ROI in Corpus Callosum

In corpus callosum, there is an increase in the anisotropy, table 4.21 and figure 4.39. Because this is an area of high anisotropy and little to no free water contamination, the change is smaller than in the white matter, grey matter or the whole brain.

Index	Mean	Std	P-value	Change(%)
FA	0.64	0.01		
FA-fw	0.69	0.01	$p < 0.01$	8.42
MD(10^{-4})	4.93	0.08		
MD-fw(10^{-4})	4.4	0.1	$p < 0.01$	-10.99
RA	0.35	0.01		
RA-fw	0.40	0.01	$p < 0.01$	12.74
1-VR ($10^{-}2$)	41	1		
1-VR-fw ($10^{-}2$)	49	2	$p < 0.01$	19.74

Table 4.21: Values of FA, MD, RA, and VR for corpus callosum, in the participants with MS.

Figures 4.40, 4.41, 4.42, and 4.43, shows the FA, MD, RA, and VR, respectively. In all figures, the top image is the non-corrected one, while the bottom has been corrected for free water.

Figure 4.44 shows the volume ratio visualizations with a threshold applied(< 0.8) to better visualize the difference between the corrected and non-corrected data. The red box denotes the ROI used in the corpus callosum analysis. In all figures, the window level has been kept the same for the corrected and non-corrected to have a better comparison.

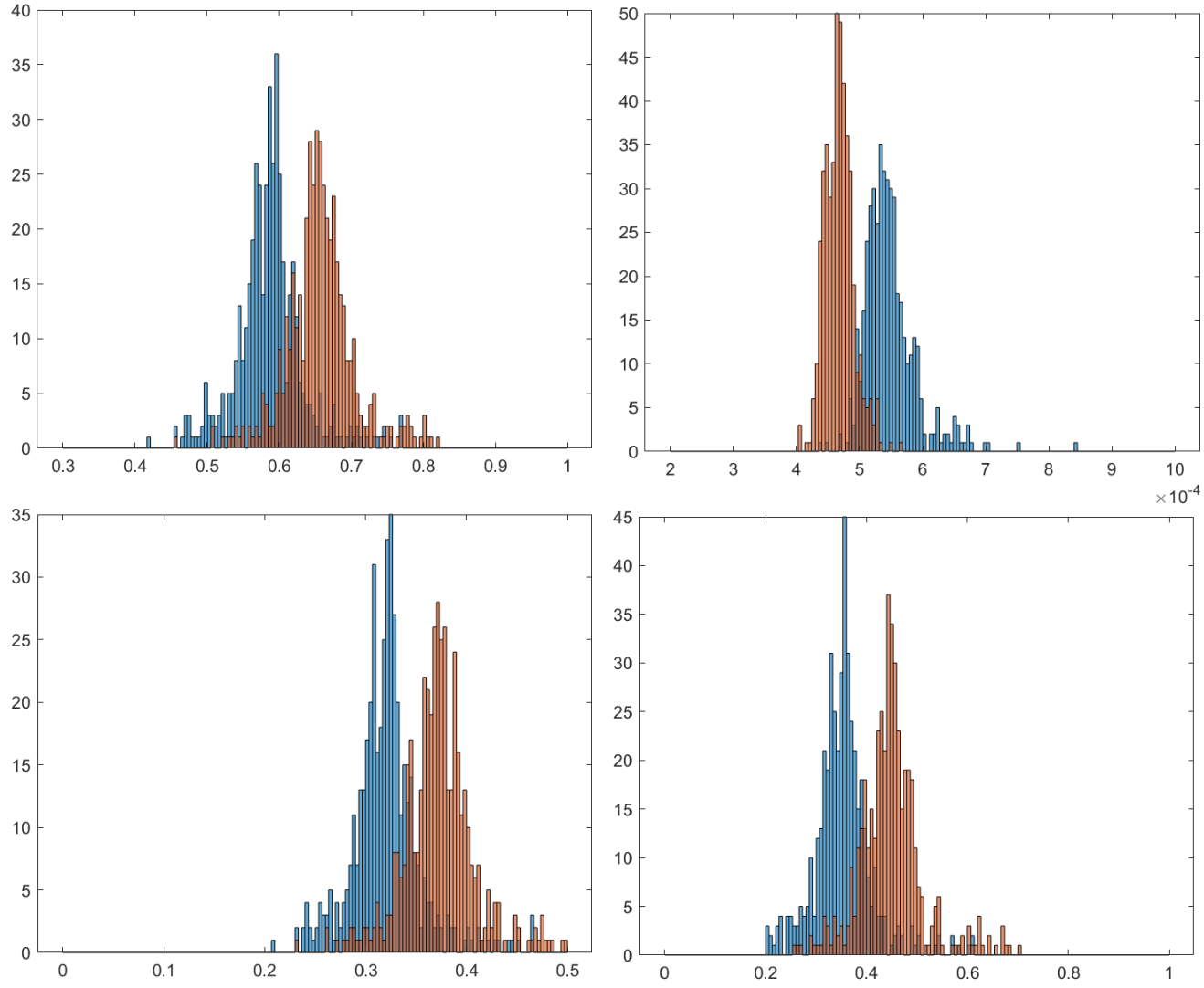

Figure 4.39: Histograms of FA, MD, RA, and VR from corpus callosum in the participants with MS. From top left to bottom right: FA, MD, RA, VR. Orange represents the free water correction data.

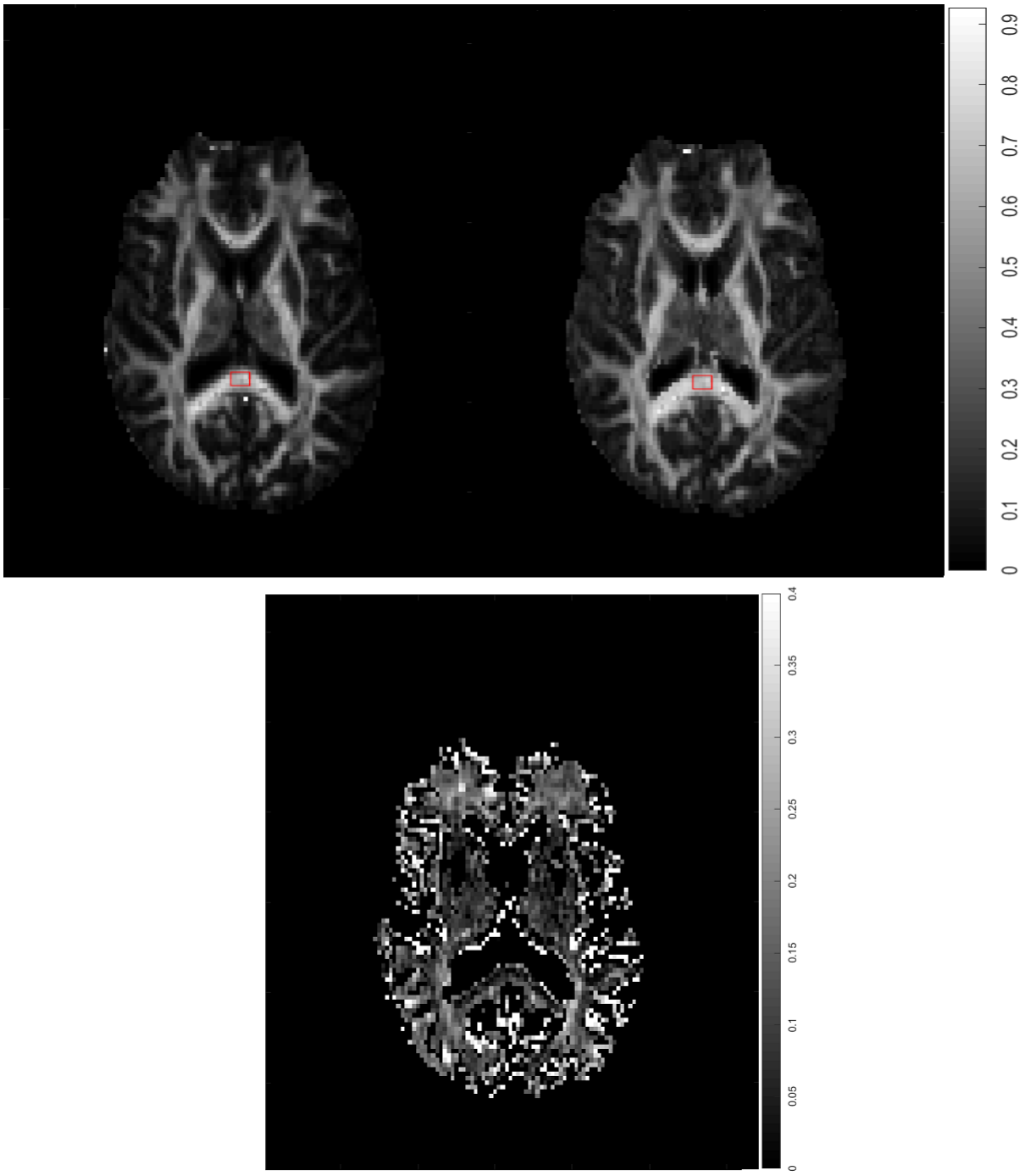

Figure 4.40: FA maps, top left is non-corrected, top right is corrected, and the bottom is the difference, in a participant with MS.

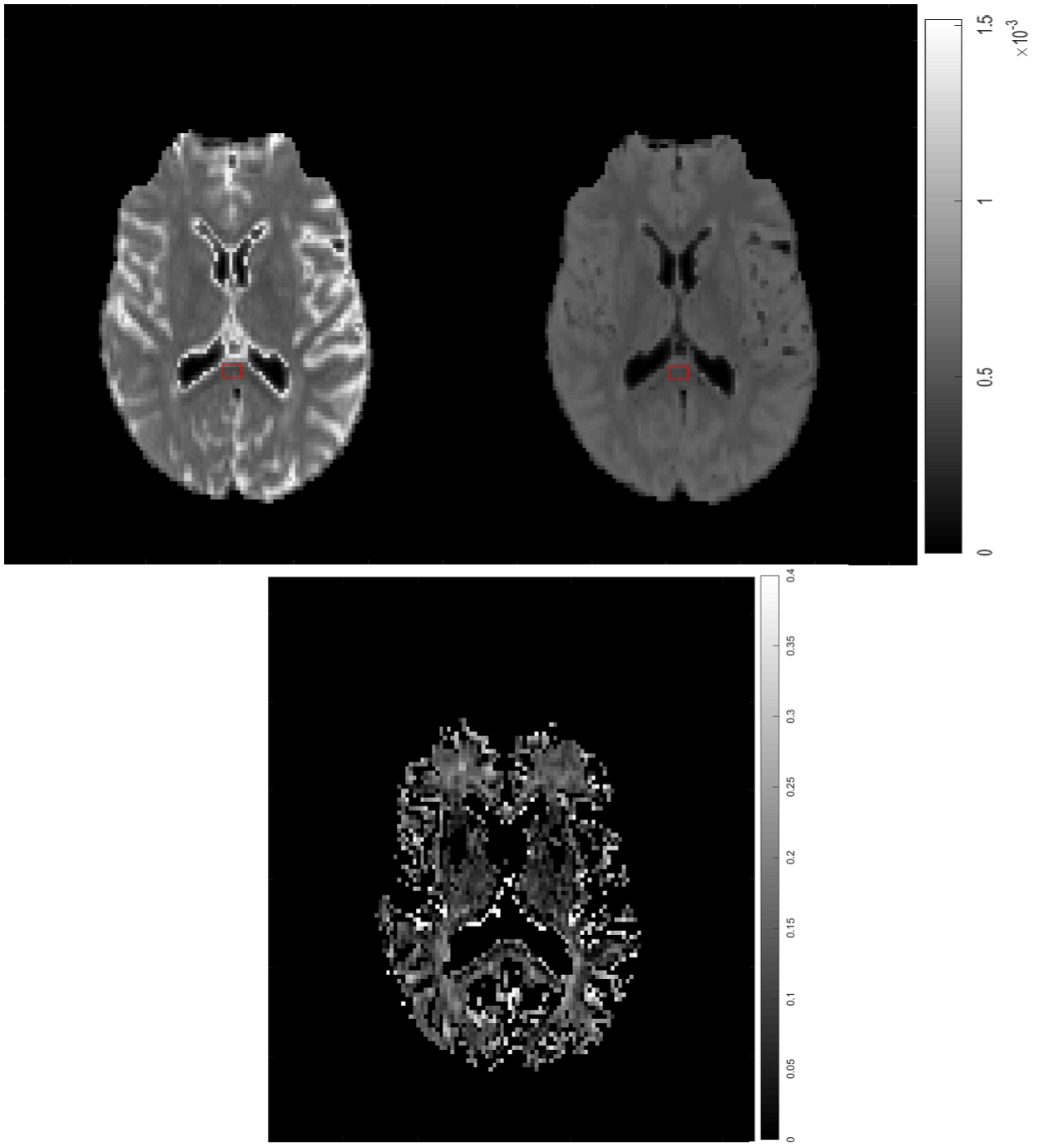

Figure 4.41: MD maps, top left is non-corrected, top right is corrected, and the bottom is the difference, in a participant with MS.

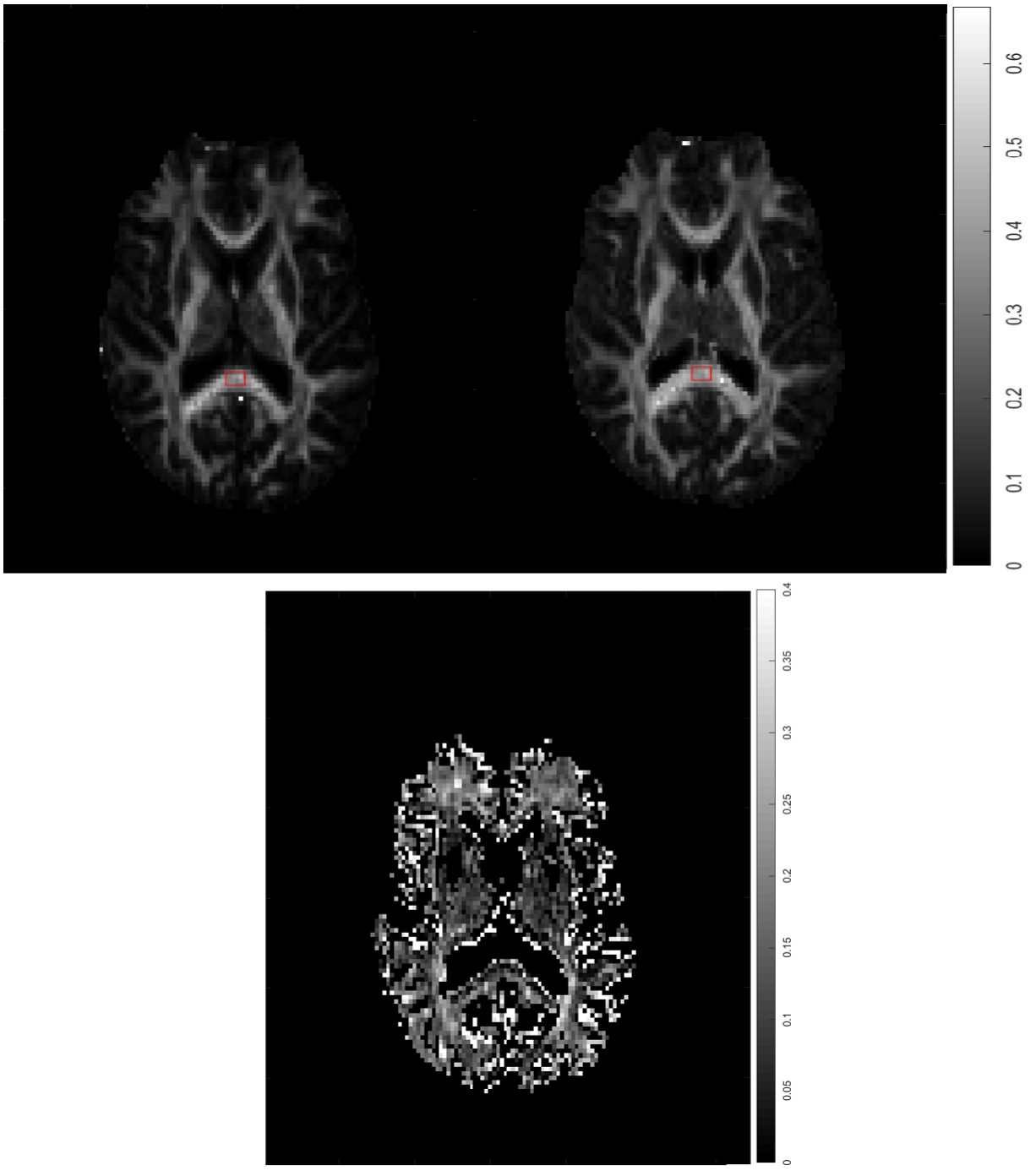

Figure 4.42: RA maps, top left is non-corrected, top right is corrected, and the bottom is the difference, in a participant with MS.

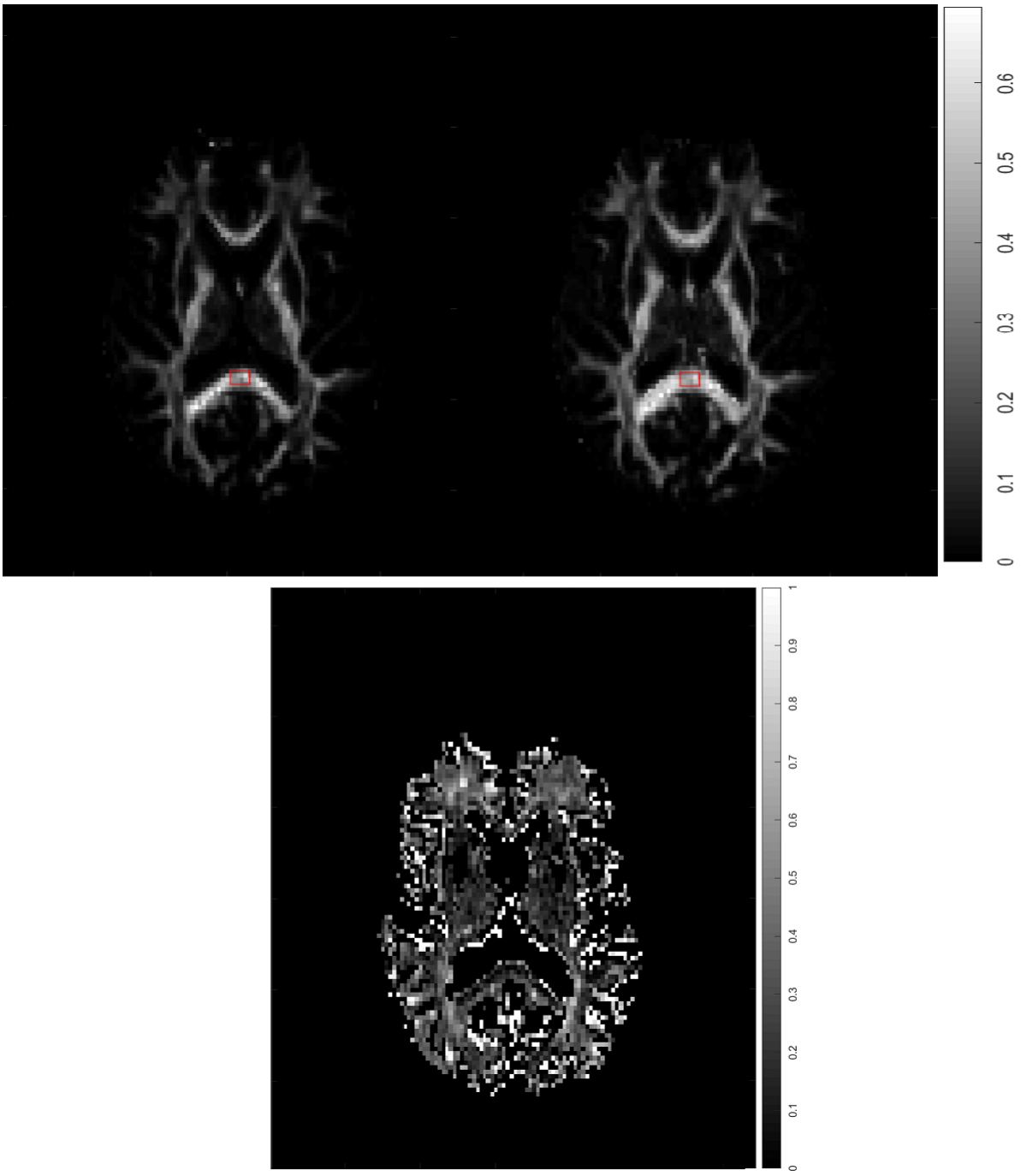

Figure 4.43: VR maps, top left is non-corrected, top right is corrected, and the bottom is the difference, in a participant with MS. Note that the window level in the difference image is not the same as that of the FA, MD, and RA difference images.

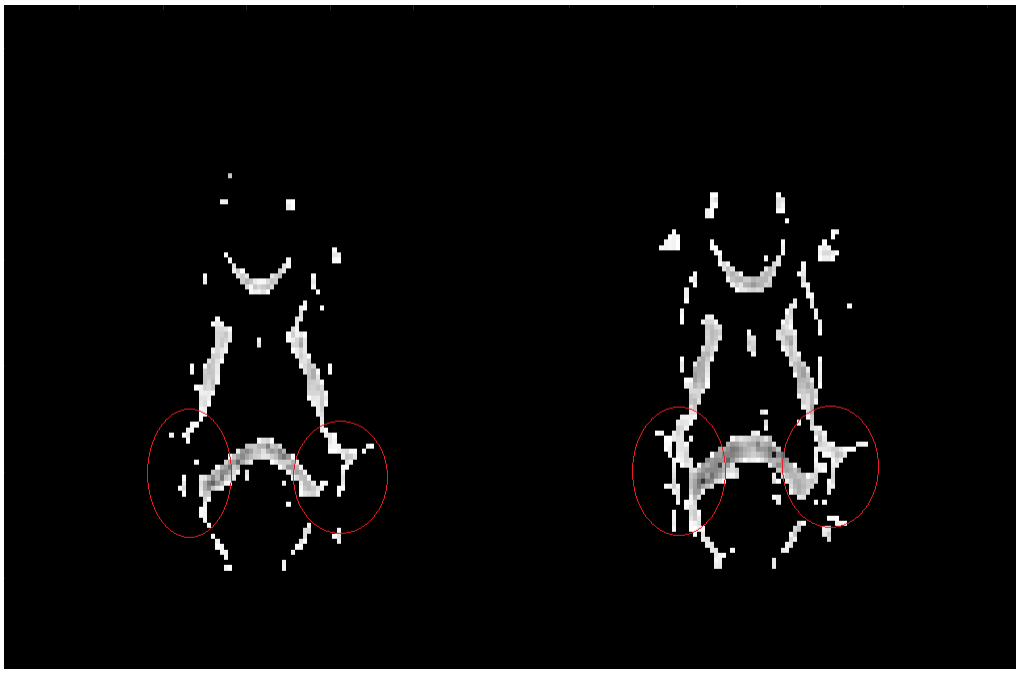

Figure 4.44: Non-corrected(left) and corrected(right) VR image with an applied threshold ($VR < 0.8$), showing an increase in VR in two areas where there are crossing fibers, in a participant with MS.

4.2.3 Other Rotationally Invariant Indices

Whole Brain Analysis

The invariant indices discussed in section 2.2.1 are important, as they contain information on the size relation of the three eigenvalues as shown in equations 2.47, 2.48, and 2.49. Because they directly describe the relationship between λ_{123} they are changed significantly, table 4.22 and figure 4.45.

Index	Mean (10^{-2})	Std (10^{-2})	P-value	Change(%)
cl	8.0	0.4		
cl FW	9.6	0.5	$p < 0.01$	20.63
cp	8.8	0.5		
cp FW	10.6	0.3	$p < 0.01$	20.83
cs	80	2		
cs FW	75	2	$p < 0.01$	-6.19

Table 4.22: Invariant indices for the non-corrected and free water corrected data for the whole brain in participants with MS.

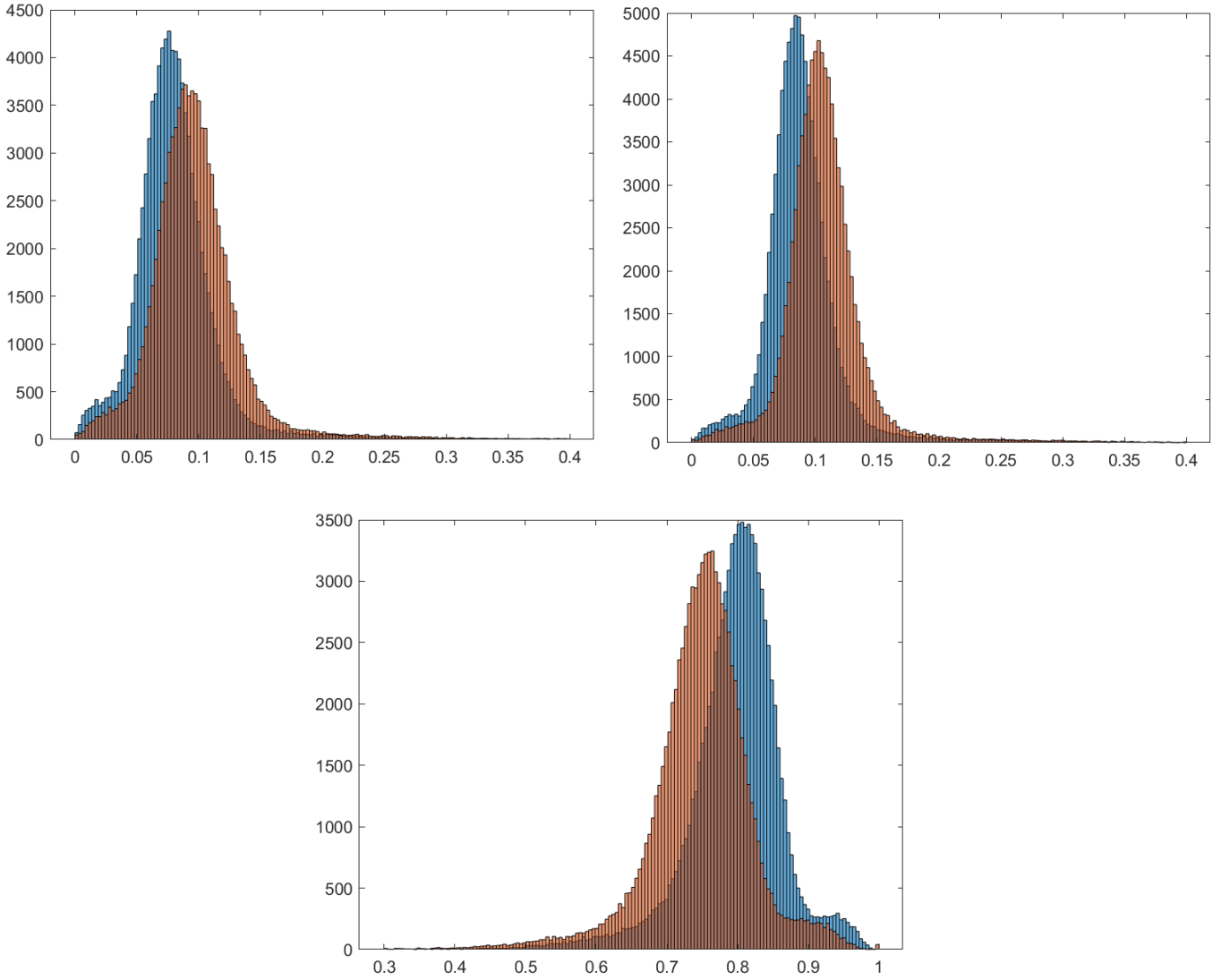

Figure 4.45: Histograms of cl, cp, and cs from the whole brain analysis in the participants with MS. From top left to bottom: cl, cp, cs. Orange represents the free water correction data.

Grey Matter Analysis

Looking at these invariant indices in the grey matter parts of the brain yield generally lower indices due to a higher degree of isotropy, table 4.23 and figure 4.46.

The invariant indices in the grey matter are generally lower when compared to the whole brain, table 4.22. As shown later the white matter, table 4.24, and corpus callosum, table 4.25, have higher degrees of anisotropy, therefore also higher values of these three indices.

Index	Mean (10^{-2})	Std (10^{-2})	P-value	Change(%)
cl	4.1	0.2		
cl FW	5.2	0.3	$p < 0.01$	26.73
cp	5.9	0.3		
cp FW	7.5	0.2	$p < 0.01$	26.52
cs	89.9	0.4		
cs FW	87.1	0.4	$p < 0.01$	-3.11

Table 4.23: Invariant indices for the segmented grey matter in the brain, in the participants with MS.

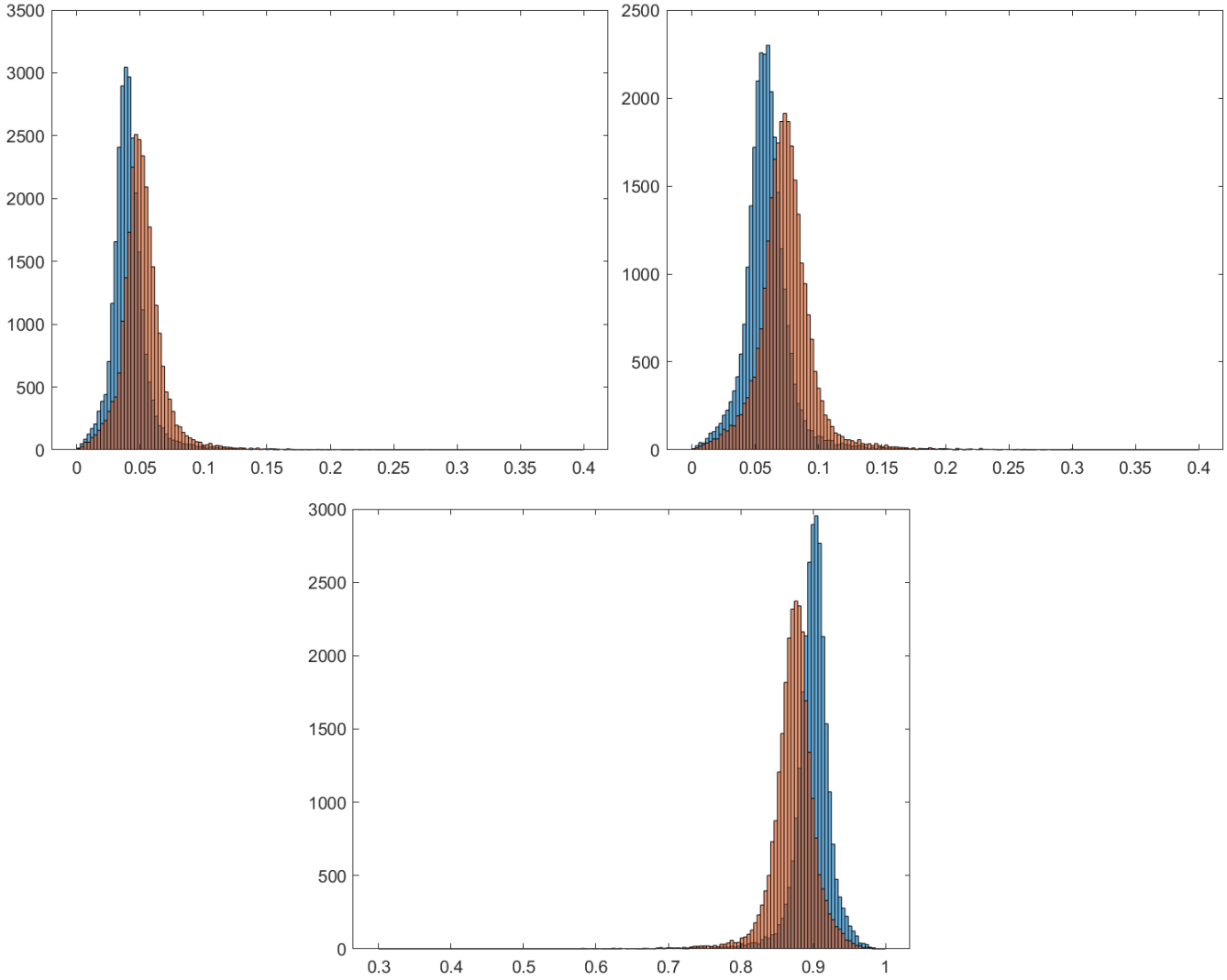

Figure 4.46: Histograms of cl, cp and cs from grey matter in the participants with MS. From top left to bottom right: cl, cp, cs. Orange represents the free water correction data.

White Matter Analysis

The anisotropy in white matter is higher than the whole brain and lower than corpus callosum, this is reflected in the invariant indices, table 4.24 and figure 4.47.

Index	Mean (10^{-2})	Std (10^{-2})	P-value	Change(%)
cl	15.6	0.5		
cl FW	17.8	0.6	$p < 0.01$	14.14
cp	14.6	0.3		
cp FW	16.6	0.3	$p < 0.01$	13.59
cs	69.7	0.4		
cs FW	65.4	0.5	$p < 0.01$	-7.07

Table 4.24: Invariant indices for the segmented white matter in the brain, in the participants with MS.

The white matter indices are between the whole brain analysis, table 4.22 and corpus callosum, table 4.25. The change is less than the grey matter, table 4.23, for the cl and cp indices, the spread is also lower than the grey matter.

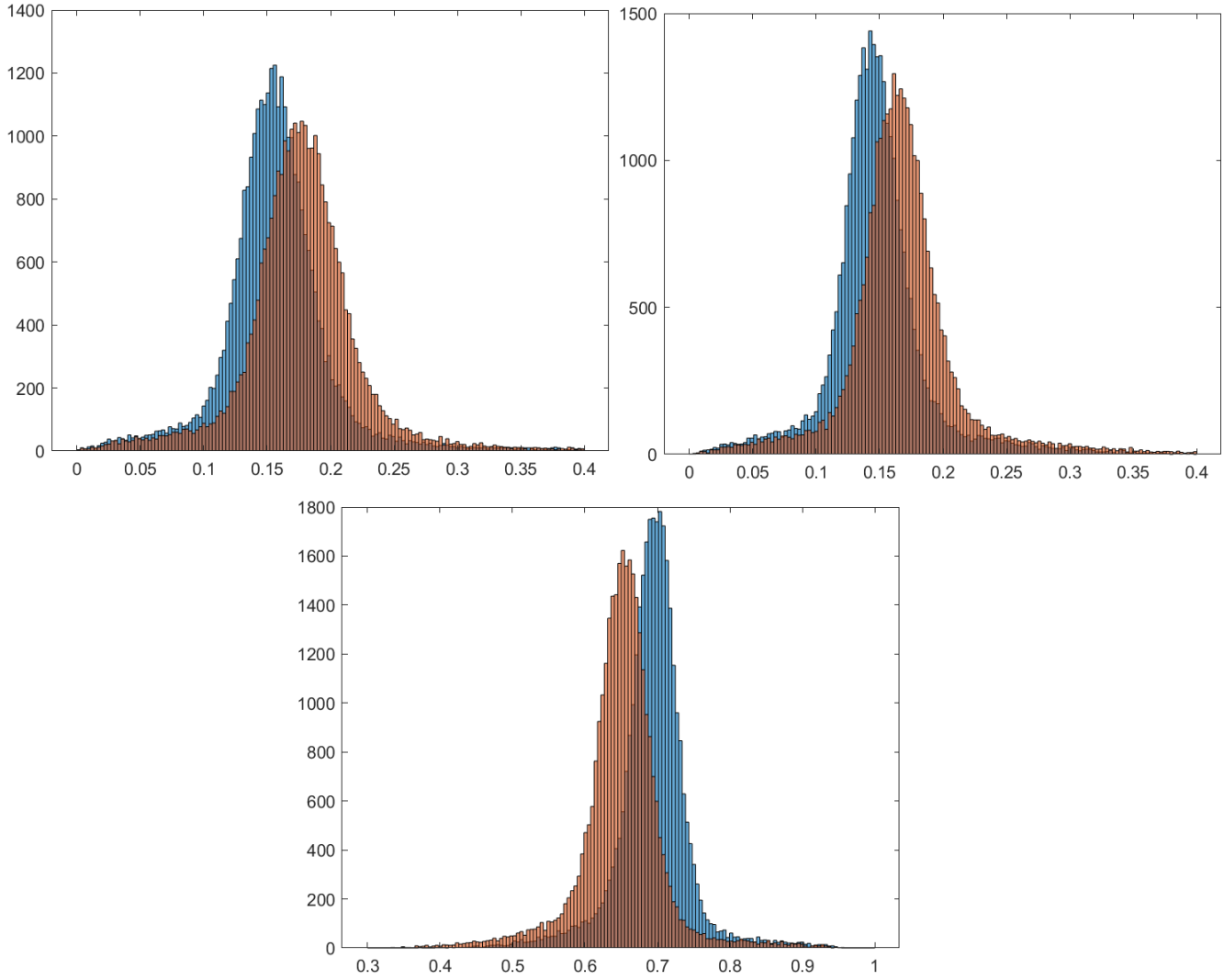

Figure 4.47: Histograms of cl, cp and cs from white matter in the participants with MS. From top left to bottom right: cl, cp, cs. Orange represents the free water correction data.

Selected ROI in Corpus Callosum

The invariant indices for corpus callosum, the chosen area is shown as the red box in all relevant visualizations. This is the region with the highest degree of anisotropy, therefore there is a high degree of linearity in the diffusion vector, 4.25 and figure 4.48.

Index	Mean(10^{-2})	Std(10^{-2})	P-value	Change(%)
cl	41	1		
cl FW	45	1	$p < 0.01$	11.13
cp	10	1		
cp FW	11	2	$p = 0.30$	10.33
cs	49.2	0.9		
cs FW	43	1	$p < 0.01$	-12.70

Table 4.25: Invariant indices for corpus callosum, in the participants with MS.

The increase in cl is as expected, from the sharpening of the tensor, the same goes for the increase in cp. The effect of the free water correction is visualized in figures 4.49, 4.50, 4.51, and 4.52. These figures show the indices cl, cp, and cs with their respective difference visualizations. Figure 4.50 shows cl with a threshold ($0.2 < cl < 0.6$) applied to better visualize the change imposed by the free water correction. In all figures, the top image is the non-corrected, and the bottom has been corrected for free water contamination.

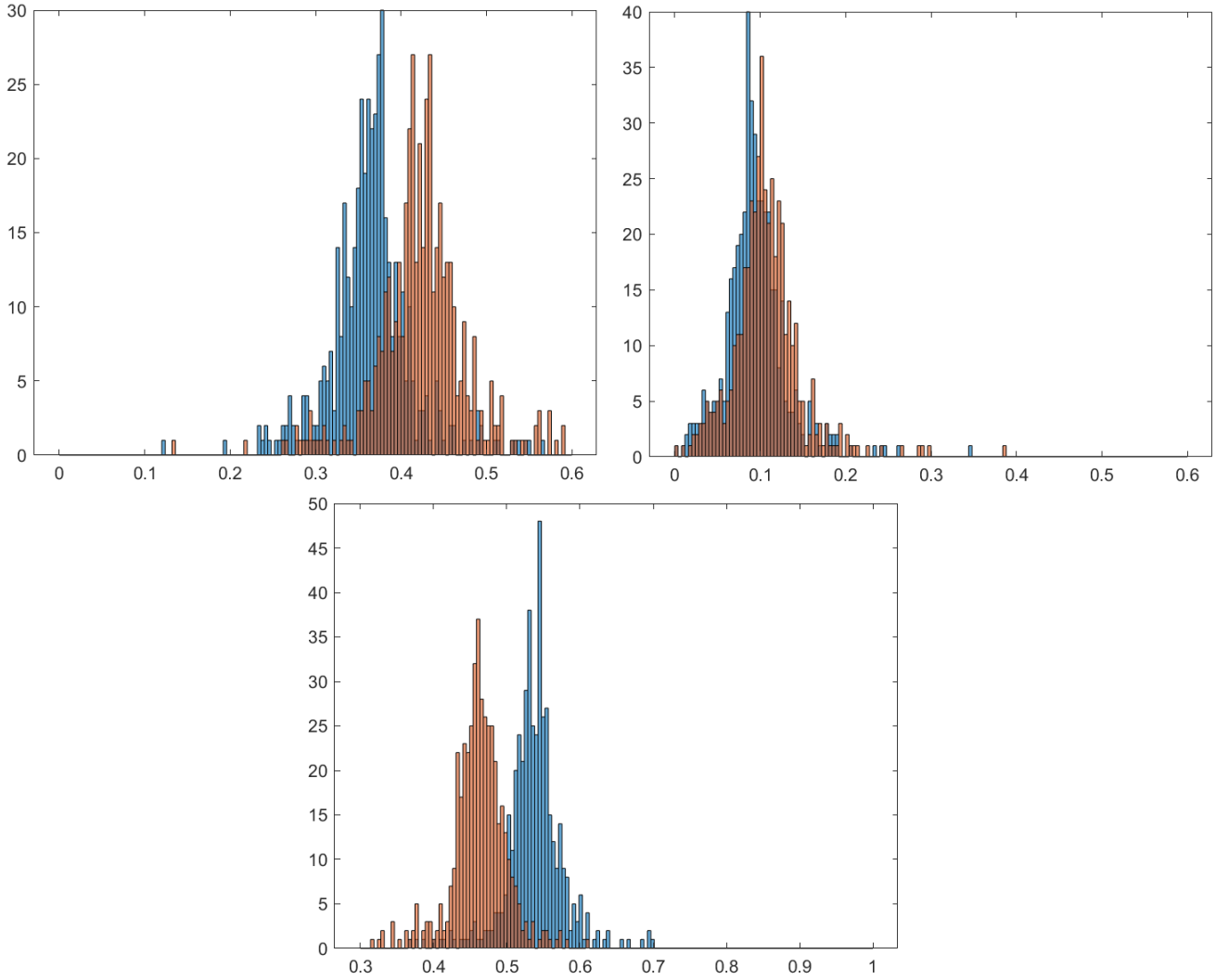

Figure 4.48: Histograms of cl, cp and cs from corpus callosum in the participants with MS. From top left to bottom right: cl, cp, cs. Orange represents the free water correction data.

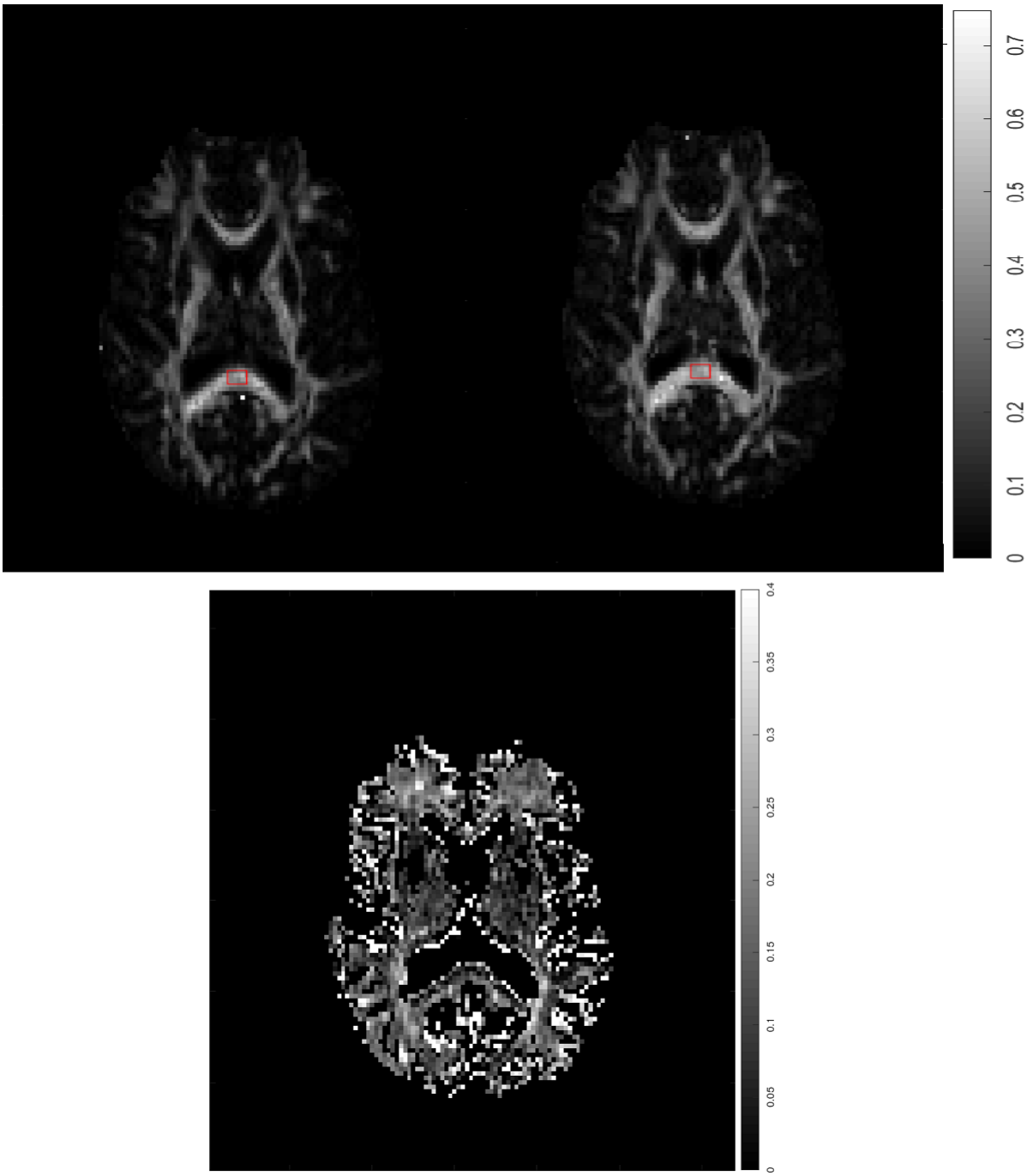

Figure 4.49: Cl, equation 2.47. Top left is non-corrected, top right is corrected and on the bottom is the difference.

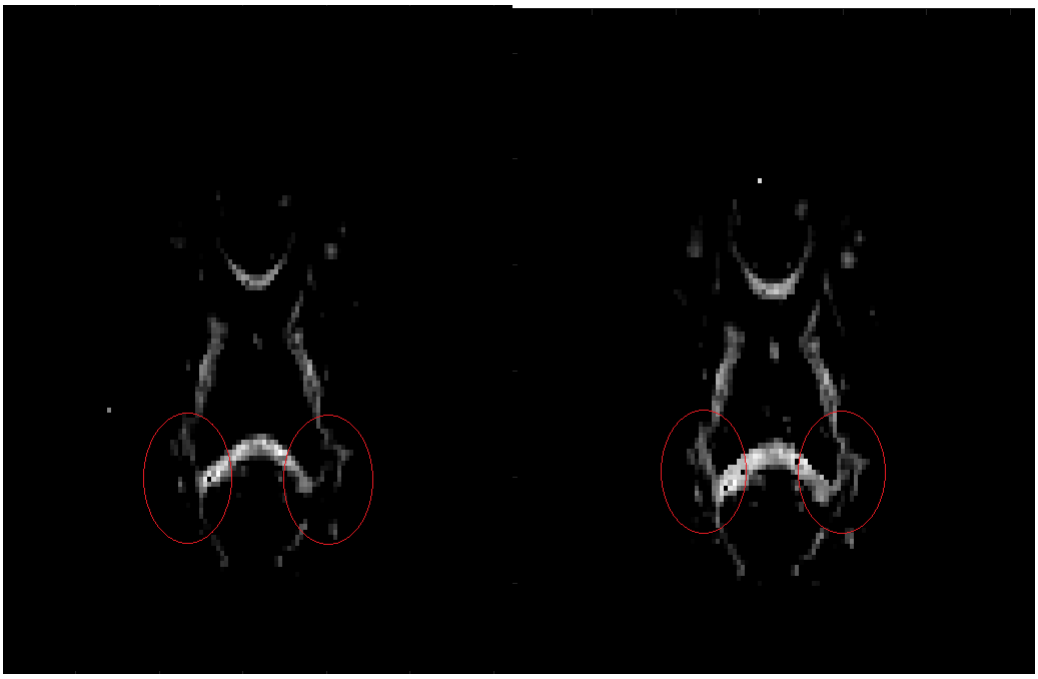

Figure 4.50: Cl shown in figure 4.22 with the high ($cl > 0.6$) and low ($cl < 0.2$) values removed to better visualize the difference between the two, the red rings show the areas where the correction is the most visible.

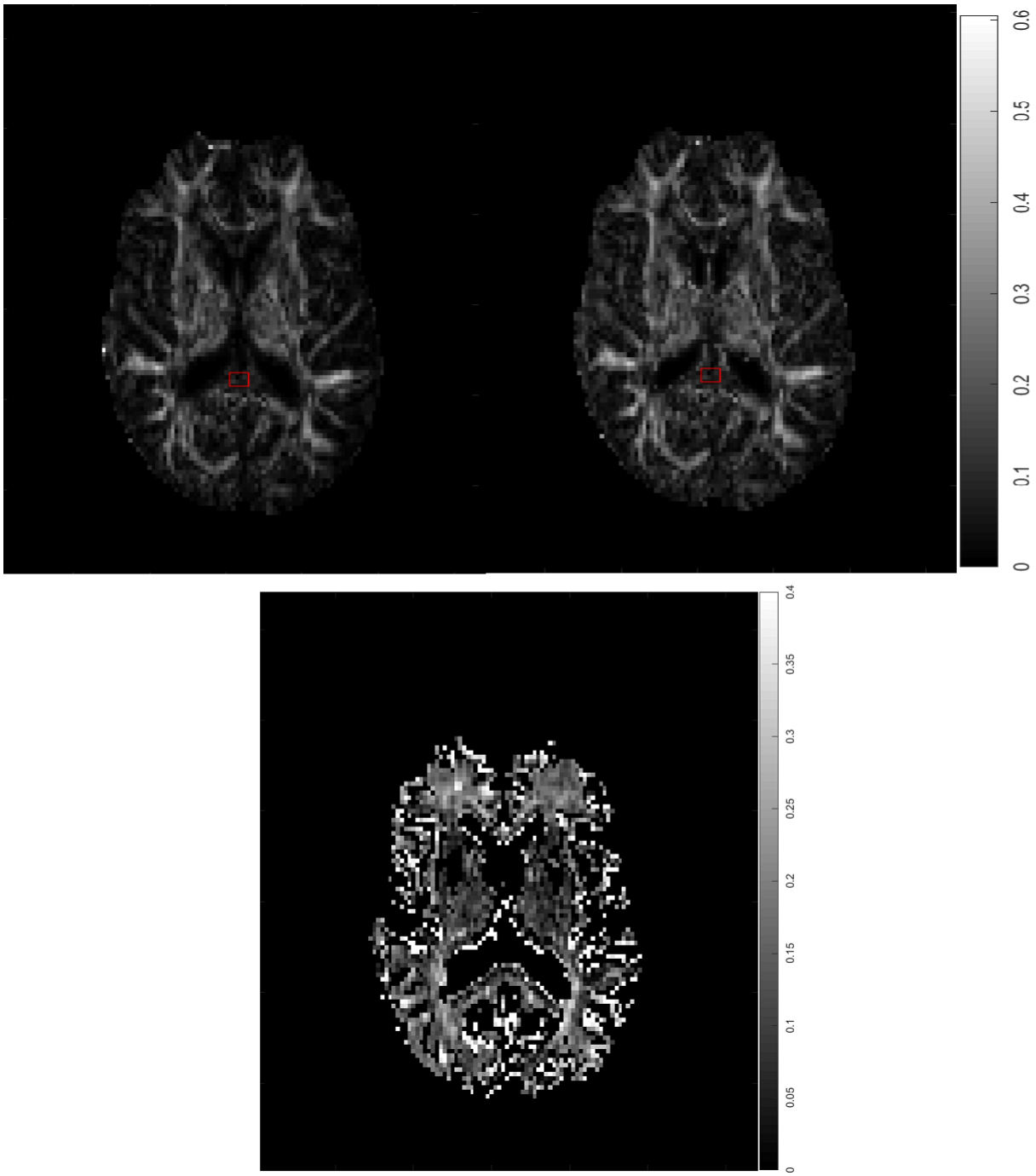

Figure 4.51: Cp, equation 2.47. Top left is non-corrected, top right is corrected and on the bottom is the difference.

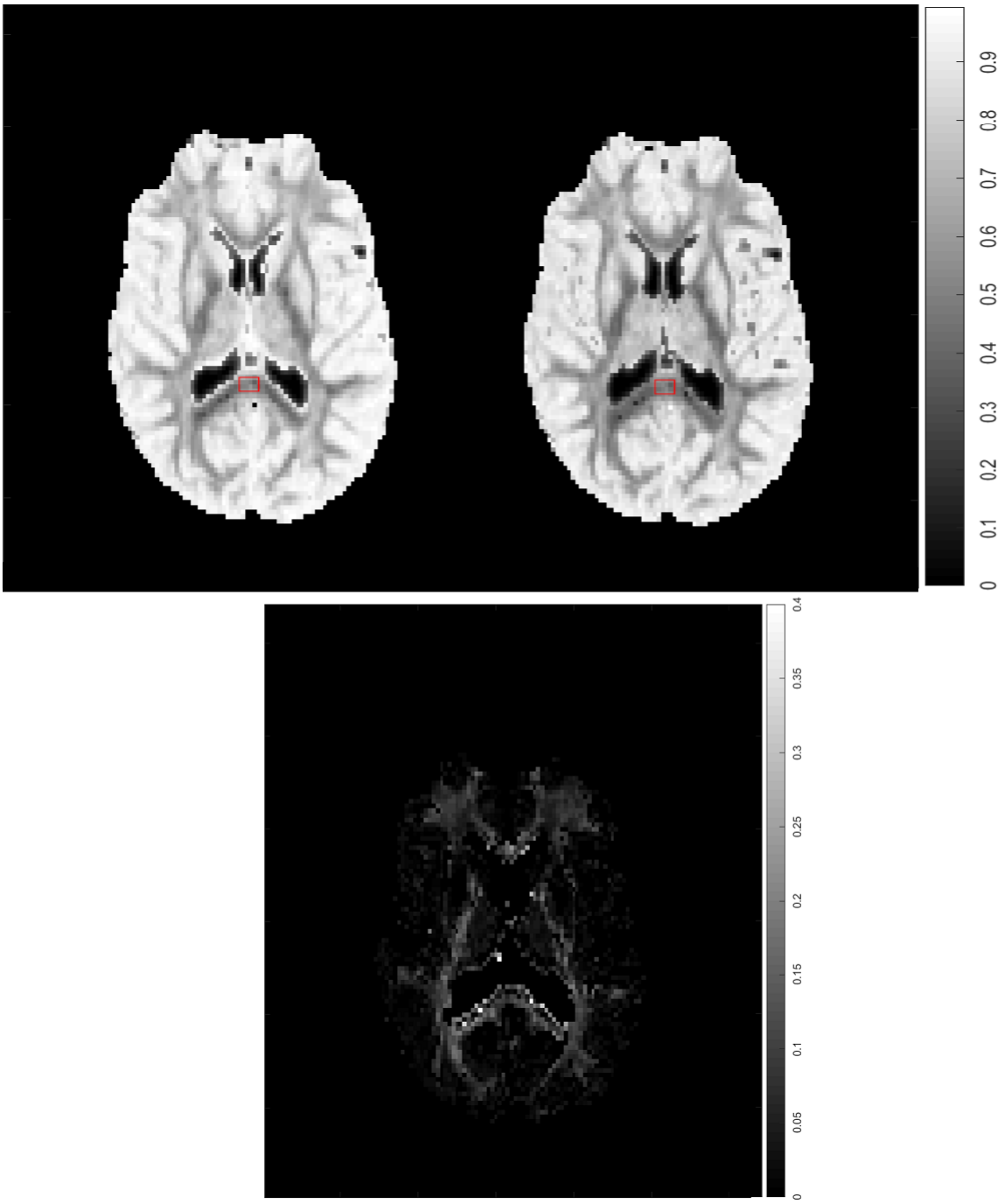

Figure 4.52: Cs, equation 2.49. Note that due to $cl + cp + cs = 1$ the intensity in the visualization is inverted, areas with high anisotropy are darker. The top left is non-corrected, top right is corrected and on the bottom is the difference.

4.2.4 Fiber Tractography

Selected ROI in Corpus Callosum

The fiber tractography results follows the brute-force technique laid out in section 2.2.1. The analysis was done on one random brain. The results were gathered using a thin ROI in the corpus callosum seen in figure 4.53 and 4.54 using the fiber tractography algorithm used in NordicIce (Nordic NeuroLabs Inc, Bergen, Norway). Due to the significant increase in anisotropy induced by FWE, there are also more fibers found in corpus callosum, table 4.26, this analysis was only done on one participant.

Parameters	Fibers FW	FA FW	Std FW	Fibers	FA	Std
40°, $FA > 0.300$	4789	0.6	0.1	2663	0.6	0.1
40°, $FA > 0.200$	5743	0.6	0.2	4127	0.5	0.2
40°, $FA > 0.100$	6757	0.6	0.2	6092	0.4	0.2
50°, $FA > 0.300$	4870	0.6	0.1	2628	0.6	0.1
50°, $FA > 0.200$	5853	0.6	0.2	4107	0.5	0.2
50°, $FA > 0.100$	7395	0.5	0.2	6460	0.4	0.2
60°, $FA > 0.300$	4984	0.6	0.1	2663	0.6	0.1
60°, $FA > 0.200$	6055	0.6	0.2	3647	0.5	0.1
60°, $FA > 0.100$	7955	0.5	0.2	6736	0.4	0.2

Table 4.26: Fiber tractography data from NordicIce, the parameters denote the cutoff angle and the FA threshold as discussed in section 2.2.1.

Figures 4.53 and 4.54 are the different fiber tractographies. The top images, figure 4.53 shows the non-corrected fiber tractography. The bottom images 4.54 are the corrected fiber tractographies. The expertise to comment on the anatomical accuracy of these two images is not present in the thesis. The parameters used for the visualizations are: $FA > 0.300$, termination angle=60°, and minimum fiber length= 5mm.

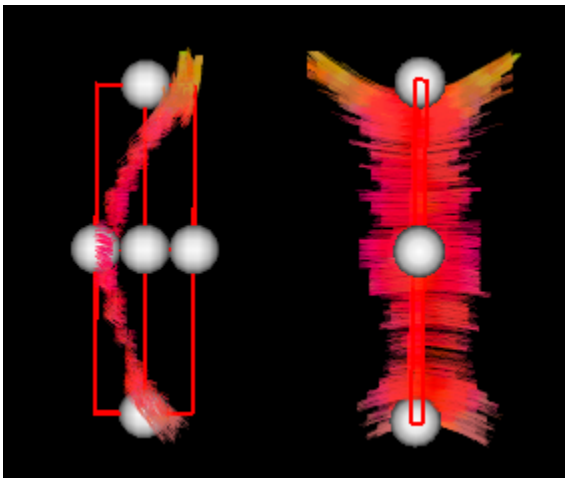

Figure 4.53: The Fiber tractography with ROI shown as the red box for the non-corrected data. The left image is shot sagitally, while the right image is shot axially. The ROI boxes are the same.

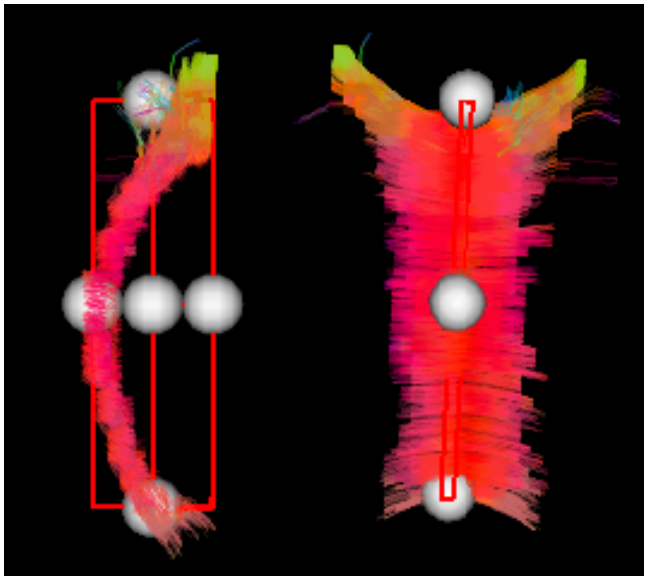

Figure 4.54: The fiber tractography with ROI shown as the red boxes for the corrected data. The left image is shot sagitally, while the right image is shot axially. The ROI boxes are the same, and almost identical to the non-corrected ROI.

4.3 Group Comparison

4.3.1 Eigenvalues

There is a significant difference between the participants with MS and the healthy volunteers in the grey matter λ_3, table 4.27, that is caused by FWE.

Index	Whole Brain	Grey Matter	White Matter	Corpus Callosum
λ_1	$p = 0.61$	$p = 0.89$	$p = 0.64$	$p = 0.39$
$\lambda_1 FW$	$p = 0.09$	$p = 0.90$	$p = 0.43$	$p = 0.52$
λ_2	$p = 0.23$	$p = 0.45$	$p = 0.49$	$p = 0.38$
$\lambda_2 FW$	$p = 0.18$	$p = 0.03$	$p = 0.09$	$p = 0.82$
λ_3	$p = 0.22$	$p = 0.39$	$p = 0.83$	$p = 0.12$
$\lambda_3 FW$	$p = 0.26$	$p < 0.01$	$p = 0.48$	$p = 0.23$

Table 4.27: The p-values of λ_{123} between the participants with MS and healthy volunteers.

4.3.2 Anisotropy Indices

The significant difference in λ_3 in grey matter mean that there are significant differences in some anisotropy indices as well, table 4.28.

Index	Whole Brain	Grey Matter	White Matter	Corpus Callosum
FA	$p = 0.12$	$p < 0.01$	$p = 0.74$	$p = 0.69$
FA FW	$p = 0.13$	$p < 0.01$	$p = 0.72$	$p = 1.00$
MD	$p = 0.30$	$p = 0.54$	$p = 0.61$	$p = 0.25$
MD FW	$p = 0.13$	$p = 0.15$	$p = 0.19$	$p = 0.25$
RA	$p = 0.13$	$p < 0.01$	$p = 0.66$	$p = 0.73$
RA FW	$p = 0.13$	$p < 0.01$	$p = 0.60$	$p = 0.99$
VR	$p = 0.19$	$p < 0.01$	$p = 0.48$	$p = 0.67$
VR FW	$p = 0.15$	$p < 0.01$	$p = 0.46$	$p = 0.98$

Table 4.28: The p-values of the anisotropy indices in the participants with MS and healthy volunteers.

4.3.3 Other Rotationally Invariant Indices

In the invariant indices there are significant differences in the grey matter in the cl and cs indices, table 4.29.

index	Whole Brain	Grey Matter	White Matter	Corpus Callosum
cl	$p = 0.07$	$p < 0.01$	$p = 0.49$	$p = 0.99$
cl FW	$p = 0.07$	$p < 0.01$	$p = 0.44$	$p = 0.74$
cp	$p = 0.34$	$p = 0.02$	$p = 0.54$	$p = 0.38$
cp FW	$p = 0.45$	$p = 0.02$	$p = 0.39$	$p = 0.33$
cs	$p = 0.48$	$p < 0.01$	$p = 0.82$	$p = 0.30$
cs FW	$p = 0.31$	$p < 0.01$	$p = 0.76$	$p = 0.42$

Table 4.29: The p-values of the invariant indices in the participants with MS and healthy volunteers.

Chapter 5

Discussion

5.1 Eigenvalues

5.1.1 Healthy Volunteers

Whole Brain Analysis

In the whole brain analysis, table 4.1, the free water correction yield a modest decrease in the spread of λ_{12}, and a large decrease in the spread of λ_3. It also significantly reduce the value of λ_{123}, by more than 20%, indicating that when analyzing the whole brain as one entity, a significant portion of λ_{123} can be attributed to free water contamination. The absolute value reduction is 1.7, this is the radius of the free water sphere removed. This is the value removed from all indices, and because of $\lambda_1 > \lambda_{23}$, this manifests as a smaller relative change in λ_1 compared to λ_{23}.

Figures 4.6, 4.7, and 4.8 show the effect of FWE. The largest change is found in the areas where there are crossing fibers, FWE removes the free water contamination from these areas, revealing the anisotropy that these fibers cause. The relative change is largest in these areas in λ_3, meaning that the sphericity should be decreased the most in these areas.

Grey Matter

The grey matter has a higher degree of isotropy, $\lambda_1 \sim \lambda_{23}$, table 4.2, than the whole brain analysis. The corrected images have a higher relative difference in λ_{123} than the non-corrected images. After correcting for the free water contamination, grey matter retains its higher degree of isotropy than the rest of the brain. Grey matter has a less organized microstructure than white matter and is measured to be more isotropic than the white matter at the current imaging resolution (3T MRI with mm^3 resolution). It is therefore very difficult to distinguish

each fiber path, thus the isotropy is estimated to be higher. FWE removes a smaller sphere of water from the grey matter, 1.5 compared to the 1.7 for the whole brain analysis. The free water algorithm found less free water contamination in this region than in the whole brain. Because the whole brain includes areas with blood vessels and voxels with a fraction of CSF, this is not surprising.

This discrepancy can be explained by an inherently higher degree of isotropy in the grey matter compared to the average of the whole brain. It could also be a side effect of the lower SNR of the diffusion in grey matter.

White Matter

While λ_1 is smaller in the white matter before correction, table 4.3, the relative difference between λ_1 and λ_{23} is larger than the whole brain analysis or the grey matter. After the correction, the relative difference has increased, the diffusion tensor has a higher degree of linearity. FWE removed a sphere of water with radius 0.7, lower than that of the grey matter (1.5) and the whole brain analysis (1.7). The white matter has the smallest amount of free water contamination in the healthy volunteers compared to grey matter and composite tissue.

λ_1 in the white matter is lower than the grey matter and composite brain before correction, and higher after. White matter has a more clear fiber structure than the grey matter, and is therefore expected to have a higher discrepancy in the indices, $\lambda_1 >> \lambda_{23}$. Due to the already high discrepancy, removing a sphere of water led to a larger difference in the relative value change compared to the grey matter and composite brain.

Corpus Callosum

Corpus callosum has the highest anisotropy of all the regions evaluated, table 4.4. Its fiber structure is clearly defined and there are minimal crossing fibers in the selected region, thus $\lambda_1 >> \lambda_{23}$. Because this area is known to be organized and highly anisotropic, the expectation was that this would be the region with the highest difference both before and after correction ($\lambda_1 >> \lambda 23$). This is the case as this area has the highest λ_1 and lowest λ_{23} compared to white matter, grey matter and composite brain. FWE still removed a small sphere of water, radius 0.6, meaning that in this highly organized fiber structure there is a portion of the diffusion tensor that is attributed to free water contamination. A part of this small sphere could be caused by the ROI touching the ventricles and creating an erroneously high degree of free water contamination.

Summary

The free water correction has a significant impact on λ_{123} in all investigated brain regions. This is the expectation, since the free water correction tries to remove a sphere of isotropic diffusion caused by free water, therefore reducing all three indices approximately equally. It also reduced the spread of all three indices. This reduction in spread in the healthy volunteers can be seen in figures 4.1, 4.2, 4.3, and 4.4, where the peak is sharper in the corrected data.

FWE has the highest impact in areas with either crossing fibers or where the fibers have a chaotic orientation (grey matter). The difference image in figures 4.6, 4.7, and 4.8 support this. There are several bright spots and small areas located in the grey matter, and larger regions of brightness where there are crossing fibers.

5.1.2 Participants with MS

Whole Brain Analysis

The reduction is more than 20% for all three indices in the whole brain analysis, table 4.14. The relative reduction is higher in λ_{23} than in λ_1, the linearity is increased by FWE. The radius removed from the diffusion tensor is 1.8, larger than that of the healthy volunteers.

In figure 4.28 there is a noticeable bump on the high end of the corrected values in λ_{23}. This is not present in the non-corrected values, this could indicate that there are some pockets of higher isotropy, $\lambda_1 \sim \lambda_{23}$, in the participants with MS. This bump is not present in the data from the healthy volunteers, figure 4.1, and could reflect the effect of MS on white matter.

Grey Matter

The bump is not apparent in the grey matter. Grey matter has more similar λ_{123}, table 4.2 than the whole brain. This is caused the same reason as in the healthy volunteers, the grey matter is expected to be more isotropic than the composite brain. The effect of the free water correction is very similar in the grey matter as in the whole brain. The changes were all in the $20 - 30\%$ range, and much like the whole brain analysis, the spread is reduced, figure 4.2. The absolute value change were similar, in the whole brain analysis, λ_{123} were reduced by 1.8, while in the grey matter they were reduced by 1.9. Both of these are higher than their equivalents in the healthy volunteers, FWE found more free water contamination in the participants with MS than in the healthy volunteers. The bump in figure 4.2 is not present in the histograms for the grey matter λ_{23}.

White Matter

White matter has an expected higher difference in λ_{23}, table 4.3, than the grey matter and composite brain. The free water sphere removed from the white matter has a radius of 0.7, smaller than that of the grey matter and composite brain, and identical to the healthy volunteers (0.7). There is the same amount of free water contamination in the participants with MS' white matter matter as the healthy volunteers'.

The histograms, figure 4.30, show a tiny bump on the high end of λ_2, and a small tail on the high end of λ_1. Before the correction, the distribution of λ_2 is visibly Gaussian upon inspection, while λ_1 has a tail. This bump is at a slightly lower value than the one observed in the composite brain, figure 4.28. In the white matter the bump is lower and less prominent than the composite brain. There are some small areas in the white matter of the participants with MS that are more disc-like than expected. λ_3 has the same dsitribution before and after correction.

Corpus Callosum

Corpus callosum has the highest difference in λ_{123}, table 4.17, compared to the grey matter, composite brain and white matter. The reasons for this are suspected to be the same as in section 5.1.1, the homogenous fiber structure and direction of the ROI leading to a high degree of linearity.

The spread is unchanged, as visualized by the the peaks being similar just shifted in figure 4.31. The reduction in value is significant in λ_{123}, and the sphere removed has a radius of 0.5. There is less free water contamination in corpus callosum in the participants with MS, same as the healthy volunteers.

Summary

FWE in the participants with MS revealed a tail on the high end of the Gaussian distribution. This tail is visible in the whole brain analysis, figure 4.28 λ_{23}. In the white matter, figure 4.30, there is a slight bump that lies at a slightly lower value than the one in the composite brain, 5.5 for the white matter and 5.8 for the composite brain. The cause for the bump observed in λ_3 is not visible in the white matter, grey matter or corpus callosum analyses. The source for this is then not discovered, meaning it is probably in an area not covered by either of the white or grey matter masks.

The grey matter λ_3, figure 4.29, and corpus callosum, figure 4.31, show no signs of these effects of FWE. The anomalies in the composite brain λ_{23} and the white matter λ_2 could potentially be caused by the demyelination leading to a loss of directionality.

5.1.3 Group Comparison

Whole Brain Analysis

The data from the participants with MS and the healthy volunteers were almost identical, table 4.14 and table 4.1 respectively. The free water correction has a very slight difference in the amount of change it imposed, the data of the participants with MS has a free water sphere with a radius of 1.8, whereas the one for the healthy volunteers is 1.7. Both data sets also has nearly identical spreads, in the averages of the whole brain analysis, there is not a difference in healthy volunteers and in participants with MS. In the whole brain average there is no significant difference between the healty volunteers and the participants with MS.

The histograms have a visual difference, figure 4.1 for the healthy volunteers and 4.28 for the participants with MS. The healthy volunteers' histograms show Gaussian distributions before and after correction, with less spread after the correction. In the participants with MS there is the aforementioned bump on the high end of λ_{23}. There is a change caused by FWE in some small areas of the participants with MS in the direction of less directionality.

Grey Matter

The grey matter data tells a similar story to the whole brain analysis. The values for the grey matter, table 4.2, started out as having a much lower spread in the participants with MS than in the healthy volunteers, table 4.1, this discrepancy is still present after the free water correction.

The reduction in values suggests that the free water correction removed a slightly larger amount of free water from the participants with MS than the healthy volunteers. From the participants with MS the correction removed 1.7, while in the healthy volunteers it removed 1.5, suggesting that a slightly larger part of λ_{123} in the participants with MS can be ascribed to free water contamination.

White Matter

The effect of FWE on the white matter is very similar in the participants with MS, table 4.16, and the healthy volunteers, table 4.3. The spread in the participants with MS is lower than that of the healthy volunteers before the correction, after the correction this difference is removed for λ_{12}. The amount of free water removed is also identical, FWE removed a sphere of radius 0.7 in both cases.

The slight bump in λ_2 suggests that there are some areas of the white matter in the participants with MS that has more disc-like diffusion than expected based on the healthy volunteers' data. This could be because of demyelination leading to a more disc-like diffusion

tensor in the white matter. The difference in the tail of λ_2 is not large enough to cause a significant difference in the average, table 4.27.

Corpus Callosum

Corpus callosum is similar in both the healthy volunteers, table 4.4, and in the participants with MS, table 4.17, the lack of significance between them supports the claim of no difference, table 4.27. The differences seen in the histograms of the participants with MS, figure 4.31, and healthy volunteers, figure 4.4, can be explained by the ROI being drawn with no experience.

The water sphere removed is also very similar in both cases, 0.5 for the participants with MS, and 0.6 for the healthy volunteers. This difference is too small to draw any conclusions, when combining this with the histograms, it is explained by the inaccuracy of the ROI, rather than any inherent difference between participants with MS and healthy volunteers.

Summary

The averages of λ_{123} are very similar in both the participants with MS and the healthy volunteers. Visually there is a difference in the whole brain analysis, where the participants with MS has visible anomalies on the high end of λ_{23}. The anomaly in λ_3 is not found in the white matter, grey matter or corpus callosum analyses. The λ_2 anomaly is present in the white matter of the participants with MS, albeit at a slightly lower value and not as pronounced. This visual difference is not large enough to cause a significant difference in the averages, table 4.27. The significant difference in grey matter could be caused by either a pathology increasing the isotropy, or the mask size discrepancy, table 3.4. The difference in age of the two groups could also explain some of the discrepancies found, in a study by Prof. O. Pasternak, it was shown that FWE reduces the age-dependency of diffusivity indices. [36]

The relative decreases in λ_{23} were higher than the decrease in λ_1 in both groups, this is similar to the effect observed by Dr. C. Metzler-Baddeley and Prof. O. Pasternak in the whole brain [37], and Dr. R. Berlot [38]. It is difficult to directly compare λ_{23} due to the use of radial diffusivity ($RD = \frac{\lambda_2+\lambda_3}{2}$).

The participants with MS has areas where the diffusion is more spherical after the correction than expected, given the Gaussian nature of the distributions in the healthy volunteers after the correction. Ultimately, the cause of these anomalies in λ_{23} requires further study.

5.2 Anisotropy and Diffusivity

5.2.1 Healthy Volunteers

Whole Brain Analysis

All changes to the anisotropy indices due to FWE in the whole brain analysis were significant, table 4.5. Figure 4.13 show where the correction has the highest impact on FA, it is the same case for RA, figure 4.15, the largest changes are in the same areas as λ_{123}, where there are crossing fibers or in the grey matter. As seen on each side of the ventricles and in corpus callosum, the change is smaller in areas where the fibers are uniform. VR is greatly affected in the same areas, the window level of the difference image in figure 4.16 is set to [0 1], VR in the areas of crossing fibers are therefore increased by almost double that of the other indices. There is not, however, a significant difference between the participants with MS and healthy volunteers for any of the anisotropy indices, table 4.28.

MD, figure 4.14, has the largest reduction where the fibers are crossing, the fiber structure is chaotic, and in the areas close to the blood vessels (outer edges), the last effect is very visible in the before and after images (top). This effect is not visible in the other indices because they measure anisotropy, and the outer edges are areas of high isotropy.

The spread of MD and VR were reduces, this is visible in figure 4.9, the spread of FA and RA remained unaffected by FWE. As seen in figure 4.13 the biggest change is in the areas of crossing fibers. This effect is also demonstrated in figure 4.17, where a threshold has been applied to VR to visualize the effect. The area marked by the red circle has an increase in VR large enough so that the structures are connected.

Grey Matter

Grey matter has a higher degree of isotropy compared to white matter or the whole brain. This is reflected in the lower indices before and after correction, table 4.6. FWE has a large impact on the indices, and it can be seen in figures 4.13, 4.14, 4.15, and 4.16. It is uncertain whether or not FWE has a significant impact on the anisotropy indices, table 4.28, due to the significant difference both before and after correction. In all the difference images the grey matter has a higher average intensity than the white matter. The spread in grey matter is only affected for MD, it is unchanged for FA, RA, and VR. This is seen in figure 4.10 where it is clearly visible that MD is the most affected index,while the other indices are mostly the same shape and just shifted in the direction of higher anisotropy.

While λ_{123} in grey matter, table 4.2, has a lower relative decrease than the whole brain, table 4.1. The anisotropy indices in the grey matter has a slightly larger relative increase

compared to the whole brain, 4.5. The difference between participants with MS and healthy volunteers, is significant before and after correction, table 4.28, This is due to the inherently higher degree of isotropy leading to lower anisotropy indices, a small change in the value of these indices are relatively large. All changes in the grey matter were significant in the direction of higher anisotropy.

White Matter

The inherently high anisotropy of white matter mean the relative changes are small, table 4.7. The crossing fibers effect observed in the difference images are located within the white matter. Due to these areas being affected by FWE to a higher degree than the rest of the brain, the increase in the anisotropy indices for the white matter could be driven by the increasing anisotropy of these areas that were possibly erroneously observed as having a higher degree of isotropy before the correction.

The spread remains the same for all indices except MD, where the spread saw a dramatic decrease (0.2-¿0.06), this is very visible in figure 4.11. FWE shifted the indices towards higher anisotropy, and in the case of MD, drastically lower spread as well.

Corpus Callosum

Corpus callosum is the area with the highest anisotropy, table 4.8. This is the area that is least affected by FWE in the λ_{123} analysis. It is therefore not surprising that it has the least relative change in all four indices. The absolute value change however is greater in corpus callosum than in the white matter, grey matter and composite brain. This is visible in figure 4.12 where the shift is clear, the spread has remained the same, the histograms have the same shape before and after the correction.

Summary

FWE has a significant effect on all anisotropy indices in the healthy volunteers in all areas evaluated. Figures 4.13, 4.14, 4.15, 4.16, and 4.17 all show that FWE has a large effect on areas of crossing fibers. Crossing fibers are a known problem for conventional DTI as it can not distinguish the fibers and reports those areas as having a high degree of isotropy. FWE seemingly then fixes part of this problem, leading to a higher anisotropy where there should be higher anisotropy.

This effect is not visible in figures 4.9, 4.10, 4.11, and 4.12, as the histograms contain no spatial information. The localized effect of correcting crossing fibers is only visible when the anisotropy indices is put together with where this anisotropy lies.

5.2.2 Participants with MS

Whole Brain Analysis

In the whole brain histogram of the participants with MS there is a visible anomaly in MD, 4.36. Where the expectation is a Gaussian distribution there is a small bump after correction. This fits with the observations made in λ_{123}, figure 4.28.

The averages of the anisotropy indices, table 4.18, are affected by FWE in the same way as the indices for the healthy volunteers, table 4.9. There is a shift towards higher anisotropy with the same spreads, except in MD, where the spread is reduced by a factor of three.

Grey Matter

The anomaly observed in MD in the whole brain analysis, figure 4.36, is not present in the grey matter, figure 4.37. Grey matter follow the same pattern in the participants with MS, table 4.19, as in the healthy volunteers, table 4.6.

Grey matter has a high level of isotropy, this is confirmed by the anisotropy indices being lower than in the composite brain and the white matter. All the distributions in the grey matter of the participants with MS keep their Gaussian shapes after the correction. FWE has shifted the values significantly towards a generally higher anisotropy. The spread is unchanged for all indices, except for MD where it has decreased.

White Matter

The shift caused by FWE in white matter is visible in figure 4.38, this is due to histograms showing a absolute value change more readily than a relative change. The relative (%) change of the anisotropy indices in white matter, table 4.20, is lower than the grey matter and composite brain.

The bump observed in figure 4.36 is not visible in the white matter indices, figure 4.38. This could be cause by the segmentation not recognizing white matter tissue with a pathology as white matter.

Corpus Callosum

Corpus callosum, table 4.21, has a significant small increase in anisotropy due to FWE. The ROI used for the corpus callosum analysis lies within an area that has little visual change in the difference images. This is due to the highly organized structure of the fiber tracts within that ROI.

The correction has no noticeable impact on the spread of the values, and due to the small number of voxels covered, the histograms, 4.39, contain little useful information. The data seems to follow the overall pattern of a Gaussian distribution that is shifted towards higher anisotropy by FWE.

Summary

There is a noticeable bump in MD when the whole brain is analyzed, figure 4.36, this bump is on the high end of the curve, the same place a bump is observed in the eigenvalue analysis of the same region, figure 4.28. The reason for this bump could be localized areas of higher isotropy caused by the MS disease. It does not show up in the white or grey matter segmentations, this could be due to the way the masks are calculated. Due to atrophy, the segmentation might mistakenly give the atrophied area a lower probability of being either white or grey matter. The smaller size of the grey matter mask in the participants with MS, table 3.4, could indicate that the source of the bump could lie in an area not assigned to grey matter by mistake.

5.2.3 Group Comparison

Whole Brain Analysis

There is a tendency towards lower estimated anisotropy in the participants with MS, table 4.18, than the healthy volunteers, table 4.5, but the difference is not significant, table 4.28. MD is identical in both cases, but as mentioned, there is a bump in the participants with MS, figure 4.36, that is not present in the healthy volunteers, figure 4.9.

Grey Matter

The grey matter in the participants with MS, table 4.19 is also slightly more isotropic than the grey matter in the healthy volunteers, table 4.6, this difference is significant for FA, RA and VR, table 4.28.

The spread is lower for all indices in the grey matter in the participants with MS compared to the healthy volunteers, this could be due to the oddity in the grey matter mask mentioned in section 5.2.2. The segmentation could have selected an area of more uniform diffusion in the participants with MS.

White Matter

The white matter is identical in the participants with MS, table 4.20, and the healthy volunteers, 4.7. The spread in the participants with MS is lower before and after correction, but FWE did reduce this difference in MD between the participants with MS and healthy volunteers. There is however, no significant difference before or after the correction, table 4.28.

Visually there is a very slight difference on the low end of the curve for VR in the participants with MS, figure 4.11. There are more voxels in the participants with MS in the $0 - 0.05$ range than the healthy volunteers, fig 4.9. There is also a visible dfference in RA, although this could be due to noise, as it is not present in FA, a more noise resistant index. These small pockets of higher isotropy can also be observed in the tail of MD, there is a longer tail on the MD of the participants with MS than in the healthy volunteers.

Corpus Callosum

Corpus callosum has the most similar spread when comparing the participants with MS, table 4.8, and the healthy volunteers, table 4.21, this is supported by the p-values, table 4.28. Visually there is also little difference, the participants with MS, figure 4.39, has slightly more noise than the healthy volunteers, 4.12. This difference however, is most likely due to the placing of the ROI, which is done without any formal training or experience.

Summary

The bump that is discovered in the participants with MS in section 5.1 is present in MD, and to a very small degree in the white matter VR, where it shows as localized areas of less anisotropy. This bump in MD is not explained by the grey matter, white matter or corpus callosum. The source of this discrepancy might lie in the grey matter, the grey matter mask is smaller in the participants with MS than in the healthy volunteers, table 3.4. The localized areas of more isotropy could be due to the lesions caused by MS, and they could be outside what the segmentation determined to be either grey or white matter. This localized isotropy in the participants with MS is not large enough to create a significant difference, table 4.28.

The behavior of FA and MD under FWE is similar to what was observed in a study conducted by Dr. C. Metzler-Baddeley and Prof. O. Pasternak et al [37], where MD decreased and FA increased, the same behavior was observed by Dr. R. Berlot. [38]

5.3 Other Rotationally Invariant Indices

5.3.1 Healthy Volunteers

Whole Brain Analysis

FWE has a significant effect on cl, cp, and cs, table 4.9. There is an increase in the linearity, cl, and in planarity, cp, as a result of the decrease in sphericity. Cl and cp have the same relative change (19.5%), the absolute value changed more in cp (1.7 vs 1.3 for cl), the diffusion tensor has gained more planarity than linearity. All the changes are significant, and the spread is unchanged.

On the high end of cs, figure 4.18, from $8.5 - 9.5$ the distribution has a different shape after the correction. It has gone from having a plateau to a linear decrease. Both of these mirror the elongated tail observed in λ_3, figure 4.1. While FWE increases the linearity and planarity of the diffusion tensor, the ellipsoid constructed from λ_{123} is still dominated by the spherical part.

Figures 4.22, 4.23, and 4.24 show that, similarly to λ_{123} and the anisotropy indices, the largest change is in the areas of crossing fibers. This effect in cs, figure 4.25, is not as pronounced, contrary to cl and cp, FWE has a large effect on cs within corpus callosum

Grey Matter

In the grey matter, table 4.10, there a higher degree of spherical anisotropy, than in the composite brain, table 4.9. The diffusion tensor in the grey matter is more isotropic than the whole brain, this is supported by the smaller cl and cp.

There is also a higher degree of planarity in the grey matter compared to the composite brain, the difference between cp and cl is greater. The difference between these two indices is the same before and after the correction, same as with the whole brain analysis. The relative increase in linearity and planarity is greater in grey matter than in the composite brain, figure 4.22 and 4.24, this due to the high degree of isotropy in grey matter.

FWE did not change the distribution of cl, cp, and cs, figure 4.19. The distributions are Gaussian before and after, and the plateau $->$ linear decrease seen in the composite brain is not observed.

White Matter

The change in cp is not significant. White matter has a larger degree of linearity than planarity, table 4.11, compared to the grey matter, table 4.10, and the composite brain, table 4.9. Due to the more organized nature of its fiber structure, this is as expected. FWE

has shifted the values towards a higher degree of linearity and planarity, but has not changed the shape of the distribution, figure 4.20, or the spread. All changes in white matter are significant.

Corpus Callosum

Corpus callosum has a very organized fiber structure, thus it also has a high degree of linearity, table 4.12. The planarity of corpus callosum is the same as the composite brain average, table 4.9, but the change in cp is not significant in corpus callosum. This is clear in the ellipsoid created by λ_{123}, figure 4.5.

FWE has a larger relative effect on cs in corpus callosum than in white matter, grey matter, and the composite brain. In figure 4.25 this is shown graphically, as corpus callosum is brighter than the surrounding areas. The change in cp is not significant.

Summary

In all areas cl, cp, and cs followed the same pattern, the relative increase in cl and cp within one area is the same ($\pm 1\%$). The small change in the distribution of the high end of cs in the composite brain, figure 4.18, is not observed in any of the other areas of interest. FWE has the largest effect in the same regions for cl and cp as it did for the anisotropy indices in section 5.2 and λ_{123} in section 5.1. Cs is affected the most in the ROI in corpus callosum, this is expected as FWE removes a sphere of water and cs is the measure of the sphere of water in relation to the ellipsoid created by λ_{123}.

5.3.2 Participants with MS

Whole Brain Analysis

The invariant indices for the whole brain analysis in the participants with MS changed significantly, table 4.22. The averages show an increasing degree of linearity and planarity, and a reduction in sphericity. This is as expected.

FWE has an effect on the distributions of cl and cs, figure 4.45. Cl has a bump that is smoothed out by the correction, there are certain regions where the non-corrected data has lower degree of linearity than it should, this anomaly is then reduced by FWE. Cs has a very visible bump on the high end of the curve, FWE has a similar smoothing effect, but it is still present after the correction.

Combining both of these findings means that there are areas of higher than expected sphericity and lower than expected linearity. This could be indicative of lesions in these

areas, they are expected to decrease linearity and increase sphericity due to a higher degree of isotropy.

Grey Matter

The grey matter, table 4.23, has a generally more spherical diffusion tensor. Evidenced by the high estimated sphericity, low linearity and low planarity. While the relative change is high in cl and cp, the reduction in cs is low, both in absolute and relative terms.

The distributions are unaffected by FWE, figure 4.46, the spread remains the same after correction. There is a slight shift toward higher linearity and planarity. Before and after correction, grey matter remains the region with the highest degree of sphericity, this is as expected due to the chaotic fiber structure and fits the observations in sections 5.2 and 5.1.

White Matter

The white matter behaved as expected of a region with a more organized fiber structure, table 4.24. Cl and cp is increased by almost the same relative amount, caused by the decrease in cs. There is no noticeable change in the distributions of cl, cp, and cs, figure 4.20, the spread is unchanged. The indices have been shifted, but due to maintaining the same shape before and after correction there is not any anomaly uncovered by FWE.

Corpus Callosum

Corpus callosum, table 4.25, as expected, is more linear than white matter, grey matter and the composite brain. FWE increased cl and cp by the same degree, the change in cp is however, not significant. The distributions are unchanged by FWE, figure 4.48, there are fewer data points than in the grey matter, white matter and composite brain. This could explain why the change in cp is not significant, another explanation is that it is not affected by FWE in corpus callosum, but this is deemed unlikely as cp is affected similarly to cl in all other areas.

Summary

There is an unexplained bump found in cl and cs in the whole brain analysis, figure 4.45, that is not present in any of the other analyses. This remains after correction, meaning that it is not caused by free water contamination, this could point to some pathology increasing the isotropy in some small areas of the brain.

The overall effect of FWE is the same in grey matter, white matter, corpus callosum and the composite brain. The reduction in cs causes an increase in cl and cp, this is expected, as

FWE removes a sphere of water, and cs is the portion of the ellipsoid generated by λ_{123} that is attributable to the sphere generated by λ_3.

5.3.3 Group Comparison

Whole Brain Analysis

Comparing the values found for the healthy volunteers, table 4.9, and the participants with MS, table 4.22 for the whole brain show that they have the same amount of sphericity. It is then possible to conclude that when taking the whole brain average, there is no difference between the healthy volunteers and participants with MS.

Both the healthy volunteers, figure 4.18, and participants with MS, figure 4.45, show indications of a small bump on the low end of the curve of cl. This bump is completely smoothed out by FWE in the healthy volunteers, but it maintains some of its shape in the participants with MS. There is a similar effect on the high end of the curve of cs. In the healthy volunteers, the bump has disappeared as an effect of FWE, but in the participants with MS this is still present, it is not large enough to cause a significant difference however, table 4.29.

The bump in healthy volunteers then seem to be created by free water contamination that is expectedly removed by FWE. In the participants with MS they are still present, suggesting that something other than free water contamination might be causing localized areas of higher than expected isotropy.

Grey Matter

In the grey matter, the healthy volunteers, table 4.10, and the participants with MS, table 4.23 follow the same trend. The spread is larger in the healthy volunteers for all three indices, in the case of cs by an order of magnitude. The diffusion tensor for the participants with MS seem to be have a higher cs than the healthy ones, after correction.

There is not any visual difference between the healthy volunteers, figure 4.19, and the participants with MS, figure 4.46. There is a significant difference before and after correction, table 4.29, thus it is unclear in what way FWE has impacted the difference.

The size difference in the grey matter masks, table 3.4, could explain why the spread is so much lower in the participants with MS. The segmentation might have removed the areas that would have resulted in a higher spread.

White Matter

The indices in the healthy volunteers, table 4.11, are similar to those of the participants with MS, table 4.24. FWE has an identical effect on both groups, the distributions are shifted towards higher linearity and planarity, and lower sphericity. Figure 4.47 for the participants with MS and figure 4.20 for the healthy volunteers show little to no visual difference, this is supported by the lack of significance before and after correction, table 4.29.

Corpus Callosum

In corpus callosum all the indices are almost the same for both the participants with MS, table 4.25 and the healthy volunteers, table 4.21, both before and after the free water correction. For both the participants with MS and the healthy volunteers, the change in cp is not significant. The distributions are also very similar, there are no discernible or significant difference, table 4.29, between the healthy volunteers, figure 4.48, and the participants with MS, figure 4.48.

Summary

The invariant indices cl, cp, and cs are very similar when comparing the participants with MS (tables 4.22, 4.23, 4.24, and 4.25), with the healthy volunteers (tables 4.9, 4.10, 4.11, and 4.12), the only significant differences were found in the grey matter, table 4.29. The spread is generally lower in the participants with MS, than in the healthy volunteers.

Visually there is a difference in the whole brain analysis. In the healthy volunteers, figure 4.18, there is a bump on the low end of cl and a bump on the high end of cs, these are removed by FWE. In the participants with MS, figure 4.18, these same bumps appear in the uncorrected data, but are not removed by FWE. This suggests that in the participants with MS, there is something besides free water contamination that are causing these anomalies. These anomalies do not appear in the grey matter, white matter or corpus callosum of either group.

The cause of these anomalies, together with the ones observed in section 5.2 and section 5.1, lie somewhere not covered by either the white or grey matter masks. This thesis does not go further in the search for the source of these anomalies.

5.4 Fiber Tractography

5.4.1 Healthy Volunteers

The fiber tractography, table 4.13 find more fibers in the free water corrected data. The difference get smaller as the FA threshold is reduced, the free water correction lead to a higher average FA, in addition to finding more fibers that might have been obscured by free water contamination. A cautionary note, there might also be some fibers that are false-positives in the free water corrected data, as is mentioned in section 2.2.2. For all cutoff angles, the trend is the same, a large difference in fibers found when the FA threshold is $FA > 0.300$, that gradually decreases as the threshold decreases. The smaller impact of the cutoff angle compared to the FA threshold, is because the fibers in this region are mainly straight or with very low angles.

The free water correction led to a more distinct cingulum, figure 4.27, the cingulum on the left side is much longer than that of figure 4.26. This suggests that in the non-corrected data, this structure was obscured by something, or that it fell below the FA threshold used in creating the visualizations.

5.4.2 Participants with MS

The fiber tractography algorithm in NordicIce (Nordic NeuroLabs inc, Bergen, Norway) is greatly affected by the free water correction in the participants with MS, table 4.26. There are more fibers found in the free water corrected data, this difference decreased as the FA threshold went down. There is also a generally higher degree of anisotropy observed, but due to the large spread, this does not necessarily mean anything. Naturally, as the threshold values go down, both the amount of fibers and the spread in FA are increased.

The images, figures 4.53 and 4.54 show the non-corrected and corrected fiber tracts respectively. From these visualizations it is easy to see that the free water correction has a lot more fibers. With the parameters used in the visualizations (FA$>$ 0.300, cutoff angle = 60°, minimum length = 5mm) there are 2663 fibers found in the non-corrected and 4984 in the corrected fiber tractography.

5.4.3 Group Comparison

Comparing the participant with MS, table 4.26, and the healthy volunteer, table 4.13, there were more fibers found in the participant with MS for all parameters. Although this could be these two specific brains, since the fiber tractography is only done on one healthy volunteer and one participants with MS. For the same reason, there are not any conclusions that can

be drawn from the FA values, there is only one data point for each case. The difference could also be due the ROI, since it had to be redrawn visually for the participant with MS to match the healthy volunteer.

A visual comparison of the healthy fiber tractography, 4.26 and 4.27, with that of the participant with MS, 4.53 and 4.54, show some difference as well. The most visual difference is the cingulum (green), it is much more visible in the healthy fiber tractography, especially for the free water correction, there is some indication of this effect in the participant with MS. The right side remains very similar. The participant with MS seem to have many more fibers across (red) than the healthy volunteer, and they are more densely packed. There are also some "stray fibers" that can be observed in the post-correction participant with MS fiber tractography at the top. None of these findings are significant however, due to only comparing one healthy volunteer to one participant with MS.

5.5 Limitations and Outlook

Participant Selection

In this thesis, 20 healthy volunteers and 20 participants with recently diagnosed MS were selected. The participants were selected randomly from ongoing data sampling studies, thus removing any kind of selection bias, that means that there is a fairly large spread in age. This might have affected the resulting means and standard deviations. The large spread in age and difference between the groups, table 3.3, might affect the difference between the two groups.

This thesis did not set out to directly analyze the difference between the two groups, but rather investigate the effect of FWE on the groups. The findings reflect this, as FWE affected both groups in the same way, influencing the indices towards higher anisotropy. In future analyses, in order to perform a direct comparative study, the participants should be age-controlled.

Grey and White Matter Segmentation

Issues when using automatic segmentation of grey and white matter in a brain with a known pathology arose. The grey matter masks for the participants with MS were smaller on average than those of the healthy volunteers, table 3.4. The segmentation program could have altered the results by not properly segmenting out the grey matter in the participants with MS, this could be due to atrophy, giving the tissue attributes that the segmentation program did not recognize as grey matter.

Erroneous masks caused by either movement or artifacts could explain the significantly smaller masks in two of the healthy volunteers. To investigate the effect of this problem, the two participants with grey matter masks one order of magnitude smaller than the mean were selected out. These participants belong to the healthy volunteers group, it is therefore unlikely that the reduced grey matter masks are the result of severe atrophy caused by a pathology.

The segmentation of the whole brain, could also explain the similarity between the two groups. MS affects white matter to a high degree, therefore, a difference is expected to be found inside the white matter. In this thesis there was no difference found besides some signal deviation ("bumps"), meaning that the masks might be too coarse to find any effect of MS at this early stage. In future analyses, this coarse whole brain white matter approach could be replaced by more refined techniques that incorporate spatial information could be used. This would have to be done with more expertise than this thesis due to issues that might arise due to the known pathology.

Some of the difference in grey matter mask sizes can be ascribed to age, as the grey matter volume has a negative correlation with age. The white matter is the same size in both groups, likely because the white matter volume of the whole brain has a very modest increase until about 40 years, and it is too early to see the effect of MS on the macroscopic level in white matter. [39]

The analysis was then redone with the 18 remaining healthy volunteers to determine the impact of the erroneous grey matter masks. The size of the grey matter masks are significant ($p < 0.01$) after the removal of the two participants from the data set. Additionally there is a significance in λ_{23} before correction that disappears after correction. There is no change in the significance in the whole brain analysis, white matter analysis, or corpus callosum ROI-analysis.

Slice Alignment

Due to the issues forcing the analysis to be performed on 17 slices in the middle of the brain, the issue of slice alignment could have an effect. This was also done in order to reduce the effect of susceptibility effects close to the sinuses. This could also affect the results by each participant having slightly different start and end points. Averaging all measurements across the 20 participants in each group should eliminate the error that might occur when doing a slice-to-slice comparison.

This also makes it difficult to directly compare masks and f-maps. Due to the non-alignment of the slices, the data does not overlap. In order to achieve a direct spatial comparison, the data could be registered to a standard template prior to doing the analysis.

This is not done because the registration might be affected by the presence of a pathology, thus raising new methodological issues. Additionally the histogram approach used for this analysis removes the need for spatial localization, otherwise needed for the spatial approach. It is unlikely that the main findings would be different, had the spatial approach been selected.

Free Water Elimination

FWE has been shown significantly influence the estimation of anisotropy indices. It is especially effective in regions of crossing fiber bundles and may serve to reduce some of the ambiguity in these regions. FWE is still in development, and has so far only been developed as a single-shell (one b-value) model. The diffusion data used in this thesis was gathered using a more advanced imaging scheme, several b-value, table 3.2, than what the model was designed for. Future analyses might be able to use a multi-shell FWE model that could be more sensitive to disease processes, this will be possible through the ongoing collaboration with the milieu that first proposed the technique (Pasternak et al).

This testifies to the novelty of the current analysis, it is performed on what is currently available with regards to data and technology. It is also the first time FWE is used on MS patients, previously FWE has been used on patients with Parkinson's disease [31], Alzheimer's disease [32], schizophrenia [33], and the effect of concussion on a small group [34]. It is therefore of great interest to use this technique in longitudinal follow-up examinations, combining the results of these future analyses with clinical information (cognitive performance, clinical disease progression).

5.6 Conclusion

The results of this thesis show that FWE will increase the measured anisotropy in the brain by removing a sphere of water. This supports the hypothesis that by removing a spherical portion of the ellipsoid constructed by λ_{123}, the remaining free water corrected ellipsoid is more anisotropic. It is further shown that FWE is not uniform, the correction is higher in areas of crossing fibers or chaotic fiber orientation, this should allow for better separation of fibers. The difference in diffusion indices between the two groups were not significantly different, except for the anisotropy indices in grey matter.

By utilizing FWE it is possible to evaluate voxels consisting of more than one fiber path by differentiating fiber paths and calculate correct indices that conventional DTI will evaluate as more isotropic than they are. The various effects caused by different artifacts, aging, and a possible pathology, means that, based on the preliminary analysis in this study, this thesis can not conclude that any differences were induced by MS. It will however, be very interesting

to use this same method in the follow-up on the participants with MS to see when the indices diverge from the healthy volunteers, and how they change within the same patient group.

Bibliography

[1] O'Donnell LJ, Westin C-F. *An introduction to diffusion tensor image analysis.* Neurosurgery clinics of North America. 2011;22(2):185-viii. doi:10.1016/j.nec.2010.12.004.

[2] Pasternak, O. , Sochen, N. , Gur, Y. , Intrator, N. and Assaf, Y. , *Free water elimination and mapping from diffusion MRI.* Magn. Reson. Med., 62: 717-730. doi:10.1002/mrm.22055

[3] Ernest M. Henley and Alejandro Garcia. *Subatomic physics.* World Scientific Pub- lishing, 5 Toh Tuck Link, Singapore 596224, third edition, 2007.

[4] F. Schwabl, *The Zeeman Effect and the Stark Effect. In: Quantum Mechanics. 4th ed.* Springer, Berlin, Heidelberg (2007)

[5] Roméo Françoise, and Hoult D. I. *"Magnet Field Profiling: Analysis and Correcting Coil Design."* Magnetic Resonance in Medicine 1, no. 1 (March 1984): 44–65. https://doi.org/10.1002/mrm.1910010107.

[6] Jezzard, Peter. *"Shim Coil Design, Limitations and Implications,"* n.d., 6.

[7] Ray H. Hashemi ,William G. Bradley , Christopher J. Lisanti *"MRI The Basics"*, 3rd ed, (2010);

[8] de Graaf, R. A., Brown, P. B., McIntyre, S. , Nixon, T. W., Behar, K. L. and Rothman, D. L., *High magnetic field water and metabolite proton T1 and T2 relaxation in rat brain in vivo.* Magn. Reson. Med. (2006), 56: 386-394. doi:10.1002/mrm.20946

[9] Bjørnerud, Atle. *"The Physics of Magnetic Resonance Imaging,"* Department of Physics, University of Oslo, March 2008.

[10] Dr Graham Lloyd-Jones. $MRI Interpretation - T1vT2images$ `https://www.radiologymasterclass.co.uk/tutorials/mri/t1_and_t2_images` (Accessed: 2018-04-05)

[11] Renate Grüner. *"Compendium PHYS212 Medical Physics and Technology."* Department of Physics and Technology, University of Bergen, 2012.

[12] Allen Elster *Gradientcoils − QuestionsandAnswersinMRI* `http://mriquestions.com/gradient-coils.html` (Accessed: 2018-04-05)

[13] Lothar R. Schad. *Problems in texture analysis with magnetic resonance imaging.* Dialogues in Clinical Neuroscience, 6:235–242, 2004.

[14] Dr. Brian Gilcrease-Garcia, Dr. Ushman Bashir et al. *Gibbs and truncation artifacts— Radiology Reference Article — Radiopaedia.org*, `http://radiopaedia.org/articles/gibbs-and-truncation-artifacts`. (Accessed: 2018-08-20).

[15] Allen Elster *Gibbs artifact? - Questions and Answers in MRI* `http://mriquestions.com/gibbs-artifact.html` (Accessed: 2018-08-20).

[16] Gary P. Zientara, Ph.D. *"Fast Imaging Techniques for Interventional MRI".* `https://www.spl.harvard.edu/archive/spl-pre2007/pages/papers/zientara/fast/fastimaging.html` (Accessed 2018-08-01)

[17] Mark Hammer, *MRI Physics: MRI Pulse Sequences.* `http://xrayphysics.com/sequences.html` (accessed 2018-10-01)

[18] A. Prof Frank Gaillard, *MRI Physics Diagrams*, `https://radiopaedia.org/cases/mri-physics-diagrams`.

[19] Jeffrey J. Neil. *Measurement of water motion (apparent diffusion) in biological systems.* Concepts in Magn. Reson., 9:385–401, 1997.

[20] Le Bihan, D. , Poupon, C. , Amadon, A. and Lethimonnier, F. (2006), *Artifacts and pitfalls in diffusion MRI.* J. Magn. Reson. Imaging, 24: 478-488. doi:10.1002/jmri.20683

[21] Luo, Zhanpeng, Li Litao, Suxi Gu, Xiaobo Luo, Dawei Li, Long Yu, and Yuanzheng Ma. *"Standard-b-Value vs Low-b-Value DWI for Differentiation of Benign and Malignant Vertebral Fractures: A Meta-Analysis."* The British Journal of Radiology 89, no. 1058 (February 2016). https://doi.org/10.1259/bjr.20150384.

[22] Bihan, Denis Le, Jean-François Mangin, Cyril Poupon, Chris A. Clark, Sabina Pappata, Nicolas Molko, and Hughes Chabriat. *"Diffusion Tensor Imaging: Concepts and Applications."* Journal of Magnetic Resonance Imaging 13, no. 4 (April 1, 2001): 534–46. https://doi.org/10.1002/jmri.1076.

[23] Pierpaoli, C. and Basser, P. J. (1996), *Toward a quantitative assessment of diffusion anisotropy.* Magn. Reson. Med., 36: 893-906. doi:10.1002/mrm.1910360612

[24] Peter J. Basser, Carlo Pierpaoli, *Microstructural and Physiological Features of Tissues Elucidated by Quantitative-Diffusion-Tensor MRI*, Journal of Magnetic Resonance, Series B, Volume 111, Issue 3,1996,Pages 209-219, ISSN 1064-1866, https://doi.org/10.1006/jmrb.1996.0086.

[25] Hasan, K. M., Alexander, A. L. and Narayana, P. A. (2004), *Does fractional anisotropy have better noise immunity characteristics than relative anisotropy in diffusion tensor MRI? An analytical approach.* Magn. Reson. Med., 51: 413-417. doi:10.1002/mrm.10682

[26] C.F. Westin, S. Peled, H. Gubjartsson, R. Kikinis, and F.A. Jolesz. *Geometrical diffusion measures for MRI from tensor basis analysis.* In ISMRM, Conf. Proc., page 1742, April 1997.

[27] Basser, Peter J., Sinisa Pajevic, Carlo Pierpaoli, Jeffrey Duda, and Akram Aldroubi. *"In Vivo Fiber Tractography Using DT-MRI Data."* Magnetic Resonance in Medicine 44, no. 4 (October 1, 2000): 625–32. https://doi.org/10.1002/1522-2594(200010)44:4¡625::AID-MRM17¿3.0.CO;2-O.

[28] Mori, Susumu, and Peter C. M. van Zijl. *"Fiber Tracking:Principles and Strategies - a Technical Review."* NMR in Biomedicine 15, no. 7-8 (November 1, 2002): 468-80. https://doi.org/10.1002/nbm.781.

[29] P. Mukherjee, S.W. CChung, J.I. Berman, C.P. Hess and R.G. Henry. *Diffusion Tensor MR Imaging and Fiber Tractography: Technical Considerations*, American Journal of Neuroradiology May 2008 , 29 (5) 843-852; DOI: https://doi.org/10.3174/ajnr.A1052.

[30] Pierpaoli C, Jones DK. *Removing CSF contamination in brain DT-MRIs by using a two-compartment tensor model.* InProc. International Society for Magnetic Resonance in Medicine 12th Scientific meeting ISMRM04 2004 (p. 1215).

[31] Planetta PJ, Ofori E, Pasternak O, et al. *Free-water imaging in Parkinson's disease and atypical parkinsonism.* Brain. 2016;139(2):495-508. doi:10.1093/brain/awv361.

[32] Ji F, Pasternak O, Liu S, et al. *Distinct white matter microstructural abnormalities and extracellular water increases relate to cognitive impairment in Alzheimer's disease with and without cerebrovascular disease. Alzheimer's Research & Therapy.* 2017;9:63. doi:10.1186/s13195-017-0292-4.3

[33] Lena K.L. Oestreich, Amanda E. Lyall, Ofer Pasternak, Zora Kikinis, Dominick T. Newell, Peter Savadjiev, Sylvain Bouix, Martha E. Shenton, Marek Kubicki, Thomas J. Whitford, Simon McCarthy-Jones, *Characterizing white matter changes in chronic schizophrenia: A free-water imaging multi-site study.* Schizophrenia Research, Volume 189, 2017, Pages 153-161, ISSN 0920-9964, https://doi.org/10.1016/j.schres.2017.02.006.

[34] Pasternak O, Koerte IK, Bouix S, et al. *Hockey Concussion Education Project, Part 2. Microstructural white matter alterations in acutely concussed ice hockey players: a longitudinal free-water MRI study. Journal of neurosurgery.* 2014;120(4):873-881. doi:10.3171/2013.12.JNS132090.

[35] Kjell-Morten Myhr, Øivind Grytten Torkildsen, and Lars Bø. *Multippel sklerose*, 2011.

[36] Jordan A. Chad, Ofer Pasternak, David H. Salat, J. Jean Chen, *Re-examining age-related differences in white matter microstructure with free-water corrected diffusion tensor imaging.*Neurobiology of Aging, Volume 71, 2018, Pages 161-170, ISSN 0197-4580, https://doi.org/10.1016/j.neurobiolaging.2018.07.018.

[37] Claudia Metzler-Baddeley, Michael J. O'Sullivan, Sonya Bells, Ofer Pasternak, Derek K. Jones, *How and how not to correct for CSF-contamination in diffusion MRI.* NeuroImage, Volume 59, Issue 2, 2012, Pages 1394-1403, ISSN 1053-8119, https://doi.org/10.1016/j.neuroimage.2011.08.043.

[38] Berlot R, Metzler-Baddeley C, Jones DK, O'Sullivan MJ. *CSF contamination contributes to apparent microstructural alterations in mild cognitive impairment.* Neuroimage. 2014;92(100):27-35. doi:10.1016/j.neuroimage.2014.01.031.

[39] Giorgio A, Santelli L, Tomassini V, et al. *Age-related changes in grey and white matter structure throughout adulthood.* Neuroimage. 2010;51(3-2):943-951. doi:10.1016/j.neuroimage.2010.03.004.

Appendix A

All the relevant MatLab scripts.